SUBGRID MODELS FOR LARGE EDDY SIMULATION: SCALAR FLUX, SCALAR DISSIPATION AND ENERGY DISSIPATION

By

Sergei G. Chumakov

A dissertation submitted in partial fulfillment of the

requirements for the degree of

Doctor of Philosophy

(Mechanical Engineering)

at the

UNIVERSITY OF WISCONSIN – MADISON

2005

Abstract

Subgrid Models for Large-Eddy Simulation:

Scalar Flux, Scalar Dissipation and Energy Dissipation

Sergei Chumakov

Under supervision of Professor Christopher J. Rutland

at the University of Wisconsin-Madison

This project can be regarded as a continuation of the research done at the Engine Research Center in the fields of Large Eddy Simulation (LES) and Direct Numerical Simulation model development, evaluation and implementation.

New LES models were proposed for

- subgrid-scale scalar transport
- subgrid-scale dissipation of a scalar
- subgrid-scale energy dissipation.

The new models belong to the class of Dynamic Structure (DS) models. The DS models rely on the Leonard-type term to provide the structure of the modeled quantity, and then a particular scaling factor is used. The models were evaluated *a priori* using DNS databases created at the Engine Research Center for channel flow, Couette flow, non-reacting mixing layer and decaying isotropic turbulence with passive scalar.

A DNS code that was used for creating the DNS databases was modified in order to support Large Eddy Simulation techniques for the purpose of *a posteriori* evaluation of

the most successful among the models proposed. The results from LES and DNS runs were compared for the non-reacting spatially developing shear layer and decaying isotropic turbulence. A good agreement between LES and DNS was observed.

Overall, the new models have been found to perform adequately. In *a priori* tests the DS models perform as good as the popular models from the literature or better. The thorough *a posteriori* evaluation of the full suit of models is not yet complete but the available results already indicate a good potential.

Acknowledgements

First and foremost, I would like to express my gratitude to Professor Christopher J. Rutland for accepting me into the PhD program at the Mechanical Engineering Department and being a very patient advisor.

I also would like to show my appreciation for the faculty, students and staff team at the Engine Research Center. In particular, I would like to thank Eric Pomraning, Bert Debusschere, Fritz Bedford and Scott Mason for providing me with insight into DNS and LES, Hao Lu for working on the DNS of decaying isotropic turbulence, and Joshua Leach for being the most efficient system administrator.

Finally I would like to thank all my friends and family, especially my wife Julia, for their love and support.

The research for this work was supported by the National Science Foundation, US Army Research Office and Air Force Research Office.

to my parents, Natalia and Gennadii

Contents

List of Figures

List of Tables

Notation and Symbols

Acronyms

CFL — Courant-Friedrichs-Lewy number

DNS — Direct Numerical Simulation

ERC — Engine Research Center

DIT — Decaying Isotropic Turbulence

LES — Large Eddy Simulation

PDF — Probability Density Function

SGS — Sub-grid Scale

Non-dimensional parameters

Ma — Mach number

Re — Reynolds number

Re_λ — Reynolds number based on Taylor microscale

Pr — Prandtl number

Le — Lewis number

Roman symbols

C_δ — shear layer growth rate constant

$C_{i,\phi}$ — dynamic constant for the subgrid scalar transport model

C_i — dynamic constant for the subgrid scalar dissipation model

C_s — Smagorinsky constant, self-similarity constant

c_k — Kolmogorov constant

D — diffusion coefficient

E — energy

f — passive scalar

G — LES base filter function

G_t — LES test filter function

$\widehat{G}$ — LES test filter function

k — Subgrid-scale kinetic energy, wave number

L_{ij} — LES Leonard term

$L_{i\phi}$ — LES Leonard-type term for SGS scalar flux

L_x — non-dimensional length of domain in x-direction

L_y — non-dimensional length of domain in y-direction

L_z — non-dimensional length of domain in z-direction

p — pressure

r — free-stream velocity ratio in the shear layer

S_{ij} — rate of strain tensor

S_u — velocity derivative skewness

T — temperature

t — time

u — velocity component in x-direction

$\hat{u}$ — Convective outlet velocity

u_i — velocity vector

U — base velocity profile (function of y only)

U_1 — high-speed free-stream velocity

U_2 — low-speed free-stream velocity

v — velocity component in y-direction

w — velocity component in z-direction

x — coordinate direction

x_i — position vector

y — coordinate direction

z — coordinate direction

Greek symbols

α — generic LES model on the test level

α_i — characteristic filter width in the direction of the spatial coordinate i

β — generic LES model on the base level

δ — ratio of characteristic lengths of test and base filters, 1% shear layer thickness

γ — ratio of specific heats

γ_i — Runge-Kutta integration coefficient

Δ — characteristic filter width

δ_{ij} — Kronecker delta

δ_ω — Vorticity thickness

ϵ — Kinetic energy dissipation rate

ϵ_s — SGS kinetic energy dissipation rate

ζ — Runge-Kutta integration coefficient

η — Kolmogorov length scale

θ — SGS scalar variance

κ — dilatational viscosity

λ — Taylor microscale

μ — dynamic viscosity

ν — kinematic viscosity

ν_T — turbulent viscosity

ξ — self-similarity coordinate

Π — energy transter term in one-equation models

ρ — density

σ — shape parameter for the hyperbolic tangent profile,second moment of a filter function

σ_{ij} — stress tensor

$T_{i\phi}$ — LES subgrid scalar transport term on the test level

τ_{ij} — subgrid stress tensor

τ_{iij} — triple-correlation term

$\tau_{i\phi}$ — LES subgrid scalar transport term

ϕ — generic scalar flow variable

χ — Scalar dissipation

χ_r — Resolved scalar dissipation

χ_s — SGS scalar dissipation

Φ — dissipation function

ω — vorticity vector

Auxiliary symbols (ϕ represents a generic variable)

$\widehat{\phi}$ — LES test filtering operation

$\overline{\phi}$ — LES base filtering operation

ϕ' — LES fluctuating component

$\widetilde{\phi}$ — LES Favre averaging

$\langle\phi\rangle$ — ensemble average, average over the entire domain

Chapter 1. Introduction

1.1 Motivation

With the improvement of computational power over last decades it has become more feasible to model complex engineering flows using Computational Fluid Dynamics (CFD). The improvement of computational power is expected to continue which will serve to improve CFD modeling capabilities. However, significant challenges still are expected to remain for an extended period of time. An internal combustion engine (IC engine) is an excellent example of such a challenge due to transient flows, multi-phase media, chemical reactions and high degree of turbulence present in the flow.

The understanding of the role of turbulence in particular is crucial to the prediction of many natural phenomena including combustion, and consequently for improvement of engineering devices.

During the last several decades, Large Eddy Simulation (LES) has become a widely recognized and acknowledged part of CFD, and has been applied to a variety of problems ranging from weather prediction that dates back to original work of Smagorinsky,[64] to IC engine simulations.[59]

The main advantage of LES is that it is capable of capturing the unsteady effects much better than Reynolds-Averaged Navier-Stokes (RANS) approach, and does not require such extensive computational power as Direct Numerical Simulation (DNS). Taking into account this characteristic and the fact that the results obtained by using LES have been found to agree well with the experimental measurements, LES can be regarded as one of the most promising approaches for modeling of highly turbulent unsteady flows in domains with complex geometry.

The essence of the LES approach is the separation of variables of interest such as velocity, temperature, mixture fraction or other passive scalars, into resolved and unresolved parts. The resolved, or large-scale quantities are computed numerically. The unresolved, or subgrid-scale (SGS) quantities are not directly available. Thus the SGS models that use the resolved quantities to model the effect of SGS quantities on the resolved scales must be utilized. SGS model quality is most crucial for any LES computation.

Over the course of the last four decades, many SGS models have been developed. Generally, a model can depend on many parameters some of which have to be tuned "by hand" using some *a priori* available knowledge of the flow that is being modeled. The majority of such parameters are empirical constants that work well for one type of a flow (i.e. homogeneous isotropic turbulence) but might not be valid for another (mixing layer or channel flow). Some of these difficulties are overcome by using so-called one-equation models that employ an additional transport equation for some SGS quantity that is not directly available from the resolved flow. The auxiliary LES quantity is then used in the SGS model thus reducing the number of empirical constants needed. This, in our opinion, is the most promising approach to date, and in this direction we shall pursue our research.

An SGS model, once formulated, needs to be validated. Generally, two approaches are available called *a priori* and *a posteriori* tests. In *a priori* test, the output of a model is directly compared to SGS quantities obtained elsewhere. In *a posteriori* test, the results of the LES simulation are compared to the mean flow statistics obtained elsewhere. Thus, the *a priori* test evaluates the model's ability to directly reproduce the modeled term itself, while *a posteriori* tests evaluates the ability of the model to predict the interaction between resolved and subgrid scales in question.

Unfortunately, the unresolved quantities are difficult to measure directly in experimental setup thus making *a priori* LES model evaluation extremely difficult. An alternative consists of utilizing existing DNS results where all scales are resolved and thus the LES "subgrid"

quantities are available by applying a simple filtering operation. This is the method we are going to use in this work. *A posteriori* tests will be conducted as well.

1.2 Objective and Approach

The main objective of this work is to test and develop LES models for use in CFD. New models will be proposed that close the transport equation for the SGS kinetic energy, LES transport equation for a generic scalar, and the transport equation for the SGS scalar variance. The SGS kinetic energy and SGS scalar variance are two auxiliary LES quantities that are used in one-equation SGS models for the SGS momentum stresses and SGS scalar flux.

After formulating models for the unclosed terms, they are going to be checked *a priori* using the DNS database built at the Engine Research Center (ERC) at University of Wisconsin-Madison. The database includes data for the non-reacting incompressible mixing layer, Couette flow and channel flow. Also, DNS data for decaying isotropic turbulence is going to be used.

The remainder or this document is organized as follows. Chapter 2 provides the necessary LES background. Chapter 3 contains the review of the literature currently available on the subject. Chapter 4 contains the review of the DNS data used for *a priori* testing and some general DNS results. Chapters 5 and 6 contain the same information about models for the SGS scalar flux and SGS scalar dissipation. Chapter 7 contains the formulation and results of *a priori* test for the model of the SGS energy dissipation. Chapter 8 contains the description of the *a posteriori* tests conducted on all three models. Finally, chapter 9 contains the conclusions and description of the future work.

Chapter 2. Background

In this chapter, the fundamentals of LES will be discussed: spatial filters, their properties, and the fundamental LES equations. Also a brief overview of the Self-Similarity assumption will be conducted.

2.1 Spatial filters and their properties

Large-Eddy Simulation technique is based on the decomposition of a spectra of a flow variable into several parts with respect to the wave number. During the simulation, these parts are treated separately and the interaction between them is modeled. The usual number of parts is two, however, splitting the spectra in three parts can be found in literature.[16]

When splitting the spectra of a flow variable ϕ in two parts, the lower wave number part is referred to as resolved and usually is denoted by $\overline{\phi}$, and the upper wave number part is called sub-grid and denoted by ϕ'. It is easy to illustrate using the energy spectrum for isotropic turbulence as an example. The energy containing eddies with wave numbers below some cutoff value are resolved, while eddies above the cutoff wave number curve are modeled (see Figure 2–1).

The separation of the flow field into the resolved, or "filtered", and the subgrid parts is performed using the LES filtering operation, or weighted spatial averaging. The filtered quantities are often referred to as "resolved quantities" since it is customary to define the filter function G in such a way that the support of G, or "LES filter size", has dimensions of one computational cell in the LES simulation. However, the filter size and the computational cell size do not have to be equal. In order to be consistent with the literature, the terms "resolved" and "filtered" are equivalent in this document.

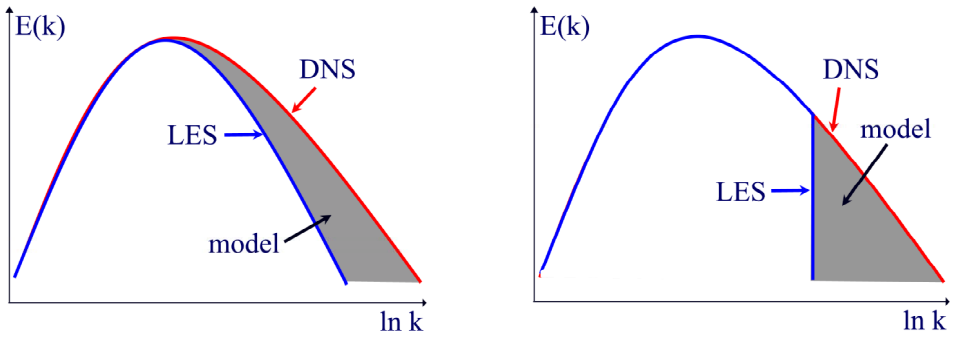

(a) (b)

Figure 2–1: DNS and LES energy spectra for isotropic turbulence for (a) Gaussian filter and (b) Fourier sharp cutoff filter. $E(k)$ represents the energy contained in the eddies with wavenumber k. The cutoff wave number curve may be different for different LES filters (see section 2.1.2).

The shape of the cutoff wave number curve depends on the filter size and shape. In physical space, the flow is resolved to the grid resolution while the sub-grid flow and its effects on the resolved flow are modeled. LES filters are discussed in the next section.

It should be noted that LES filtering is quite different from RANS averaging. The fundamental differences are summarized in the Table 1.

Property	**RANS**	**LES**
$\overline{\phi'} = 0$	true	false
$\frac{\partial \overline{\phi}}{\partial x_i} = \overline{\frac{\partial \phi}{\partial x_i}}$	true	grid and filter dependent
$\overline{\overline{\phi}} = \overline{\phi}$	true	false

Table 1: Difference between RANS averaging and LES filtering

2.1.1 Filtering operation

Formulation

The "LES filter" is defined by the filter function $G(y)$ which must satisfy the condition

$$\int_{\mathbb{R}^3} G(y)\, dy = 1, \tag{2.1}$$

where $\mathbb{R}$ denotes the set of real numbers. For a flow variable ϕ, the filtered and fluctuating components $\overline{\phi}$ and ϕ' are defined as

$$\overline{\phi} = \phi * G = \int_{\mathbb{R}^3} \phi(x) G(y-x)\, dy, \qquad \phi' = \phi - \overline{\phi},$$

where '$*$' denotes the convolution operator.

There are many types of filter functions G used in the LES community. The most common are "box" (or "top-hat") filter, the Gaussian filter, and Fourier sharp cut-off filter.

The box filter. The "box" filter function is given by

$$G(y) = \begin{cases} 0, & \|y\|_\infty > \Delta/2 \\ 1/V, & \|y\|_\infty \leq \Delta/2 \end{cases}, \tag{2.2}$$

where Δ is the characteristic filter length, and V is the filter volume defined as Δ^3.

Gaussian filter. The Gaussian filter function is given by

$$G(y) = \sqrt{A/\pi} \cdot e^{-Ay^2}, \tag{2.3}$$

where the constant A is commonly chosen to be $A = 6/\Delta^2$ to enforce (2.1).[66]

Fourier cut-off filter. Finally, the wave cut-off filter is defined in the Fourier space. For this filter, all wave numbers above a cut-off number, k_c, are modeled, while all wave numbers below are resolved:

$$\hat{G}(k) = \begin{cases} 1, & k \leq k_c \\ 0, & k > k_c \end{cases}, \tag{2.4}$$

Note that there is "duality" between the box filter and the cut-off filter, namely, the cut-off filter is the box filter in Fourier space.

Linear filter. We would like to introduce the linear filter function which is, in the 1-D case, given by

$$G(y) = \begin{cases} 0, & |y| > \Delta/2 \\ 2\Delta - 4|y|, & |y| \leq \Delta/2 \end{cases}, \tag{2.5}$$

and can be called "a triangle filter".[55] In the general case, we can define the linear filter as follows. Let S be a closed convex set in $\mathbb{R}^3$ such that S contains a neighbourhood of the origin. Then we can define a function $f_S(y) = \min_{y \in \alpha S} \alpha$. The linear filter is then defined as

$$G(y) = \max\{0, 1 - f_S(y)\} \cdot \left[\int_S 1 - f_S(y)\, dy \right]^{-1}. \tag{2.6}$$

The set S is the support of G.

2.1.2 Comparison between different filters

Consider a case of a one-dimensional periodic domain of $[0, 2\pi)$ with 64 grid points. Suppose we would like to retain approximately the first sixteen Fourier modes to use in the LES experiment with resolution of 32 grid points in the domain. Then, we assume one of the following filters should be applied:

- A box filter with $\Delta = 8\Delta_g$,
- A linear filter with $\Delta = 8\Delta_g$,
- A Gaussian filter with $\Delta = 8\Delta_g$,
- A cutoff filter with $k_c = 16$.

Here, Δ is the characteristic filter width, $\Delta_g = 2\pi/64$ is the DNS grid spacing, and k_c is the cutoff wave number.

Figures 2–2, 2–3 and 2–4 show behaviour of four different LES filters in real and Fourier space: box, linear, Gaussian and cutoff. Figure 2–2 shows the filters in the real space, Figure 2–3 shows the filters in the Fourier space, and Figure 2–4 shows the decay of the transfer functions together with the slopes -1 and -2 for the exponential decay. The figures illustrate the following filter properties.

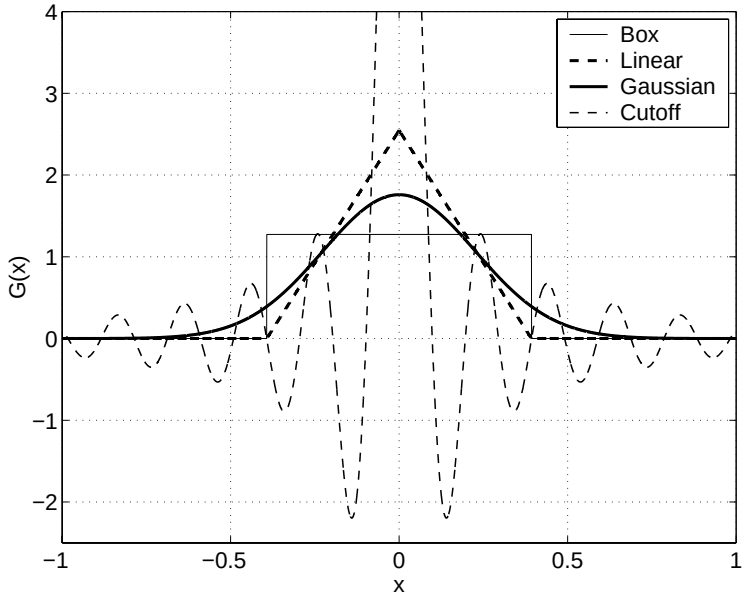

Figure 2–2: LES filters in real space.

The box filter, although the easiest to implement numerically, shows the slowest rate of decay in the Fourier space – $O(1/k)$ (Figure 2–4), where k is the wave number. Moreover, the oscillatory behaviour of the box filter in the Fourier space suggests that additional noise is introduced by non-uniform amplifications of harmonics.

The linear filter might be more feasible than the box filter because it stays positive and shows the faster rate of decay – $O(1/k^2)$ – in the Fourier space. However, it still shows oscillatory behaviour (Figure 2–3).

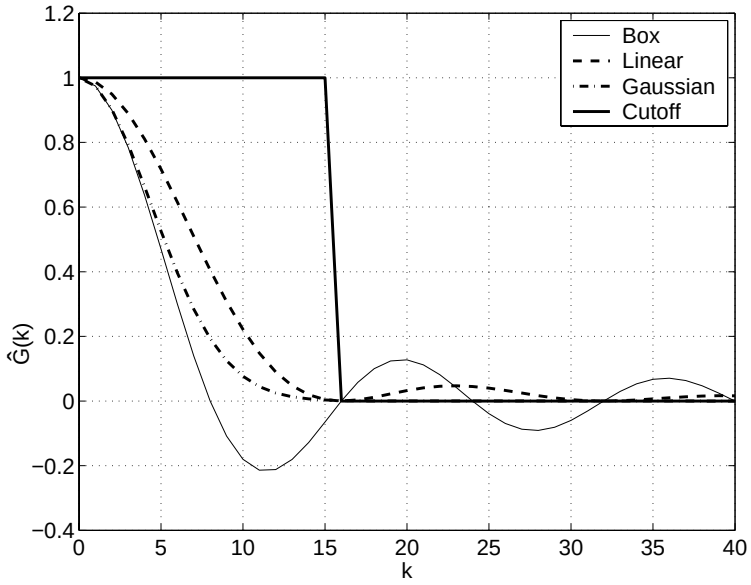

Figure 2–3: LES filters in the Fourier space.

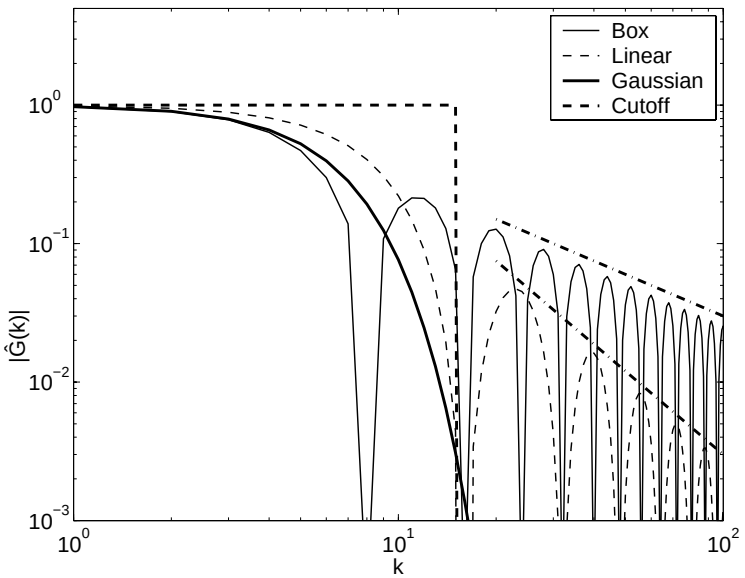

Figure 2–4: Log-log plot of the magnitude of the transfer function $\hat{G}(k)$ for different LES filters. Slopes of -1 and -2 are plotted for comparison.

The Gaussian filter possesses some attractive properties, e.g., it retains its shape in the Fourier space and it's always positive in Fourier space. As shown in the Figure 2–3, it effectively damps out the waves with wave number higher than 11.

Finally, the cutoff filter is the most convenient for the calculations done in the Fourier space, but it shows oscillatory behaviour in the real space.

Thus, for practical use, the Gaussian LES filter is advisable. However, the linear filter is a good "first approximation" to the Gaussian filter, and thus may also be suitable for practical applications. The cut-off filter is very convenient to use in case one conducts a numerical experiment in Fourier space – e.g., LES of decaying isotropic turbulence in a fully periodic domain.

2.1.3 Filtering and differentiation

Note that the spatial differentiation does not necessarily commute with LES filtering operation (2nd row in the Table 1). In general, a numerical error that is referred to as "commutation error", is introduced. It can be verified[70,71] that the difference $\frac{d\overline{f}}{dx} - \overline{\frac{df}{dx}}$ contains the term $\frac{d\Delta(x)}{dx}$ as a multiplicative factor, where $\Delta(x)$ is the local filter width. Thus if $\Delta(x) \equiv \Delta = const$ holds then the filtering operation and differentiation operator do commute.

In practice, however, flow length scales that have to be resolved might vary throughout the domain. A good example of a numerical simulation that requires non-uniform resolution is a boundary layer simulation. A non-uniform grid might be required which could make the filtering procedure that utilizes a spatial filter of a constant size computationally expensive.

As an alternative, one could explicitly calculate the leading term of the commutation error for a certain class of LES filters. Ghosal and Moin[30] suggested that the leading correction term be retained if high-order numerical schemes are used to discretize the LES equations.

The drawback of this approach consists of additional numerical complexities that arise from extra terms in transport equations.

Van der Ven[70] proposed a one-parameter family of filters that commute with differentiation operator up to any desired order. However, this approach is limited to a specific choice of filters and does not address the issue of additional boundary terms that would arise in finite domains. Vasilyev et al.[72] derived a general condition of commutativity for spatial filters and differentiation up to any desired order of the mesh spacing.

It should be noted that the main measure of the quality of filters[67,70,72] was taken to be the closeness of a filter to a sharp cutoff filter. This indeed seems to be the trend in the current literature. One of characteristic features of the cutoff filter is that its filter function G is not non-negative in the real space. This might result in quantities of the type $\overline{\phi\phi} - \overline{\phi}\,\overline{\phi}$ being negative. In particular the "subgrid-scale kinetic energy" $k = \frac{1}{2}(\overline{u_i u_i} - \overline{u}_i \overline{u}_i)$ would admit negative values which is somewhat counter-intuitive and makes some SGS models inapplicable. In our opinion, filtering operation should be regarded as "spatial averaging" as opposed to "removal of higher harmonics".

In this work all computations are performed using linear and box filters, which are positively defined in the physical space.

2.2 LES Governing Equations and Modeled Terms

2.2.1 Conservation equations.

The governing equations for LES are obtained by formally applying the spatial filtering procedure to the fundamental conservation equations. It is implicitly assumed that the filtering operator commutes with temporal and spatial differentiation. Thus, the LES governing equations have the following form.

Continuity:

$$\frac{\partial \overline{\rho}}{\partial t} + \frac{\partial (\overline{\rho}\tilde{u}_i)}{\partial x_i} = 0, \tag{2.7}$$

Momentum:

$$\frac{\partial \overline{\rho}\tilde{u}_i}{\partial t} + \frac{\partial \overline{\rho}\tilde{u}_i\tilde{u}_j}{\partial x_j} = -\frac{\partial \overline{p}}{\partial x_i} - \frac{\partial \overline{\sigma}_{ij}}{\partial x_j} - \frac{\partial \overline{\rho}\tau_{ij}}{\partial x_j}, \tag{2.8}$$

where

$$\sigma_{ij} = -\mu\left[\frac{\partial u_i}{\partial x_j} + \frac{\partial u_j}{\partial x_i}\right] + \left[\frac{2}{3}\mu - \kappa\right] \cdot \frac{\partial u_k}{\partial x_k} \cdot \delta_{ij}.$$

The unclosed term τ_{ij} is referred to as *SGS momentum flux*, and is defined as

$$\tau_{ij} = \begin{cases} \widetilde{u_i u_j} - \tilde{u}_i\tilde{u}_j & \text{if} \quad \rho \neq const \\ \overline{u_i u_j} - \overline{u}_i\overline{u}_j & \text{if} \quad \rho = const \end{cases} \tag{2.9}$$

Scalar transport:

$$\frac{\partial \overline{\rho}\tilde{\phi}}{\partial t} + \frac{\partial \overline{\rho}\tilde{u}_i\tilde{\phi}}{\partial x_i} = \frac{\partial}{\partial x_i}\left[D\overline{\rho}\widetilde{\frac{\partial \phi}{\partial x_i}}\right] - \frac{\partial \overline{\rho}\tau_{i\phi}}{\partial x_i} \tag{2.10}$$

Here, ϕ is a generic scalar, $\tilde{\phi} = \overline{\rho\phi}/\overline{\rho}$ denotes the LES Favre averaging operation, μ denotes the viscosity, κ denotes the dilitational viscosity, and D is the diffusion coefficient. The *SGS scalar flux* $\tau_{i\phi}$ is defined as

$$\tau_{i\phi} = \begin{cases} \widetilde{u_i\phi} - \tilde{u}_i\tilde{\phi} & \text{if} \quad \rho \neq const \\ \overline{u_i\phi} - \overline{u}_i\overline{\phi} & \text{if} \quad \rho = const \end{cases} \tag{2.11}$$

Note that no modeling assumptions have been made yet. The terms that require modeling are momentum SGS flux τ_{ij}, scalar SGS flux $\tau_{i\phi}$ and $\widetilde{\partial\phi/\partial x_i}$, the latter being usually approximated by $\partial\tilde{\phi}/\partial x_i$.[25]

2.2.2 Auxiliary LES equations.

SGS Kinetic Energy

Some closures for the LES transport equations (2.8) and (2.10) require computation of the *SGS kinetic energy*

$$k \equiv \frac{\widetilde{u_i u_i} - \tilde{u}_i \tilde{u}_i}{2}. \tag{2.12}$$

The SGS kinetic energy has been successfully used in modeling τ_{ij}.[35,36,56] In order to calculate k, one can use a number of models or, alternatively, derive a transport equation for k:[55]

$$\frac{\partial \overline{\rho} k}{\partial t} + \frac{\partial \overline{\rho} \tilde{u}_i k}{\partial x_i} = -\left[\overline{u_i \frac{\partial p}{\partial x_i}} - \tilde{u}_i \frac{\partial \overline{p}}{\partial x_i}\right] - \frac{1}{2}\frac{\partial \tau_{iij}}{\partial x_j} + \tilde{u}_i \frac{\partial \tau_{ij}}{\partial x_j} + \left[\overline{u_i \frac{\partial \sigma_{ij}}{\partial x_i}} - \tilde{u}_i \frac{\partial \overline{\sigma}_{ij}}{\partial x_i}\right]. \tag{2.13}$$

For the incompressible case (2.13) simplifies to

$$\frac{\partial k}{\partial t} + \overline{u}_i \frac{\partial k}{\partial x_i} = -\frac{1}{\rho}\left[\overline{u_i \frac{\partial p}{\partial x_i}} - \overline{u_i}\,\overline{\frac{\partial p}{\partial x_i}}\right] - \frac{\partial}{\partial x_j}\left[\frac{1}{2}\tau_{iij} - \overline{u}_i \tau_{ij}\right] + \nu \frac{\partial^2 k}{\partial x_j \partial x_j} - \tau_{ij}\overline{S}_{ij} - \epsilon_s, \tag{2.14}$$

where ν is dynamic viscosity, p is pressure, ρ is density, τ_{iij} is the triple-correlation term and ϵ_s is the SGS dissipation:

$$\tau_{iij} = \overline{u_i u_i u_j} - \overline{u_i u_i}\;\overline{u_j}, \quad \epsilon_s = \nu\left[\overline{\frac{\partial u_i}{\partial x_j}\frac{\partial u_i}{\partial x_j}} - \overline{\frac{\partial u_i}{\partial x_j}}\;\overline{\frac{\partial u_i}{\partial x_j}}\right], \quad \overline{S}_{ij} = \frac{1}{2}\left[\frac{\partial \overline{u}_i}{\partial x_j} + \frac{\partial \overline{u}_j}{\partial x_i}\right].$$

Note that in the equation (2.14), four out of five terms on the right-hand side have to be modeled since they cannot be computed using the resolved velocity field. A number of models were discussed in Pomraning.[55] The most successful are presented later in section 3.4.

The purpose of adding the transport equation for the SGS kinetic energy is to enforce a budget on the energy flow between the resolved and unresolved scales. The models that utilize either equation (2.13) or (2.14) are referred to as "one-equation models", as opposed to "zero-equation models" that do not require solution of an additional transport equation.

SGS Scalar Variance

An analogous equation can be derived if we try to model scalar-related quantities. In this instance, the transport equation describes the time evolution of the *SGS scalar variance* for the scalar ϕ:

$$\theta = \overline{\phi\phi} - \overline{\phi}\,\overline{\phi}. \tag{2.15}$$

For incompressible flow, the transport equation for θ is

$$\frac{\partial\theta}{\partial t} + \overline{u}_i\frac{\partial\theta}{\partial x_i} = \underbrace{D\frac{\partial^2\theta}{\partial x_i\partial x_i}}_{\text{diffusion}} - \underbrace{2D\left[\overline{\frac{\partial\phi}{\partial x_i}\frac{\partial\phi}{\partial x_i}} - \frac{\partial\overline{\phi}}{\partial x_i}\frac{\partial\overline{\phi}}{\partial x_i}\right]}_{\text{SGS scalar dissipation } \chi_s} - \underbrace{2\tau_{i\phi}\frac{\partial\overline{\phi}}{\partial x_i}}_{\text{source}}, \tag{2.16}$$

where D is the diffusion coefficient. See Appendix A for the derivation.

2.3 Self-Similarity assumption and beyond

2.3.1 Self-Similarity

The idea of scale invariance, or self-similarity, dates back to Richardson[60] who made the following qualitative assessment of a turbulent flow:

> *Big whorls have little whorls*
> *Which feed on their velocity,*
> *And little whorls have smaller whorls*
> *And so on to viscosity (in the molecular sense).*

Quantitatively, there exists a range of scales (the inertial range) in which effects of viscosity, boundary conditions, and large-scale structures are not important. This leads to a well-known Kolmogorov universal power-law spectrum:[38]

$$E(k) = c_k\epsilon^{2/3}k^{-5/3}, \tag{2.17}$$

where c_k is the Kolmogorov constant, k is the wavenumber, and ϵ is the dissipation rate of kinetic energy by molecular viscosity ν.

However, Large-Eddy Simulation procedure exhibits a clear need for deeper insight into relationship between large and small scales. In the part of the current literature that deals with similarity models, an assumption is made that a turbulent flow exhibits a fractal-like behaviour in the inertial range of scales thus allowing one to extrapolate the information obtained from resolved scales to the unresolved scales. This is usually done by using an additional filtering procedure — so-called test-level filtering as opposed to base-, or grid-level filtering. Then the information about interaction between the grid and test-level flow fields is used to model the interaction between the grid and subgrid-level flow field.

2.3.2 Test-level filtering and Self-Similarity

In LES simulations, the resolved flow field is assumed to be already filtered using some base-level filter with kernel $G_1(x)$ and characteristic filter width Δ_1. In order to obtain a test-level filtered field, a filter with kernel $G_t(x)$ is applied to the base-level field. The resulting test-level field can also be theoretically obtained by applying some filter with kernel $G_0(x)$ and characteristic width Δ_0 to the fully resolved flow. Figure 2–5 shows the relation between functions G_1, G_0 and G_t.

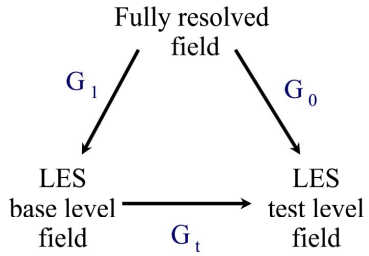

Figure 2–5: Connection between filters G_1, G_0 and G_t.

It is assumed that both filter G_0 and the base filter G_1, although different in size, behave

in a similar way regarding the unresolved quantities. This is not correct for an arbitrary filter shape. Carati and Vanden Eijnden[6] argue that in order for the self-similarity assumption to be valid, the functions $G_1(x)$ and $G_0(x)$ have to be similar:

$$G_1(x) = \delta^{-d}\, G_0(x/\delta), \tag{2.18}$$

where $\delta = \Delta_0/\Delta_1$ is the ratio of characteristic filter widths, and d is the number of dimensions in the simulation. Thus G_1 and G_0 must have identical shapes and must differ only by their characteristic width.

This can be achieved if we make the following assumption. Instead of just test and base filters, we can consider an infinite chain of filters $\mathbb{G}_n$, defined by the function G_t and ratio δ in the following fashion:

$$\mathbb{G}_n(x) = \delta^{nd} G_t\left(\delta^{-nd} x\right), \qquad n = 0, 1, \ldots, \infty. \tag{2.19}$$

Then we can define another sequence of filters G_n as

$$G_n(x) = \mathbb{G}_n(x) * \mathbb{G}_{n+1}(x) * \mathbb{G}_{n+2}(x) * \ldots \tag{2.20}$$

The sequence G_n contains the base filter G_1 and the test filter G_0. This construction is illustrated in Figure 2–6.

The whole chain of self-similar filters is defined by the filter function G_t and the ratio of characteristic widths δ. It should be noted that the shape of G_1 and G_0 is hardly affected by the shape of G_t due to the fact that G_1 and G_0 are obtained by infinite number of convolutions of G_t with itself.

Thus the most crucial information supplied by the function G_t is its characteristic width Δ_t. Having Δ_t, one can calculate the characteristic widths Δ_0 and Δ_1. Namely, using the fact that the characteristic width of $\mathbb{G}_n(x)$ equals $d_n = \Delta_t/\delta^n$ and $\Delta_0 = \sum_{n=0}^{\infty} d_n$ we can find Δ_0 as a sum of infinite geometric series with common ratio $1/\delta$:

$$\Delta_0 = \sum_{n=0}^{\infty} \frac{\Delta_t}{\delta^n} = \Delta_t \cdot \frac{\delta}{\delta - 1}.$$

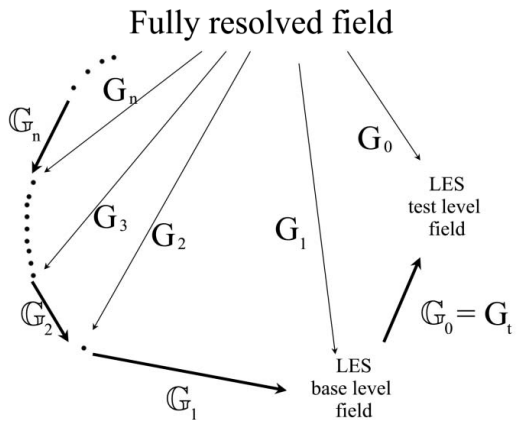

Figure 2–6: Chain of self-similar filters defined by G_t and δ.

Then we can find Δ_1 by definition $\Delta_1 = \Delta_0/\delta = \Delta_t/(\delta - 1)$.

One can obtain a similar expression for second moments. If we define the second moment of a filter function $G(x)$ as

$$\sigma = \int x^2 G(x)\, dx,$$

then using similar argument as above, we obtain

$$\sigma_0 = \sum_{n=0}^{\infty} \frac{\sigma_t}{\delta^{2n}} = \sigma_t \cdot \frac{\delta^2}{\delta^2 - 1}, \qquad \sigma_1 = \sigma_t \cdot \frac{1}{\delta^2 - 1},$$

where σ_n and σ_t denote the second moment of filter functions G_n and G_t correspondingly.

For the Gaussian and cut-off filter types, the dependence (2.19) can be computed analytically, while for the box or the linear filter, a numerical approximation must be applied. For the Gaussian G_t, the corresponding base filter is also Gaussian, and for a cutoff G_t the base filter is also a cutoff filter.

These speculations can be summarized in the following.

Proposition. In order for self-similarity assumption to be valid, we should regard the LES simulation setup as follows. Given the basic filter shape G_t with characteristic width Δ_t, and the test-to-base ratio of characteristic widths δ, the base and test filter functions can be

found as

$$G_1(x) = C \cdot G_t(x/\delta) * G_t(x/\delta^2) * G_t(x/\delta^3) \ldots, \qquad G_0(x) = G_t(x) * G_1(x), \tag{2.21}$$

where C is the normalization constant. The characteristic widths of G_1 and G_0 are

$$\Delta_1 = \Delta_t \cdot \frac{1}{\delta - 1}, \qquad \Delta_0 = \Delta_t \cdot \frac{\delta}{\delta - 1},$$

and the second moments are

$$\sigma_1 = \sigma_t \cdot \frac{1}{\delta^2 - 1}, \qquad \sigma_0 = \sigma_t \cdot \frac{\delta^2}{\delta^2 - 1}.$$

2.3.3 So, which filter should be used?

Since one of the corollaries of the above proposition is that the base and test filter shapes do not heavily depend on the shape of G_t, we can choose G_t almost arbitrarily. We propose to use the linear filter as G_t for the following reasons:

- Positively defined in real space. This ensures that quantities of the type $\overline{aa} - \overline{a}\,\overline{a}$ stay non-negative. Quantities of this type include SGS kinetic energy k and SGS scalar variance θ which are important for some SGS models.

- The decay rate in Fourier space is $O(k^{-2})$ and the Fourier transform of G_t stays non-negative in Fourier space. This is better than the commonly used box filter and improves the computational stability.

- Linear G_t has finite support as opposed to Gaussian filter thus yielding a cheaper implementation for non-uniform grids.

Further in this document, the linear G_t is used by default.

Chapter 3. Literature Review

3.1 Introduction

The LES governing equations section described in the section 2.2 have several unclosed terms:

- The SGS momentum flux $\tau_{ij} = \overline{u_i u_j} - \overline{u}_i \overline{u}_j$;
- The SGS scalar flux $\tau_{i\phi} = \overline{u_i \phi} - \overline{u}_i \overline{\phi}$;
- The filtered kinetic energy dissipation $\overline{\epsilon} = \nu \overline{\frac{\partial u_i}{\partial x_j} \frac{\partial u_i}{\partial x_j}}$;
- The SGS kinetic energy dissipation $\epsilon_s = \nu \left[\overline{\frac{\partial u_i}{\partial x_j} \frac{\partial u_i}{\partial x_j}} - \frac{\partial \overline{u}_i}{\partial x_j} \frac{\partial \overline{u}_i}{\partial x_j} \right]$;
- The filtered scalar dissipation $\overline{\chi} = 2D \overline{\frac{\partial \phi}{\partial x_i} \frac{\partial \phi}{\partial x_i}}$;
- The SGS scalar dissipation $\chi_s = 2D \left[\overline{\frac{\partial \phi}{\partial x_i} \frac{\partial \phi}{\partial x_i}} - \frac{\partial \overline{\phi}}{\partial x_i} \frac{\partial \overline{\phi}}{\partial x_i} \right]$.

In this chapter, we shall consider the models available in the literature with brief evaluation. In the following chapters we shall propose some new models for the last three terms.

3.2 Evaluation criteria for SGS models

In our opinion, a good SGS model should in general possess the following properties:

- The model should use some form of local adaptation as opposed to *a priori* defined coefficient.
- The model should have some theoretical foundation in order to accurately predict physical aspects of the modeled flow.

These can be regarded as a starting point in construction of an LES model. In addition, the following should hold for a good model for τ_{ij}:

1. The model should be capable of predicting *backscatter phenomena* – energy flow from small to large scales that is physically possible and thus has to be numerically available.

2. The model for τ_{ij} should be *realizable*,[63] i.e., the following should hold:

   (a) $\tau_{[\ddot{\imath}]} \geq 0$,

   (b) $\tau_{ij}^2 \leq \tau_{[\ddot{\imath}]}\tau_{[jj]}$

   (c) $\det(\tau_{ij}) \geq 0$.

Bracketed indices indicate that the index does not participate in summation.

3.2.1 *A priori* and *a posteriori* tests

In order to compare different models we need some uniform evaluation criteria. The standard evaluation consists of two tests: *a priori* test and *a posteriori* test.

To perform an *a priori* test, one takes available DNS data, performs filtering operation to obtain the base-filtered LES flow field and then compares the exact quantity with the model expression obtained from the filtered DNS field.

To perform an *a posteriori* test, one needs to implement the model in question into a computer code and perform a full-scale LES simulation. Then the results of the LES simulation can be compared to the results of DNS or experimental measurements.

The two mentioned tests are very different in nature. The *a priori* test procedure evaluates the ability of the model in question to predict the exact behaviour of the modeled quantity, while the a posteriori test evaluates the model's ability to accurately predict the interaction between the modeled and resolved quantities.

In this work, we shall use *a priori* and *a posteriori* tests to evaluate the newly proposed models for $\tau_{i\phi}$, ϵ_s and χ_s.

3.3 Dynamic modelling

The drawbacks of universal coefficient models can be partially mended by applying the dynamic modeling idea proposed by Germano et al.[29] The dynamic modeling consists of applying the test filter to the resolved quantities, and trying to determine the local value of the model constant using the test-level flow field. Let us illustrate this approach using an abstract LES model for the SGS scalar flux term $\tau_{i\phi}$.

A generic example of a dynamic model

Let the test filtered quantity ϕ be denoted by $\widehat{\overline{\phi}}$, where "$\widehat{\ }$" signifies the application of the filter with kernel G_t to the base-level variable $\overline{\phi}$ (see section 2.3.2). Consider the base-level transport term $\tau_{i\phi} = \overline{u_i\phi} - \overline{u}_i\overline{\phi}$, and the test-level transport term $T_{i\phi} = \widehat{\overline{u_i\phi}} - \widehat{\overline{u}_i}\widehat{\overline{\phi}}$.

The quantities $T_{i\phi}$ and $\tau_{i\phi}$ are connected by the Germano identity:[29]

$$L_{i\phi} = T_{i\phi} - \widehat{\tau_{i\phi}}, \tag{3.1}$$

where $L_{i\phi}$ is the Leonard-type term which is defined as

$$L_{i\phi} = \widehat{\overline{u}_i\overline{\phi}} - \widehat{\overline{u}_i}\widehat{\overline{\phi}}. \tag{3.2}$$

Note that the Leonard term (3.2) can be readily determined from the resolved velocity and scalar fields in an LES simulation. Thus, the equation (3.1) relates the unknown terms at two scales to a known term $L_{i\phi}$.

The next step in formulation of a dynamic LES subgrid model requires postulating models for the two transport terms on the base and test levels:

$$\tau_{i\phi} \approx C_{[i,1]}\beta_{[i\phi]}; \qquad T_{i\phi} \approx C_{[i,2]}\alpha_{[i\phi]},$$

where $C_{i,2}$ and $C_{i,1}$ are scaling coefficients, and $\alpha_{i\phi}$ and $\beta_{i\phi}$ are the model terms for $\tau_{i\phi}$ and $T_{i\phi}$ obtained, e.g., by dimensional argument. A good example of α and β would be

$$\alpha_{i\phi} = -\Delta^2 |\overline{S}_{ij}| \frac{\partial \overline{\phi}}{\partial x_i}; \qquad \beta_{i\phi} = -\widehat{\Delta}^2 |\widehat{\overline{S}}_{ij}| \frac{\partial \widehat{\overline{\phi}}}{\partial x_i}.$$

Substituting these modeled subgrid transport terms into the Germano identity yields

$$L_{i\phi} = C_{[i,2]} \alpha_{[i,\phi]} - \widehat{C_{[i,1]} \beta_{[i,\phi]}}. \tag{3.3}$$

The equation (3.3) cannot provide us with values of $C_{i,2}$ and $C_{i,1}$ since it gives us only 3 equations for 6 unknowns. Moreover, the equation (3.3) is an integral equation because, in general, $C_{i,2}$ and $C_{i,1}$ are functions of space. These types of equations do not always have a unique solution, and can be numerically expensive to solve. Therefore, some additional assumptions on $C_{i,2}$ and $C_{i,1}$ have to be made.

The most common assumption made about $C_{i,2}$ and $C_{i,1}$ is that, although functions of space, they are exactly the same. This reduces the number of unknowns to 3 instead of 6, yet some difficulties still remain, e.g., it requires some work to determine if the resulting integral equation is solvable at all.

To simplify the problem much further, the second simplifying assumption is made – that $C_{i,1}$ and $C_{i,2}$ "vary slowly in space" and thus $C_{i,1}$ can be taken outside of the integral. This simplifies the integral equation (3.3) to a simple algebraic equation resulting in

$$C_{i,1} = C_{i,2} = \frac{L_{i\phi}}{\alpha_{[i,\phi]} - \widehat{\beta_{[i,\phi]}}}.$$

Thus the problem has been reduced to three algebraic equations with three unknowns. To reduce the problem further, we can used the technique proposed by Lilly.[40] We define the square of the modeling error as

$$Q = (L_{i\phi} - CM_{i\phi})^2,$$

where $M_{i\phi} = \alpha_{i\phi} - \widehat{\beta_{i\phi}}$. Minimizing Q reduces the three equations to the following algebraic expression with the single constant C:

$$C = \frac{L_{i\phi} M_{i\phi}}{M_{k\phi} M_{k\phi}}.$$

3.4 Models for SGS Momentum Flux τ_{ij}

3.4.1 Smagorinsky model

The Smagorinsky model was originally proposed in 1963 by Smagorinsky:[64]

$$\tau_{ij} \approx \nu_T \overline{S}_{ij} \tag{3.4}$$

where

$$\nu_T = -2(C_s\Delta)^2|\overline{S}_{ij}|, \qquad \overline{S}_{ij} = \frac{1}{2}\left(\frac{\partial \overline{u}_i}{\partial x_j} + \frac{\partial \overline{u}_j}{\partial x_i}\right), \qquad |\overline{S}| = \sqrt{2\overline{S}_{ij}\overline{S}_{ij}},$$

Δ is the characteristic filter width, and C_s is a user-specified coefficient. The usually prescribed value for C_s is 0.17.[57]

Note that the trace of the rate of strain tensor $\overline{S}_{ij}$ is zero which implies existence of at least one negative entry on the diagonal. The actual SGS stress tensor has all non-negative diagonal entries, given a non-negative filter. To remedy this problem, the model was modified by Akselvoll and Moin[2] by adding the trace of the SGS stress tensor to the model in order to make the trace of the modeled tensor positive:

$$\tau_{ij} \approx \nu_T \overline{S}_{ij} + \frac{1}{3}\delta_{ij}\tau_{kk}, \tag{3.5}$$

The model is based upon the assumption that the subgrid stress tensor τ_{ij} is a scalar multiple of the resolved rate of strain tensor $\overline{S}_{ij}$. This assumption, based on a molecular transport analogy, cannot be justified, in fact, the assumed scaling is poor.[41] According to recent measurements,[4,9] the probability density function (PDF) of the angle between the most extensive directions of τ_{ij} and $\overline{S}_{ij}$ has a mean that ranges from 28 to 45 degrees.

In addition, the Smagorinsky model requires *a priori* knowledge of the flow in order to define the coefficient C_s. Moreover, being defined, C_s might not be valid for all parts of the flow in case of complex flow geometry.

Another theoretical weakness (and the major numerical strength) of the Smagorinsky model is that it is purely dissipative. The energy flows only in one direction — from resolved to sub-grid scales. This greatly enhances the numerical stability of the modeling procedure. On the other hand, the presence of the "backscatter" — energy transport from sub-grid to resolved scales — has been verified by numerous experimental and numerical studies, and thus should be available.

3.4.2 Dynamic localization model

A natural way to improve the Smagorinsky model for τ_{ij} is to try to utilize the SGS kinetic energy k in computing the eddy viscosity ν_T. The following model has been used:[35,62]

$$\tau_{ij} \approx -(C_s\sqrt{k}\Delta)\overline{S}_{ij} + \frac{1}{3}\delta_{ij}k, \tag{3.6}$$

where C_s is calculated using the Dynamic Modeling approach. The model (3.6) has been applied to variety of problems[22,35,36] and the same form of the eddy viscosity has been used to close LES equations for scalar transport as well. The computational cost of this model is higher but, comparing to the zero-equation eddy-viscosity models, the performance of the model is superior due to the using of the SGS kinetic energy k.

3.4.3 Gradient, or Clark model

The gradient model relates the subgrid stress tensor to the gradient of velocity by the *gradient form of viscosity*:[15,37]

$$\tau_{ij} \approx 2\alpha_{[i]}\frac{\partial\overline{u}_i}{\partial x_k}\frac{\partial\overline{u}_j}{\partial x_k}, \tag{3.7}$$

where

$$2\alpha_{[i]} = \int_{-\infty}^{\infty} G(x) x_i^2 \, dy.$$

The bracketed indices indicate that the quantity does not participate in the index summation.

The gradient model correlates well with the actual subgrid stress tensor. The reason for this is that the model represents the first term in the series:[76]

$$\begin{aligned} \overline{fg} - \overline{f}\,\overline{g} &= 2\alpha_{[k]} \frac{\partial f}{\partial x_k} \frac{\partial g}{\partial x_k} + \frac{2^2}{2!} \alpha_{[k_1]} \alpha_{[k_2]} \frac{\partial^2 f}{\partial x_{k_1} \partial x_{k_2}} \frac{\partial^2 g}{\partial x_{k_1} \partial x_{k_2}} + \dots \\ \dots &+ \frac{2^n}{n!} \alpha_{[k_1]} \dots \alpha_{[k_n]} \frac{\partial^n f}{\partial x_{k_1} \dots \partial x_{k_n}} \frac{\partial^n g}{\partial x_{k_1} \dots \partial x_{k_n}} + \dots . \end{aligned} \tag{3.8}$$

Unfortunately, in the incompressible case, using this model to close the LES scalar transport equation results in negative diffusion in at least one direction everywhere in the domain and thus if unchecked the model may become unstable. This has been demonstrated by Leonard[39] using the 3-D Gaussian filter function

$$G(y) = \frac{1}{\sigma\sqrt{\pi}} e^{-|y|^2/\sigma^2}.$$

The gradient scalar flux model becomes

$$\tau_{i\phi} \approx \frac{\sigma^2}{2} \frac{\partial \overline{u}_i}{\partial x_k} \frac{\partial \overline{\phi}}{\partial x_k}.$$

We make use of the following identity for incompressible flows:

$$\frac{\partial}{\partial x_i} \left(\frac{\partial \overline{u}_i}{\partial x_j} \frac{\partial \overline{\phi}}{\partial x_j} \right) = \overline{S}_{ij} \frac{\partial^2 \overline{\phi}}{\partial x_i \partial x_j}.$$

After substituting the model into the transport equation for a passive scalar in an incompressible flow and adopting the notations of Leonard,[39] we obtain

$$\frac{\partial \overline{\phi}}{\partial t} + \overline{u}_i \frac{\partial \overline{\phi}}{\partial x_i} = -\frac{\sigma^2}{2} \, \overline{S}_{ij} \, \frac{\partial^2 \overline{\phi}}{\partial x_i \partial x_j} + \kappa \frac{\partial^2 \overline{\phi}}{\partial x_k \partial x_k}, \tag{3.9}$$

where κ is the diffusion coefficient. Transforming to principle coordinates of $\overline{S}_{ij}$, x'_j, we find that the first term on the right-hand side of (3.9) becomes

$$-\frac{\sigma^2}{2} \overline{S}_{ij} \frac{\partial^2 \overline{\phi}}{\partial x_i \partial x_j} = -\frac{\sigma^2}{2} \left(\overline{\alpha} \frac{\partial^2 \overline{\phi}}{\partial x'^2_1} + \overline{\beta} \frac{\partial^2 \overline{\phi}}{\partial x'^2_2} + \overline{\gamma} \frac{\partial^2 \overline{\phi}}{\partial x'^2_3} \right),$$

where the eigenvalues $\overline{\alpha}$, $\overline{\beta}$, $\overline{\gamma}$ of $\overline{S}_{ij}$ satisfy

$$\overline{\alpha} \geq \overline{\beta} \geq \overline{\gamma}, \qquad \overline{\alpha} + \overline{\beta} + \overline{\gamma} = 0.$$

Thus, along the stretching direction(s) x_1' and possibly x_2', we have effectively negative diffusion. This decreases the wave number for some small-scale perturbations which leads to propagation of numerical instabilities from the high to the low end of the spectrum and eventual blow-up.

A number of stabilizing methods could be proposed, but, as argued by Leonard,[39] the result may strongly depend on the stabilization scheme used.

3.4.4 Vortex-based model

For a Fourier cutoff filter, Misra and Pullin[44] proposed a so-called vortex-based model for SGS stress τ_{ij}. The subgrid scale motions in a computational cell are modeled as a stretched 2D vortex the main axes of which can be aligned in a variety of ways referred to as orientation models. The model reads

$$\tau_{ij} = (\delta_{ij} - e_i^v e_j^v)k \equiv (\delta_{ij} - e_i^v e_j^v) \int_{\omega_c}^{\infty} E(\omega)\, d\omega, \tag{3.10}$$

where ω is a wavenumber, $E(\omega)$ is the energy spectrum, ω_c is the cutoff wavenumber, and $(\delta_{ij} - e_i^v e_j^v)$ is the orientation tensor.

3.4.5 Similarity models

The scale-similarity model for τ_{ij} is given by

$$\tau_{ij} \approx C_s(\widehat{\overline{u}_i \overline{u}_j} - \widehat{\overline{u}}_i\, \widehat{\overline{u}}_j). \tag{3.11}$$

The Dynamic procedure can also be used to obtain the coefficient C_s locally but that requires another test filter which is larger than the one used in the model.

The similarity model has been evaluated numerically and experimentally[41] and was found to perform much better than the viscosity-type models. A mixed model — sum of similarity and viscosity models — was also considered[41] and was found to perform equally well but be more stable due to the higher energy dissipation because of the extra viscosity.

Okon'go and Bellan[49] present *a priori* evaluation of SGS models using DNS of temporal mixing layer with evaporating droplets. Again, similarity and Clark models were found to perform much better than Smagorinsky model. The Clark model was found to be preferable because the similarity model coefficient depends on the test-to-base filter size ratio.

3.4.6 A Dynamic One-Equation Non-Viscosity Model

Pomraning and Rutland[56] proposed a simple yet very efficient dynamic model for τ_{ij} that does not rely on the introduction of an analog of turbulent viscosity. Instead, τ_{ij} is modeled as the Leonard term L_{ij} rescaled by the ratio of traces of τ_{ij} and L_{ij}:

$$\tau_{ij} \approx \left(\frac{2k}{L_{kk}} \right) L_{ij}. \tag{3.12}$$

The trace of τ_{ij}, which equals $2k$, is readily available provided we solve the transport equation for the k.

The formal derivation of (3.12) begins with the hypothesis $\tau_{ij} \approx c_{ij} k$, then the dynamic procedure is formally applied to yield (3.12). However, the model can be viewed as a next generation of self-similarity models with a particular form of the scaling coefficient.

The model was tested and compared to DNS results for the case of isotropic turbulence, and a very good agreement between the DNS and LES was found. Here we list pros and cons that are important in our opinion.

Pros:

- No coefficients to tune manually;

- Allows backscatter;
- Using the separate transport equation for the SGS kinetic energy k allows to enforce the energy budget;
- The model is realizable;
- Excellent agreement in a priori tests — better than dynamic localization model (3.6).

Cons:

- Since the term that is responsible for the energy transfer between the resolved and subgrid scales is $\tau_{ij}S_{ij}$, it can be deduced that in order for the SGS kinetic energy k to be non-zero it has to be non-zero to begin with. In short, k needs itself to grow.
- The need to develop a procedure for specifying initial amount of k for all applications, and the inlet value of k for the problems with open domains.
- An additional unclosed term is introduced in the k-equation: ϵ_s.

The most serious problem, in our opinion, seems to be the specification of inlet values of k for the flow simulations in unclosed domains. At the present time we have not yet developed a uniform algorithm to solve this difficulty and every case should be tuned manually. Varying the initial amount of k for box turbulence case (Section 8.2) did not dramatically affect the kinetic energy decay rate. On the other hand, varying the inlet value of k in quasi-steady problems such as the dump combustor simulation seems to affect the mixing rates and, as a consequence, most of the scalar-related statistics.

3.5 Models for SGS Energy Dissipation ϵ_s

Not many models can be found in the literature for the SGS energy dissipation term ϵ_s. A common model is[62,65]

$$\epsilon_s \approx C\frac{k^{3/2}}{\Delta},$$

where C is a model constant. The model is "derived" using dimensional analysis. The advantage of this model is that it is simple and guarantees positive dissipation when it is well-defined. The disadvantage of this model is that it requires *a priori* knowledge of the modeled flow to prescribe a value for C. Ghosal et. al.[62] proposed to use the Dynamic Procedure to find local value for C. *A posteriori* tests were conducted for the case of decaying isotropic turbulence and backward-facing step and results were compared to experimental data,[1,18] LES and experimental data matched well. For the case of decaying isotropic turbulence, total energy decay rate and energy spectra were compared to experimental on a non-log-log plot, which is discussed later in the chapter 8.

3.6 Models for SGS Scalar Flux $\tau_{i\phi}$

3.6.1 Viscosity models

To model the subgrid transport of a passive scalar ϕ, one might try a Smagorinsky-type model that is given by

$$\tau_{i\phi} = -C_s\Delta^2|\overline{S}_{ij}|\frac{\partial\overline{\phi}}{\partial x_i}, \tag{3.13}$$

where C_s is, again, a model constant.

Moin et.al.[46] proposed an eddy diffusivity model for the subgrid energy flux $q_i = \overline{\rho}(\widetilde{u_iT} - \tilde{u_i}\tilde{T})$, where $\tilde{\phi} = \overline{\rho\phi}/\overline{\rho}$ is the Favre averaged quantity:

$$q_i = -\overline{\rho}\frac{\nu_T}{\mathrm{Pr}_t}\frac{\partial\tilde{T}}{\partial x_i}.$$

The subgrid Prandtl number Pr_t is determined using the dynamic model, and $\nu_T = -C\Delta^2|\tilde{S}_{ij}|$ is the subgrid viscosity. Pierce and Moin[53] used the dynamic idea to determine the coefficient C_s.

Pallares and Davidson[51] applied the gradient model to calculate the SGS heat fluxes in stationary and rotational square duct flows, while using the Menon model (3.6) for the SGS momentum flux.

Although the dynamic determination of the scaling constant seems to improve the result dramatically, it still does not eliminate the main flaw of the model (3.13) which is the assumption that the gradient of the resolved scalar field scales well with the subgrid scalar transport term. This is studied in detail later in the chapter 5.

3.6.2 Gradient and similarity models

Okon'go and Bellan[49] compared *a priori* the performance of three types of models: Smagorinsky model (3.13), gradient (Clark) model

$$\tau_{i\phi} \approx C\Delta^2 \frac{\partial \overline{u}_i}{\partial x_k} \frac{\partial \overline{\phi}}{\partial x_k}, \tag{3.14}$$

and self-similarity model

$$\tau_{i\phi} \approx C_s(\widehat{\overline{u}_i \overline{\phi}} - \widehat{\overline{u}}_i \, \widehat{\overline{\phi}}). \tag{3.15}$$

Corresponding modeling approaches were employed for momentum equation closure. They report that similarity and Clark models were found to perform much better than Smagorinsky model for the energy and species SGS fluxes as well as for the momentum fluxes. As with the momentum flux, the Clark model was found to be preferable because the similarity model coefficient depends on the test-to-base filter size ratio.

3.6.3 Stretched-vortex model

An extension of the stretched-vortex model (3.10) to the SGS scalar flux has been proposed by Pullin.[58] The final model for the subgrid flux of a passive scalar ϕ can be expressed as

$$\tau_{i\phi} = -\mu_{ij}\frac{\partial\overline{\phi}}{\partial x_j}, \qquad \mu_{ij} = \frac{1}{2}kT_t(\delta_{ij} - e_i^v e_j^v), \tag{3.16}$$

where k is the subgrid energy, $(\delta_{ij} - e_i^v e_j^v)$ is the unitary operator that rotates the vortex axes to laboratory axes, and $T_t = \gamma\Delta/\sqrt{k}$ is a typical eddy turnover time where the constant γ is chosen to be 1. The results shown[58] predict that, for the "box" turbulence case, the ratio of $\tau_{i\phi}$ to the squared product of the scalar gradient with the dissipation length of the turbulence is asymptotic to a nearly constant value 0.36 for large Reynolds numbers.

The vortex-based models show promise but their validation[44,58] has been performed using the sharp cutoff filter and spectral numerical scheme or sharp cutoff filter for both spectral and finite-difference numerical scheme.[73] We can argue that the stretched-vortex model, although promising, requires further *a posteriori* validation for cases with complex geometries and large Reynolds numbers.

3.7 Models for SGS Scalar Variance θ and SGS Scalar Dissipation χ_s

SGS scalar variance and SGS scalar dissipation are often required together in combustion applications. The SGS variance is employed in the PDF methods when computing the equilibrium mixture composition, while the SGS dissipation rate can be used to obtain the SGS chemical time scale. Since the two quantities are often used simultaneously, the models employed often look alike. This is why we feel that we can group models for these two terms in the same section.

Pierce and Moin[53] used the following model:

$$\tilde{\chi} \approx \overline{\rho}\alpha_t \frac{\partial\tilde{\phi}}{\partial x_i}\frac{\partial\tilde{\phi}}{\partial x_i},$$

where $\alpha_t = C_\alpha \Delta^2 |\tilde{S}|$ is taken from the model for the SGS scalar flux $\tau_{i\phi} = -\overline{\rho}\alpha_t \frac{\partial\tilde{\phi}}{\partial x_i}$, and is determined using the Dynamic Procedure.

The SGS variance was computed using the following model

$$\theta = C\Delta^2 \frac{\partial\tilde{\phi}}{\partial x_i}\frac{\partial\tilde{\phi}}{\partial x_i}.$$

Tilde denotes Favre spatial average.

Cook and Bushe[19] used

$$\overline{\rho\chi} \equiv \overline{\rho D \frac{\partial\phi}{\partial x_i}\frac{\partial\phi}{\partial x_i}} \approx C\ \overline{\rho}\ D(\tilde{T})\ \frac{\partial\tilde{\phi}}{\partial x_i}\frac{\partial\tilde{\phi}}{\partial x_i},$$

where the coefficient C was determined to be correct in average using the scalar energy spectrum of isotropic turbulence at high Reynolds number with a Schmidt number near unity.[69] The following is used:

$$C = \frac{\left\langle \overline{\rho D \nabla\phi\cdot\nabla\phi} \right\rangle}{\left\langle \overline{\rho} D(\tilde{T}) \nabla\tilde{\phi}\cdot\nabla\tilde{\phi} \right\rangle} \approx \frac{\left\langle \overline{\nabla\phi\cdot\nabla\phi} \right\rangle}{\nabla\overline{\phi}\cdot\nabla\overline{\phi}} = \frac{\int_0^\infty k^2 E_\phi(k)\ dk}{\int_0^\infty k^2 \hat{G}(k) E_\phi(k)\ dk},$$

where $\hat{G}$ is the Fourier transform of the filtering function G, k is the wavenumber, and E_ϕ is the scalar energy spectrum. The predicted values for C range from 1.5 to 3.

Another model for $\overline{\chi}$ is the one derived using the analogy with momentum equation closure:[33]

$$\overline{\chi} \approx \frac{1}{\mathrm{Pr}} \cdot \frac{\epsilon}{k} \cdot \theta. \tag{3.17}$$

Similarity models for the SGS scalar variance were explored by Cook and Riley:[21]

$$\theta \approx C_s(\widehat{\overline{\phi}\,\overline{\phi}} - \widehat{\overline{\phi}}\,\widehat{\overline{\phi}}).$$

The suggested value for the scaling constant was 1 when the ratio of test-to-base filter width was 1.8. Subsequently, an effort was made to calculate a scaling constant in self-similarity models using an assumed spectrum.[20]

3.8 Concluding remarks

Based on *a priori* testing on the DNS data described in the Chapter 4, we can draw several conclusions about the SGS models that are currently used in the literature.

- **Eddy-viscosity models**. Perform consistently bad in a priori tests, due to the fact that the resolved gradient (resolved strain directions) does not align with the SGS scalar flux (principal directions of SGS stress). Changing the user-specified coefficient in these models may provide the correct rate of the energy transfer between the scales, but the actual prediction of the subgrid structures remains of a poor quality.

- **Scale-similarity models**. Perform much better *a priori* than the eddy-viscosity models due to fractal (self-similar) nature of the turbulence. These models can be not dissipative enough in a posteriori tests which might lead to blow-ups.

- **One-equation models**. Perform much better than the zero-equation models. Pose a new difficulty — proper model for energy dissipate from the subgrid scales.

It was found that similarity-type models, in general, tend to underpredict the rate of growth of the initial instabilities thus producing the delay in the development of turbulent structures, e.g., in mixing layer or boundary layer. In our opinion, this caused by the fact that the test-filtering procedure tends to eliminate the initial instabilities from the flow, and as a consequence, from the model.

Chapter 4. DNS data and general results

4.1 Motivation: *a priori* tests

A priori evaluation of a model means comparison of the actual value of the modeled term and the model output using data from DNS or experimental measurements. Since experimental data with resolution close to Kolmogorov scale is not readily available from the literature, we confine ourselves to using available DNS data.

The data used in our *a priori* tests covers four different flows: decaying isotropic turbulence (DIT) with a passive scalar, planar channel flow, planar Couette flow and spatially developing mixing layer. All flows are incompressible. The DIT results have been generated by Hao Lu at ERC, the channel and Couette flows have been modeled by Bert Debusschere,[24] and the incompressible mixing layer has been simulated by Scott Mason[42] at ERC. The four data sets provide us with different types of simulated flows: isotropic (DIT), pressure-driven (channel), shear driven (Couette) and free shear flow with strong mean shear (mixing layer). This enables us to *a priori* test the models in different regimes, and also give us some idea about models' near-wall performance.

4.2 Decaying Isotropic Turbulence with passive scalar

4.2.1 Introduction

By decaying isotropic turbulence (DIT) we mean the flow that has zero mean velocity, homogeneous and isotropic, i.e., statistical characteristics of the velocity field depend neither

on the point in the flow nor the direction of measurements.

Numerical simulation of decaying isotropic turbulence, although somewhat impractical for engineering applications, became a *de facto* standard test case for *a posteriori* LES model evaluation. This might be attributed to the fact that of all turbulent flows, the decaying isotropic turbulence case is one of the most well-known. A lot of theoretical results are available,[32,57] and some widely recognized measurements and DNS simulation results are available in current literature as well.[8,17,18]

4.2.2 Experimental and theoretical results

The most cited experimental paper on the subject is by Comte-Bellot and Corrsin.[18] There, the isotropic turbulence is approximated by the grid-generated turbulence: a uniform stream of velocity U_0 =10 m/s is passed through a grid which is characterized by the grid spacing $M = 2$ in. In the laboratory frame, the flow is statistically stationary and statistics vary only in x-direction (flow direction). In the frame moving with the mean velocity U_0, the turbulence is (to an adequate approximation) homogeneous, and it evolves with time ($t = x/U_0$).

In the paper, measurements were conducted at three downstream locations: $tU_0/M = 42, 98$, and 171. Energy spectra are given for all three locations, and many important parameters are tabulated including the velocity RMS $\sqrt{\langle u_1^2 \rangle}$.

Recent measurements by Cerutti and Meneveau[8] provide similar data for higher values of Reynolds number Re_λ.

Generally two types of comparison to the experimental data can be made to evaluate model performance *a posteriori*. We can compare the simulation results to the measured values of

- Energy spectrum for different times, or, more specifically, for different values of Re_λ,
- Rate of decay of kinetic energy in time.

Matching energy spectra at different times is more suitable for DNS rather than LES[75] since LES and DNS energy spectra are quite different for non-cutoff filters. This can be illustrated by plotting the energy spectra for the resolved and filtered flow fields (see Figure 4–1).

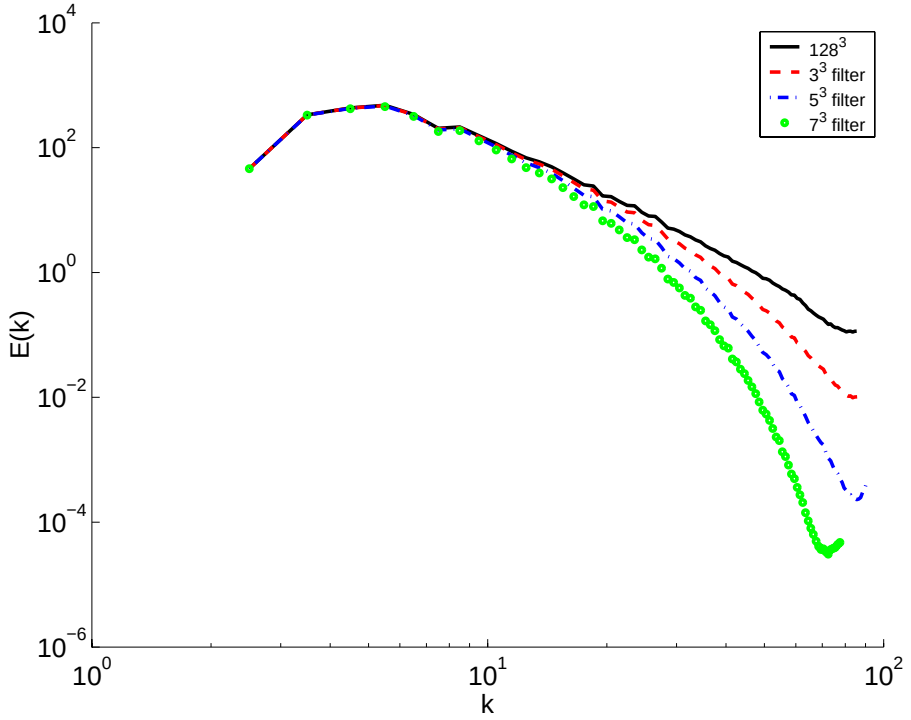

Figure 4–1: Energy spectra for resolved[75] and filtered flow fields using filters of various size.

Thus the main comparison we are going to make is matching the energy decay rate in time. This is indeed a good test for both models for the SGS stress τ_{ij} and SGS energy dissipation ε. This particular test evaluates the ability of both models to manage the energy budget between resolved and unresolved scales on one hand, and unresolved and viscous scales on the other hand. Energy transfer rates on both levels are closely related and both models must perform accurately to reproduce the experimental results.

In the current literature, when the LES of DIT is performed, usually the simulations results are compared to the experimental measurements of Comte-Bellot and Corrsin[18] on a non-logarithmic plot.[22,62] The type of comparison we are going to make differs from the one

usually performed.

In an earlier paper,[17] Comte-Bellot and Corrsin's measurements suggested that the total energy decays as a power law which, in the laboratory frame, can be written

$$\frac{K}{U_0^2} = A\left[\frac{x - x_0}{M}\right]^{-n}, \tag{4.1}$$

where K is the kinetic energy, U_0 is the freestream velocity, A is a constant, x is the streamwise coordinate, x_0 is the virtual origin, and M is the grid spacing.

In Comte-Bellot and Corrsin,[18] only three sets of measurements are available for the case $M = 2$ in. We can extract the total energy values in two ways: either numerically integrate the given energy spectra, or use the given RMS value $\sqrt{\langle u_1^2 \rangle}$ and the isotropy assumption which yields

$$\frac{1}{2}\langle u_i u_i \rangle = \frac{3}{2}\langle u_1^2 \rangle = \int_0^\infty E(k)\, dk \equiv E.$$

After curve fitting with (4.1), the former way yields $n = 1.295$, and the latter yields $n = 1.32$. In both cases, all three points lie virtually on a straight line on the log-log plot (see Figure 4–2).

In general, the decaying isotropic turbulence exhibits two different types of behaviour: inertia-dominated and viscosity-dominated.[57] For the inertia-dominated period, only experimental measurements are known. The total kinetic energy clearly exhibits the power-law decay similar to (4.1). Both Comte-Bellot and Corrsin's data[18] and Cerutti and Meneveau's[8] data suggest $n = 1.29$. The values of the decay exponent n between 1.15 and 1.45 are reported in the literature but it's been suggested[45] that nearly all of the data are consistent with $n = 1.3$.

The energy decay rate for the viscosity-dominated ("final") period can be obtained analytically from the Karman-Howarth equation that describes the time evolution of a longitudinal autocorrelation function.[32] With the inertial term omitted, this equation admits a self-similar solution which yields $E \sim t^{-5/2}$ and $n = 2.5$ which is in excellent agreement with

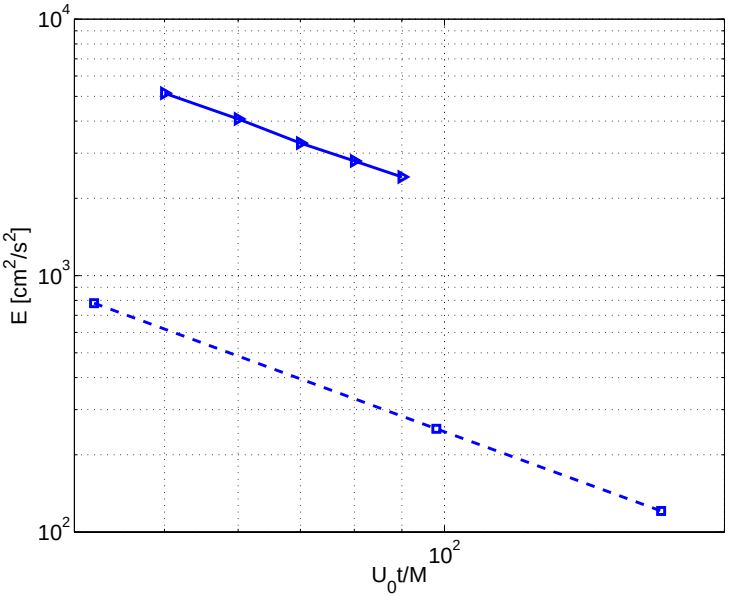

Figure 4–2: Decay rate of kinetic energy in decaying isotropic turbulence: Comte-Bellot and Corrsin[18] (squares) and Cerutti and Meneveau[8] (triangles).

experimental data. It is emphasized that this solution applies to very low Reynolds numbers – much lower than is generally of interest.

Thus, instead of trying to match the experimental results for the energy decay rate and power spectra, we are going to try to match the energy decay rate given by the power law (4.1) with $n = 1.3$ for the inertia-dominated period and $n = 2.5$ for the viscosity-dominated period.

It should be noted, though, that in general the power-law exponent $n(t)$ can depend on time and, most notably, on the shape of the initial power spectrum at low wavenumbers.[12,61] The precise scaling laws of $n(t)$ is a subject of ongoing research. For example, Chasnov[11] presents a total of four scaling laws — two for high Re_λ and two for low, — and observes that the high-Re_λ scaling occurs for $\mathrm{Re}_\lambda > 30$ while the low-Re_λ scaling requires $\mathrm{Re}_\lambda < 1$.

4.2.3 Direct Numerical Simulation

Flow field

In order to simulate the decaying isotropic turbulence a pseudo-spectral code was used. The velocity field was initialized using the deterministic forcing scheme by Overholt and Pope.[50] The following values were used:

$$T_f^* = 0.4, \quad \zeta = 0.25, \quad \alpha = 0.70.$$

Here, $T_F^* = \tau/\tau_\eta$ is the ratio of the forcing time scale τ to the Kolmogorov time scale τ_η, ζ is the parameter that determines the abruptness of the forcing cut-off function (minimum value for ζ was found to be 0.2 experimentally), and α is a damping coefficient introduced in order to achieve statistical stationarity as soon as possible and to minimize the amount of oscillation in the system.

The simulations started out with a quiescent velocity field and then the forcing was introduced. The forcing was applied until Re_λ reached the value of approximately 96, then the forcing was turned off and the flow was allowed to relax to $\mathrm{Re}_\lambda = 70.33$, at which time a passive scalar field was introduced. The simulation then proceeded until the Reynolds number dropped to about 8.9, at which time the simulation was stopped.

It should be noted that the simulation size was limited by the memory and time requirements. The value of the kinematic viscosity ν was set to 0.0014. The physical size of the domain was set to $2\pi \times 2\pi \times 2\pi$, and the computational grid had 128 nodes in every direction. Theoretically, this limited us to Reynolds numbers Re_λ less than 60 (Pope[57] gives even stronger restriction $\mathrm{Re}_\lambda \leq 40$).

We picked eight different realizations of the flow for DNS validation and *a priori* testing of LES models. The information about the chosen snapshots is given in the Table 2. The snapshots DIT-1, 3 and 4 are chosen in order to compare the statistics from the DNS to the measurements by Comte-Bellot and Corrsin.[18] The snapshot DIT-2 is chosen in order to

Dataset name	**Timestep #**	**Normalized time** t/τ_0	**Reynolds number** Re_λ	**Skewness** S_u
DIT-1	1	0.0	70.34	−0.4832
DIT-2	101	0.035	68.57	−0.4825
DIT-3	301	0.1053	65.40	−0.4810
DIT-4	701	0.2457	59.89	−0.4837
DIT-5	1501	0.526	50.40	−0.4949
DIT-6	2901	1.018	39.58	−0.4875
DIT-7	9201	3.23	25.00	−0.4941
DIT-8	72001	25.27	10.01	−0.4161

Table 2: Summary of snapshots from the DNS of decaying isotropic turbulence. The highest Reynolds number reached by forcing was approximately 96. The scalar field was introduced at $\mathrm{Re}_\lambda = 70.34$.

investigate the mechanism of early scalar field development. The next three (DIT-4, 5 and 6) are chosen to represent the period of energy decay which is still dominated by inertia yet has a Reynolds number higher than 20. The last two snapshots (DIT-7 and DIT-8) were chosen to represent the transition between the inertial and final periods of decay in the flow.

The velocity derivative skewness

$$S_u = \frac{1}{3}\left[\frac{\langle S_{11}^3\rangle}{\langle S_{11}^2\rangle^{3/2}} + \frac{\langle S_{22}^3\rangle}{\langle S_{22}^2\rangle^{3/2}} + \frac{\langle S_{33}^3\rangle}{\langle S_{33}^2\rangle^{3/2}}\right]$$

was chosen as the measure of nonlinear energy transfer from low to high wave numbers. It is evident from the table 2 that S_u has reached its asymptotic value of approximately -0.48 before the samples were taken. Thus the flow can be considered fully developed by the time we introduce the passive scalar.

Figures 4–3 and 4–4 show the general statistics of the DNS run. Figure 4–3a shows the log-log plot of the total energy decay in time. The rate of decay appears to be very close to exponential with the exponent $n = 1.7$, which lies close to the acceptable range reported in the literature. Note that the simulation did not seem to reach the final period of decay with theoretically expected $n = 2.5$. In fact, the decay exponent appears to wander away from 2.5 at the end of the simulation, as it is shown in the Figure 4–3b. The decay exponent at

the time t_k was estimated using the following formula:

$$n(t_k) \approx \frac{\ln E(t_k) - \ln E(t_{k+1})}{\ln t_{k+1} - \ln t_k},$$

where the subscripts indicate the timestep number. It should be noted that $n(t)$ becomes almost a constant after approximately three turnover times and remains such until 12 turnover times. This is consistent with results of Ristorcelli and Livescu,[61] who argue that the asymptotic value of $n(t)$ depends on the values of the infrared exponent in the initial power spectrum of the flow, but did not report the results after the ten turnover times.

Figures 4–4a and 4–4b present the evolution of the Reynolds number Re_λ in time and the ratio of the grid size Δ to the Kolmogorov length scale η in time. At $\mathrm{Re}_\lambda = 70$ we have $\Delta \approx 2.75\eta$, which is not as strict as Pope's restriction $\Delta \approx 2.1\eta$,[57] but approximately after one turnover time, Pope's conditions is satisfied and we can consider the simulation to be fully resolved.

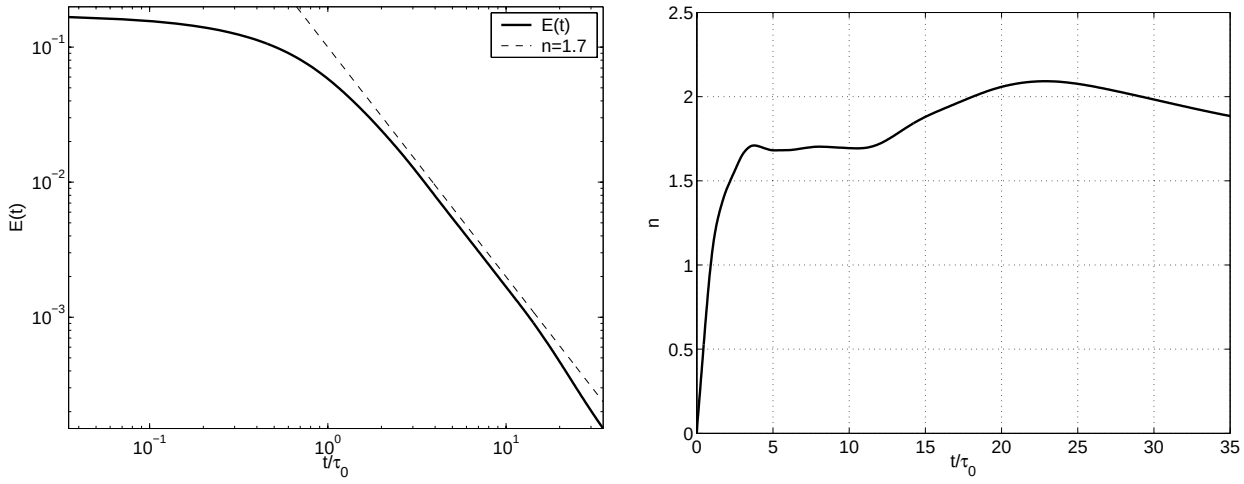

(a) (b)

Figure 4–3: DNS of decaying isotropic turbulence. (a) The decay of total kinetic energy in time on a log-log plot. For reference, the slope -1.7 is plotted. (b) Evolution of the decay exponent in time. The time is normalized by initial eddy turnover time τ_0.

Figure 4–5 shows power spectrum computed from DNS for the first five data sets along with the power spectrum given by Comte-Bellot and Corrsin.[18] A good match between the experimental data and the DNS is observed.

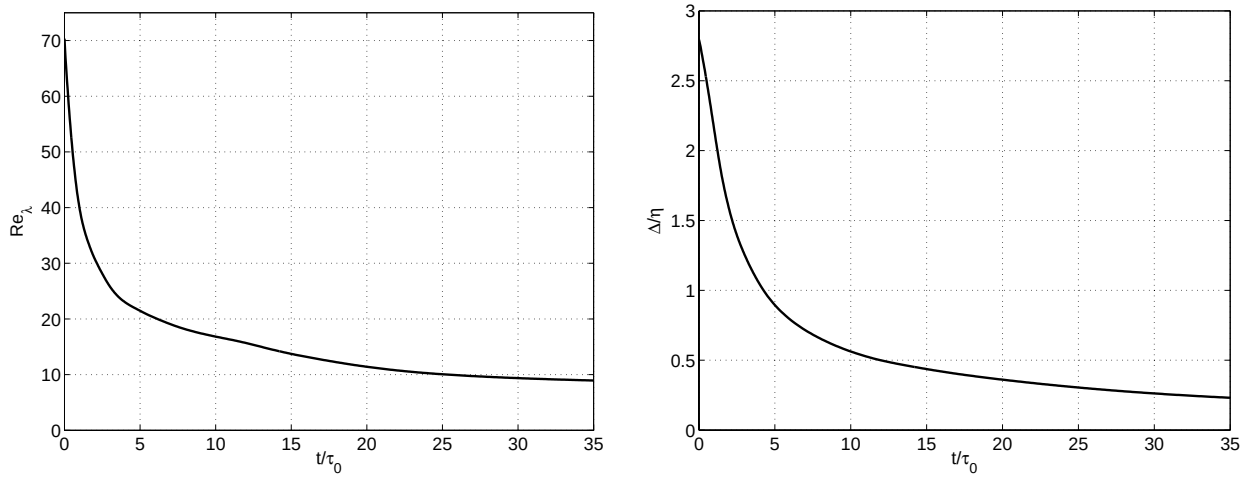

(a) (b)

Figure 4–4: DNS of decaying isotropic turbulence. (a) Evolution of the Reynolds number Re_λ in time. (b) Evolution of the ratio of the grid spacing Δ to Kolmogorov scale η in time. The time is normalized by initial eddy turnover time τ_0.

The given observations enable us to conclude that the performed DNS resolves all important length scales of the flow and accurately simulates the decaying isotropic turbulence. Thus it can be used order to evaluate the LES models *a priori*.

Scalar field

At the time when $\mathrm{Re}_\lambda = 70.34$, a passive scalar ϕ was introduced into the already developed flow. The initial scalar field was given by the following:

$$\phi(x, y, z) = e^{-10r^2}, \qquad r = \min(|z - \pi/2|, |z + \pi/2|).$$

This evolution of the scalar is illustrated by shadowgraphs of the scalar given in the Figure 4–6. The six snapshots of the scalar field correspond to the data sets DIT-1, and DIT-3 through DIT-6.

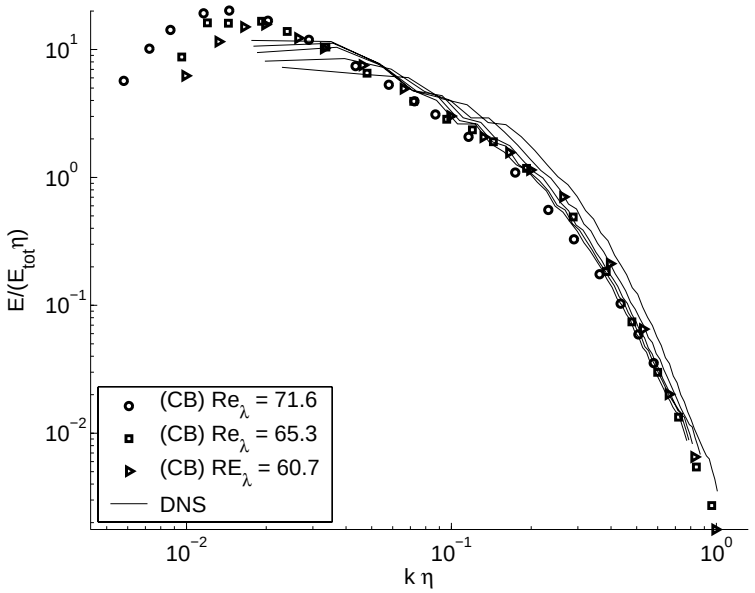

Figure 4–5: Normalized power spectra for decaying isotropic turbulence. Symbols represent the data from experimental measurements by Comte-Bellot and Corrsin[18] for three different values of Re_λ. Lines represent the spectra obtained from DNS for the first five entries in the Table 2.

4.3 Channel and Couette flows

Channel and Couette flows were simulated by Bert Debusschere[24] at the ERC. The geometry of both flows included periodicity in both x and z directions (streamwise and spanwise), and isothermal no-slip walls in the y direction (cross-flow, or transverse). The temperature ϕ was introduced as a passive scalar with values $\phi = 0$ at the bottom wall ($y = 0$) and $\phi = 1$ and the top wall ($y = 2$). The walls were isothermal and had constant temperature. All length units were normalized by the channel half-width δ. We label temperature ϕ to be consistent with other data sets.

Parameter	**Channel flow**	**Couette flow**
$\mathrm{Re} = \mathrm{U}\delta/\nu$	3300	3000
$\mathrm{Re}_\tau = \mathrm{u}_\tau\delta/\nu$	205.26	170.22
Domain size	12 x 2 x 5	12 x 2 x 5
Grid points	256 x 200 x 128	255 x 200 x 128

Table 3: DNS of channel and Couette flows — summary.

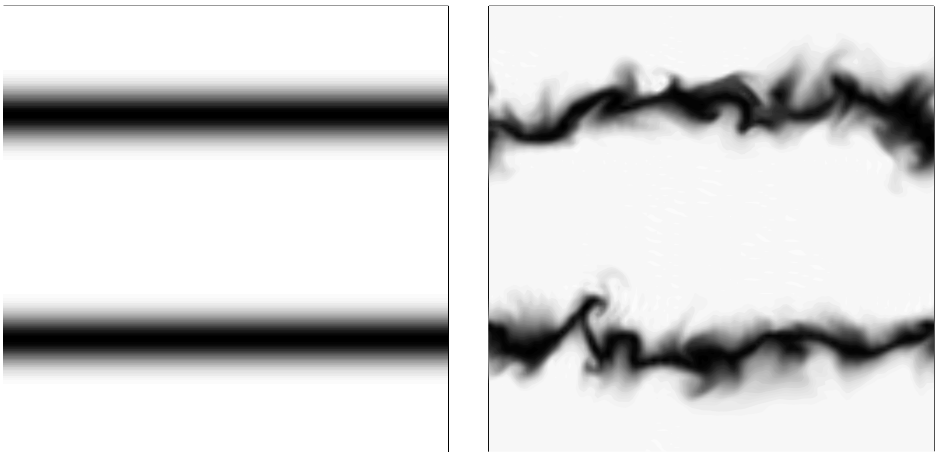

(a) DIT-1, $\mathrm{Re}_\lambda = 70.34$

(b) DIT-3, $\mathrm{Re}_\lambda = 65.4$

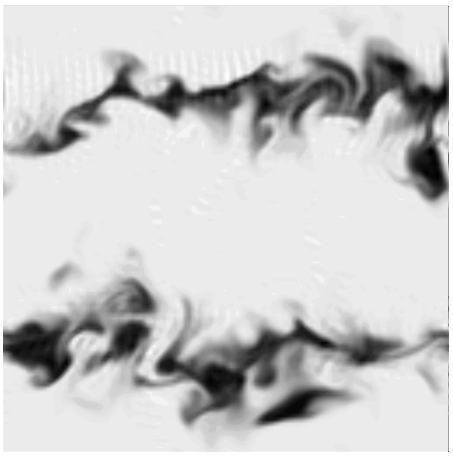

(c) DIT-4, $\mathrm{Re}_\lambda = 59.89$

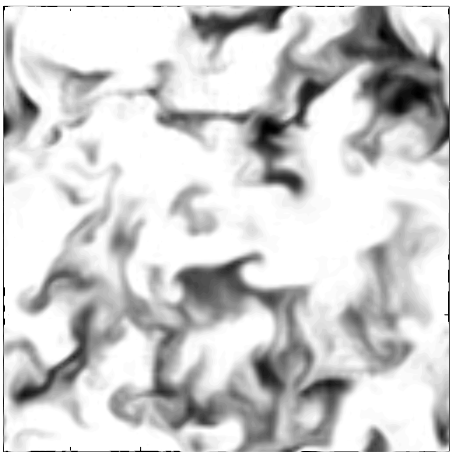

(d) DIT-5, $\mathrm{Re}_\lambda = 50.40$

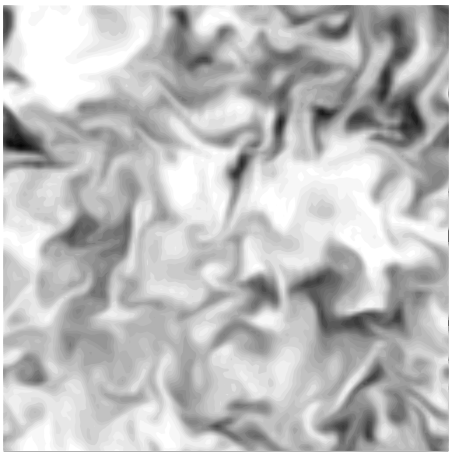

(e) DIT-6, $\mathrm{Re}_\lambda = 39.58$

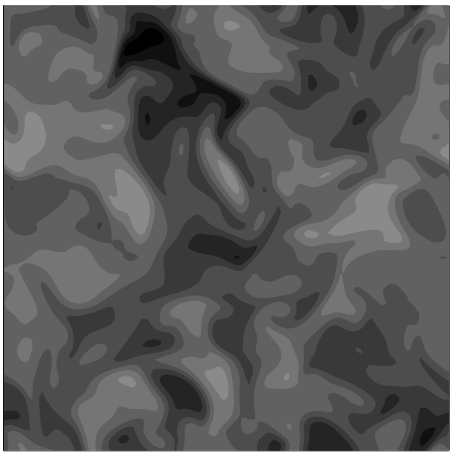

(f) DIT-7, $\mathrm{Re}_\lambda = 25.00$

Figure 4–6: Decaying isotropic turbulence: passive scalar field at various stages (plane $y = 0$).

The Table 3 provides the parameter summary for these DNS datasets. In the Table, δ is the channel half-width, U is the mean velocity and the friction velocity is defined as

$$u_\tau = \sqrt{\frac{\tau_w}{\rho}} = \sqrt{\frac{\mu}{\rho}\frac{\partial \langle u \rangle}{\partial y}\bigg|_{y=0}}.$$

The Figures 4–7 and 4–8 show snapshots of the temperature fields. The flow direction is from left to right.

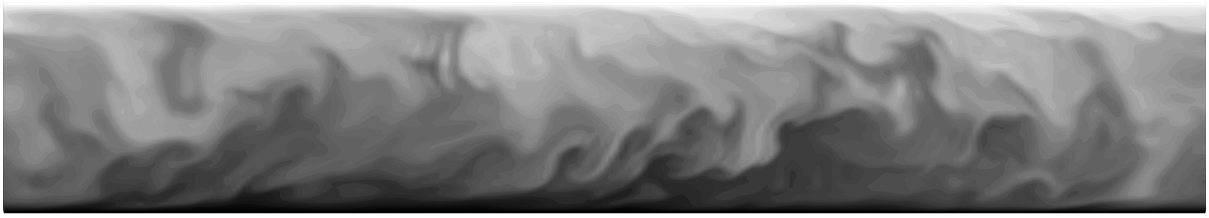

Figure 4–7: Temperature snapshot from DNS of channel flow. The plane $z = 0$ is shown, the boundary conditions on the temperature are $\phi = 0$ at the bottom wall and $\phi = 1$ at the top wall.

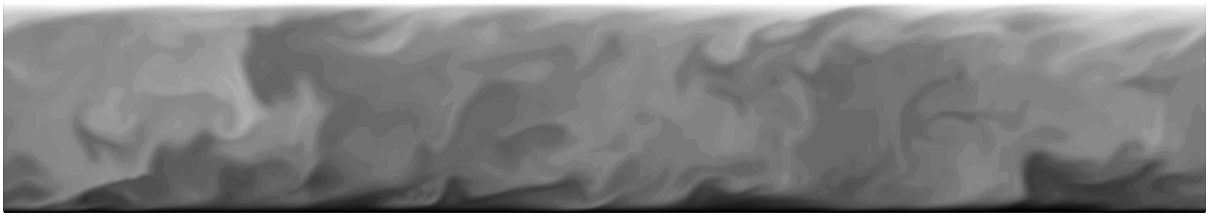

Figure 4–8: Temperature snapshot from DNS of Couette flow. The plane $z = 0$ is shown, the boundary conditions on the temperature are $\phi = 0$ at the bottom wall and $\phi = 1$ at the top wall.

Figure 4–9 shows the near-wall velocity profiles. It should be noted that using the computational grid that was equally spaced in the cross-flow direction gave somewhat insufficient resolution in the viscous sub-layer, where $u_+ = y_+$, thus resulting in under-prediction of the mean streamwise velocity in the viscous sub-layer. Nevertheless, both simulations recover the law of the wall velocity profile in the log-layer and were considered feasible for the *a priori* model testing.

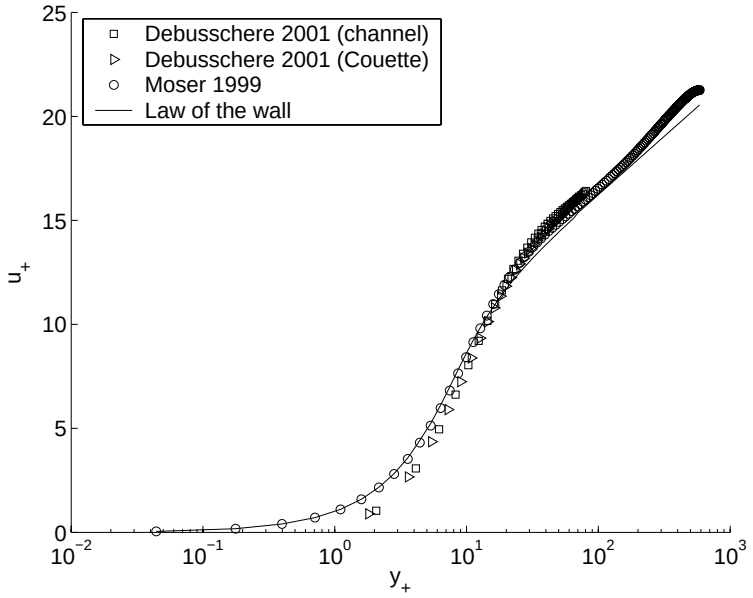

Figure 4–9: Near-wall mean velocity profile from Debusschere[24] for channel and Couette flows. For comparison, the velocity profile from DNS by Moser et al.[47] ($\mathrm{Re}_\tau = 590$) and law of the wall[74] are plotted.

4.4 Incompressible non-reacting mixing layer

The DNS data for incompressible non-reacting mixing layer was provided by Scott Mason.[42] Figure 4–10 shows the schematic for the computational domain. A brief description of the DNS experiment follows.

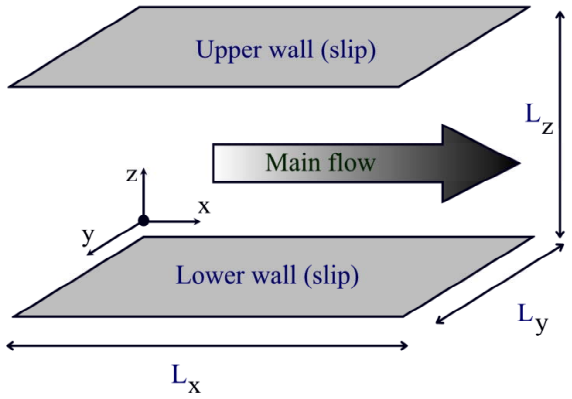

Figure 4–10: Schematic of the computational domain for the mixing layer.

The domain dimensions in x, y, and z directions are denoted by L_x, L_y and L_z. For the

particular simulation, $L_x = 120$, $L_y = 60$, $L_z = 9.6$. All lengths are non-dimensionalized by the inlet vorticity thickness

$$\delta_\omega = \frac{\Delta U}{[du/dy]_{\max}},$$

where maximum is taken over a plane $x = \text{const}$.

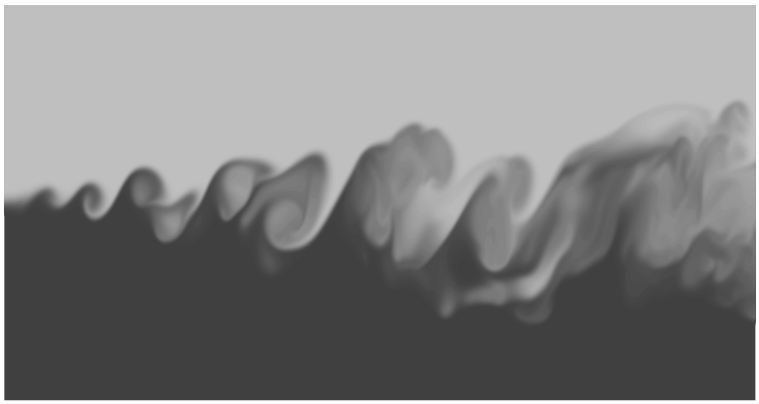

Figure 4–11: Temperature snapshot from DNS of mixing layer.[42]

The streamwise component of the velocity vector is specified at the inlet using the non-dimensional hyperbolic tangent profile

$$U(y) = u_m + \frac{\Delta U}{2} \cdot \tanh \frac{y - L_y/2}{\sigma}, \tag{4.2}$$

where u_m is the mean velocity, ΔU is the velocity difference and σ is a shape parameter. For the DNS simulation, the parameters were $u_m = 1$, $\Delta U = 0.5$, and $\sigma = 0.5$. These parameters resulted in high-speed and low-speed free-stream velocities of $U_1 = 1.5$, $U_2 = 0.5$, an inlet vorticity thickness $\delta_{\omega_0} = 1$, and velocity ratio of $r = 1/3$. The temperature inlet profile is given by

$$\phi(y) = \tanh \frac{y - L_y/2}{\sigma}.$$

To introduce the instabilities in the mixing layer at the inlet, two pairs of counter-rotating streamwise vortices were placed at the inlet plane on top of the two-dimensional inlet flow. Also, perturbations were superimposed on the inlet velocity base profile (4.2). The perturbations corresponded to the fundamental (the most unstable) mode of the base profile, also

known as the Kelvin-Helmholtz mode. These perturbations facilitated the vortex roll-up in the mixing layer.

The non-dimensional Reynolds number based on the inlet vorticity thickness was set to 200.

4.5 Properties of flow quantities observed from DNS data

4.5.1 Results from the literature

In the literature, a lot of effort is put into understanding the interaction between various flow characteristics: strain, vorticity, scalar gradient, alignment between principal strain directions and vorticity, strain and scalar gradient, etc. Before going any further, we would like to investigate the validity of some alignment assumptions from the current literature using the available data from DNS.

The following observations can be found in the current literature:

1. Vorticity tends to align with the intermediate strain direction, s_2.
2. Passive scalar gradient tends to align with the most compressive strain direction, s_3.
3. The scalar variables determined by the small-scale structures of the flow have a log-normal PDF.

The above trends were observed in DNS of decaying isotropic turbulence — incompressible[3] and compressible;[54] DNS two-dimensional mixing systems;[34] measurements in turbulent atmospheric boundary layer[9] and channel flow,[4] and many others.

4.5.2 Alignment of strain, vorticity and scalar gradient

In order to make a quantitative assessment of the alignment between two vector functions of space, one can compute a PDF of a cosine of the angle between the vectors in question. This is done due to the fact that bins of equal width for the cosine function translate into bins of equal surface area on the unit sphere in three-dimensional space. An angle between two vectors in 3-D, one of which can be fixed pointing in the z-direction can be looked upon as a point on a unit sphere. Thus we would like to split the unit sphere into concentric circular strips of equal surface area that are centered around the z-axis. Since the surface area of such a strip on a unit circle equals $2\Delta z$, fixing Δz leads to the bins of equal area, which translates into the equally spaced bins for cosine of the angle.

For convenience, we denote by $\alpha(u, v)$ the angle between two vectors u and v.

Alignment of vorticity and strain directions

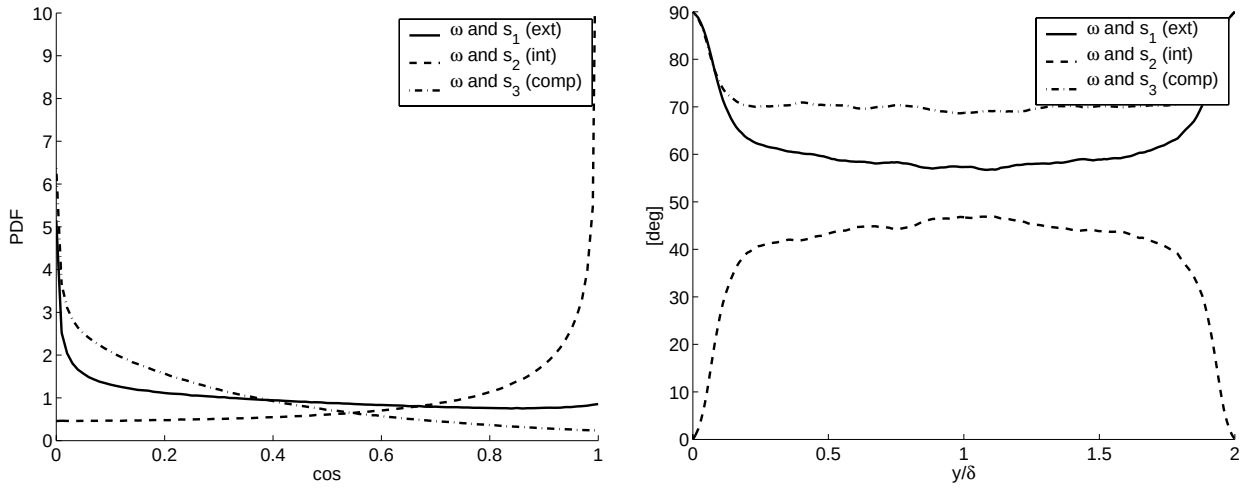

Figure 4–12: Alignment trends of the vorticity ω and the main strain directions as given by the DNS of channel flow: (a) PDF and (b) averaged along the homogeneous directions.

Figure 4–12 presents the PDF and transverse profile of the three angles between the vorticity ω and the principal strain directions, s_1, s_2 and s_3. The flow field is taken from a

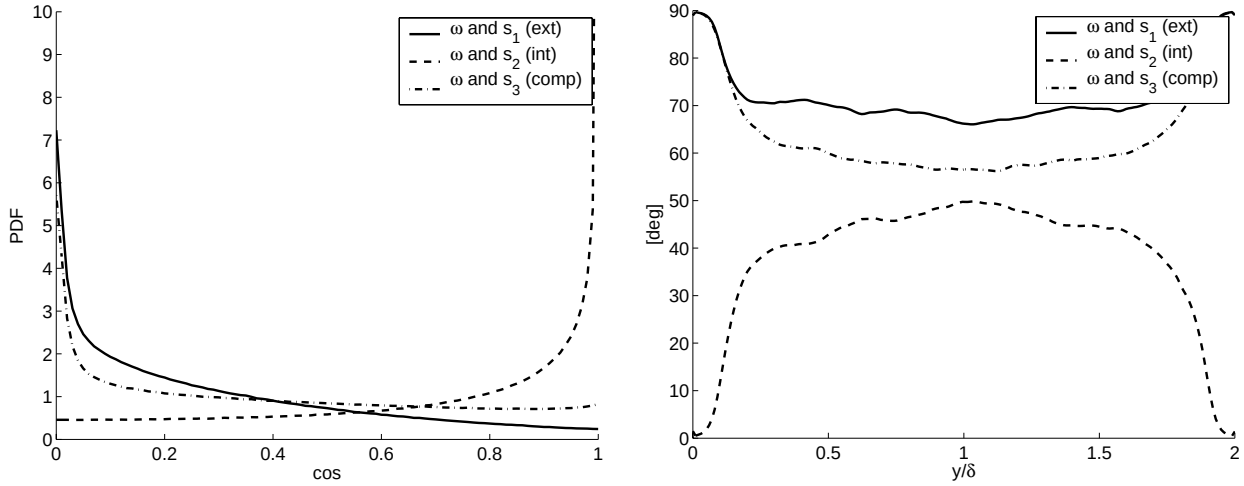

(a) (b)

Figure 4–13: Alignment trends of the resolved vorticity $\overline{\omega}$ and the resolved strain directions as given by the DNS of channel flow: (a) PDF and (b) averaged along the homogeneous directions. The filter used to average the DNS data is the linear filter, and the filter size is set to 7 DNS grid spacings in all direction.

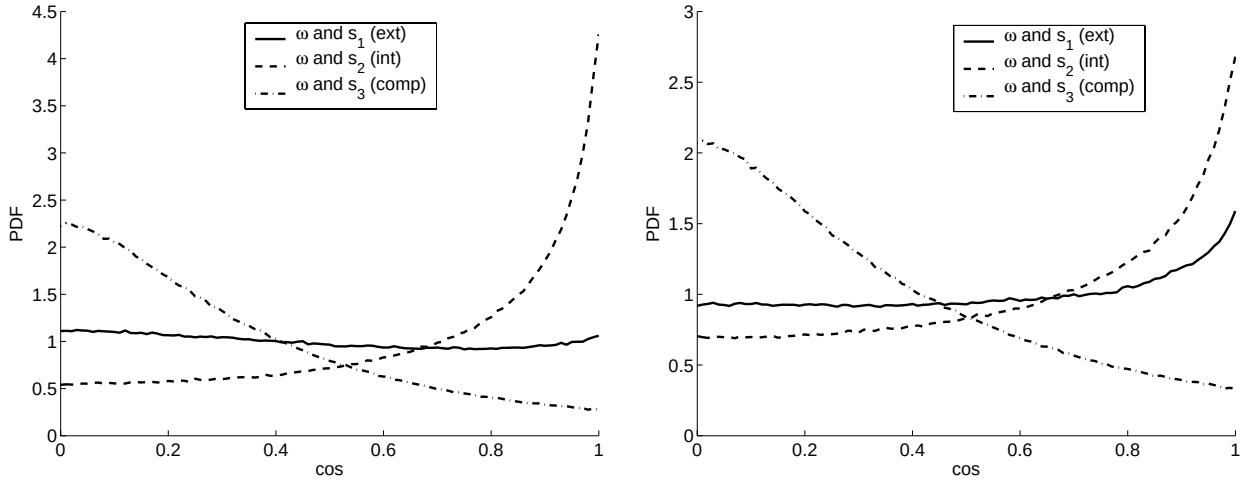

(a) (b)

Figure 4–14: Alignment vorticity and principal strain directions in the decaying isotropic turbulence at $\mathrm{Re}_\lambda = 70.34$: (a) DNS (b) spatially averaged DNS. Linear filter of size 7 DNS grid cells is used.

DNS of a channel flow. As it can be seen, the PDF clearly exhibits the tendency of ω to align with the intermediate strain direction, s_2. However, the transverse profile of the three angles (Figure 4–12b) does not fully support this alignment assumption. The average angle between ω and s_2 indeed tends to be smaller than the ones between ω and s_1 and ω and s_3, but not to the extent expected from the Figure 4–12a.

The spatially averaged, or resolved, quantities exhibit similar behavior. The resolved vorticity $\overline{\omega}$ was obtained from the spatially averaged velocity field. The filter size was chosen to be equal to 7 DNS grid spacings in all directions. The Figure 4–13 shows the alignment trends of the resolved vorticity and strain for the channel flow.

Similar alignment trends in the resolved flow field are present in Couette flow and mixing layer DNS (not shown), and decaying isotropic turbulence (Figure 4–14).

Alignment of scalar gradient, vorticity and strain directions

Our main interest in this section is to investigate the alignment trend of the raw and resolved scalar gradient with the principal strain directions. It is generally believed that in isotropic flows, the scalar gradient tends to align with the most compressive strain direction, s_3, while the presence of the mean shear changes the most probable angle between $\nabla\phi$ and s_3.[3,48] The former statement is illustrated by plotting the PDF of the alignment angle between $\nabla\phi$, strain directions and ω for the decaying isotropic turbulence in Figure 4–15.

Nomura and Elghobashi[48] state that if mean gradients of velocity and scalar dominate, the alignment peaks for both $\alpha(\nabla\phi, s_1)$ and $\alpha(\nabla\phi, s_3)$ are expected to occur at $\pi/4$, or, for the cosines of the angles, at about 0.71. In order to check this assumption we now look at channel flow and plot the PDFs of several angles sampled in different regions of the channel. The channel was split into 6 layers according to the wall proximity, ranging from the center of the channel ($|y-1| < 0.5$) to the near-wall region ($|y-1| > 0.9$, or $y^+ < 20$). The PDFs are given in the Figure 4–16.

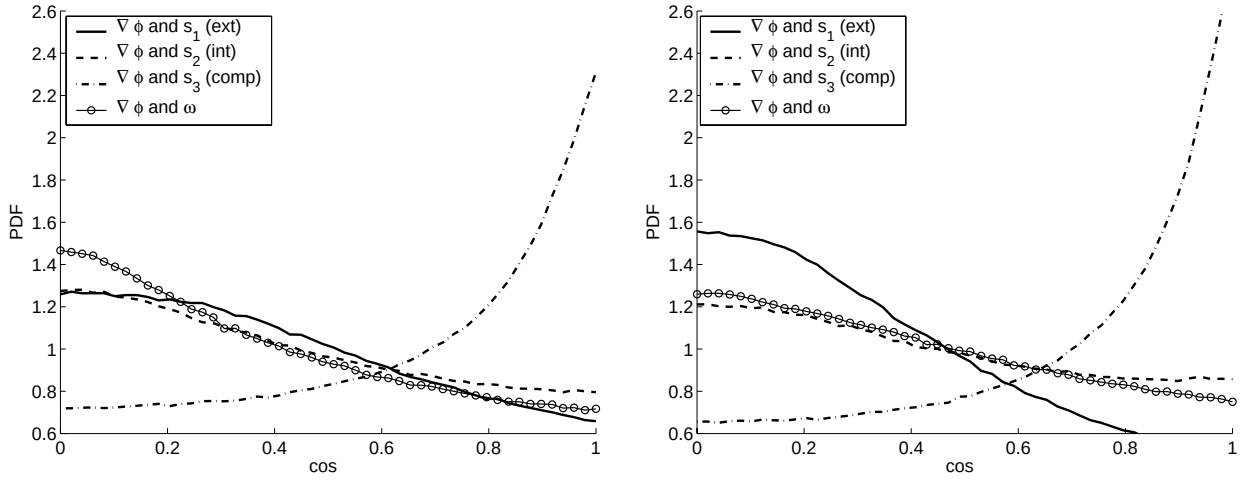

Figure 4–15: Alignment of the scalar gradient $\nabla\phi$ with principal strain directions and vorticity computed from the DNS of isotropic turbulence at $\mathrm{Re}_\lambda = 65.40$ (DIT-3): (a) DNS; (b) Filtered DNS. The filter width is set to 7 DNS grid cells.

It is evident from the Figure 4–16a that $\cos\alpha(\nabla\phi, s_1)$ and $\cos\alpha(\nabla\phi, s_3)$ indeed have peaks at 0.71, which indicates the presence of strong mean shear. Transverse profiles of $\alpha(\nabla\phi, s_j)$ and $\alpha(\nabla\phi, \omega)$ in the Figure 4–16b show that in the vicinity of the wall $\alpha(\nabla\phi, s_1)$ and $\alpha(\nabla\phi, s_3)$ are indeed close to $\pi/4$. Moreover, when averaged over the homogeneous directions (x and z), $\alpha(\nabla\phi, s_3)$ appears to be very close to $\pi/4$ throughout the channel. The secondary peak at 1 in the PDF of $\cos\alpha(\nabla\phi, s_3)$ in the Figure 4–16a can be attributed to the fact that far from the wall, the flow is close to isotropic and thus the behaviour demonstrated for the DIT case is expected (see Figure 4–15a).

Figures 4–16c through 4–16f show the alignment trends of $\nabla\phi$ with strain directions and vorticity. Each figure depicts 6 PDFs, taken in the indicated regions. It is evident that far from the wall the alignment trends of $\nabla\phi$ are not very different from ones in the isotropic flow (Figure 4–15). But in the vicinity of the wall the alignment trends shift to those predicted by Nomura and Elghobashi,[48] that is, the scalar gradient lies in the plane orthogonal to s_2 and has a $\pi/4$ angle with s_1 and s_3. The orthogonality of $\nabla\phi$ and ω, similarly to the orthogonality of $\nabla\phi$ and s_2, seems not to be affected by the presence of mean shear or the

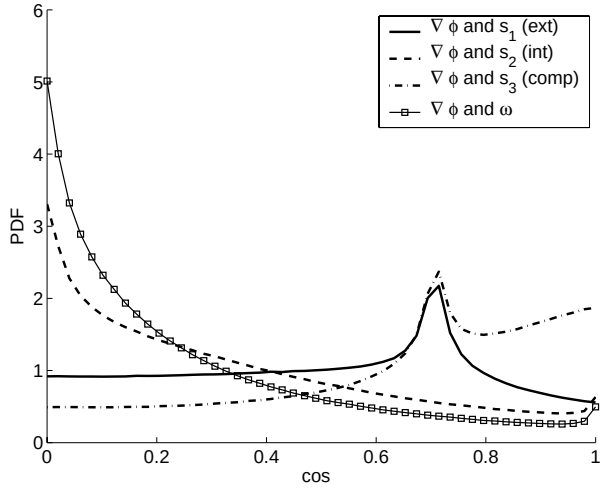

(a) $\alpha(\nabla\phi, s_j)$ and $\alpha(\nabla\phi, \omega)$

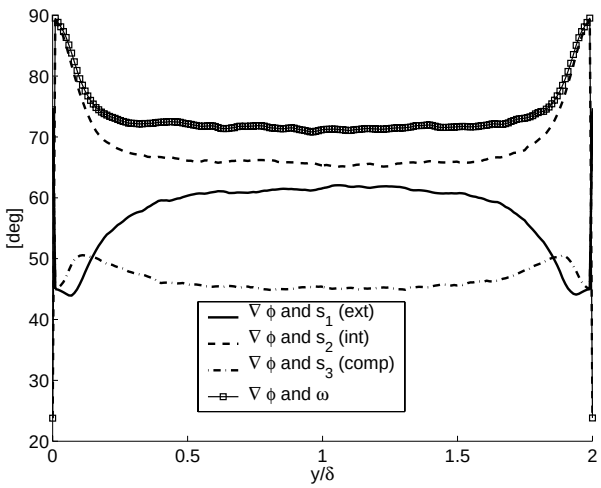

(b) y-profile of $\alpha(\nabla\phi, s_j)$ and $\alpha(\nabla\phi, \omega)$

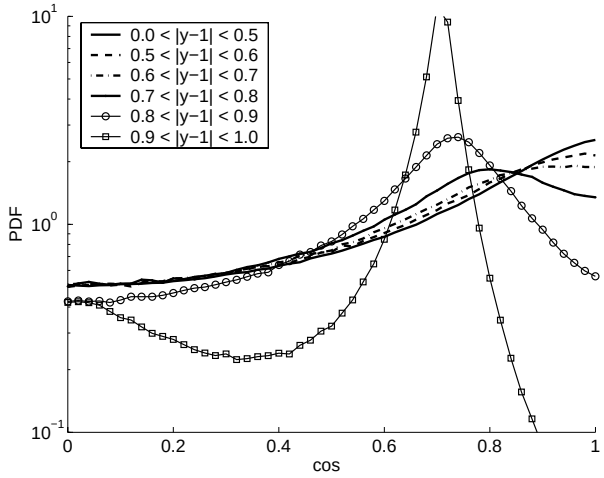

(c) $\alpha(\nabla\phi, s_1)$

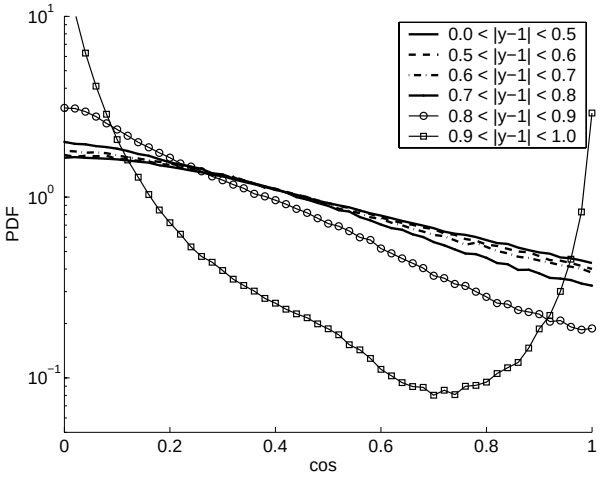

(d) $\alpha(\nabla\phi, s_2)$

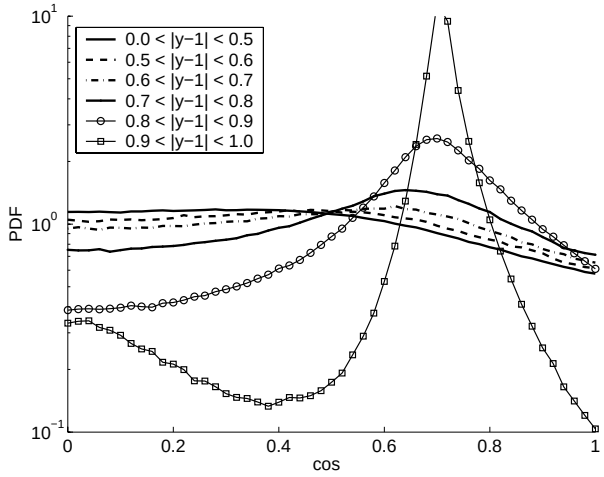

(e) $\alpha(\nabla\phi, s_3)$

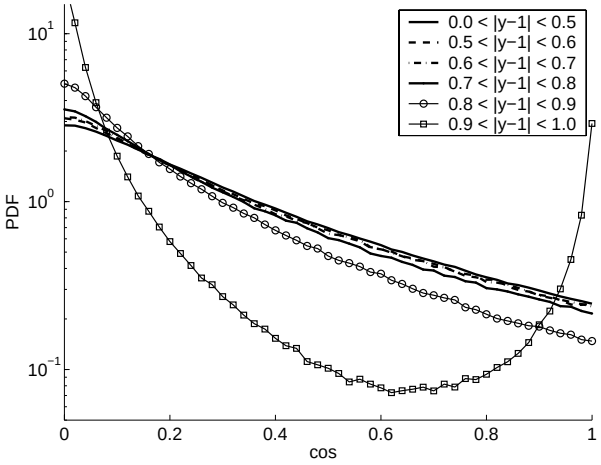

(f) $\alpha(\nabla\phi, \omega)$

Figure 4–16: Alignment trends of the scalar gradient $\nabla\phi$ in the DNS of the channel flow, and its dependence on the proximity of the wall.

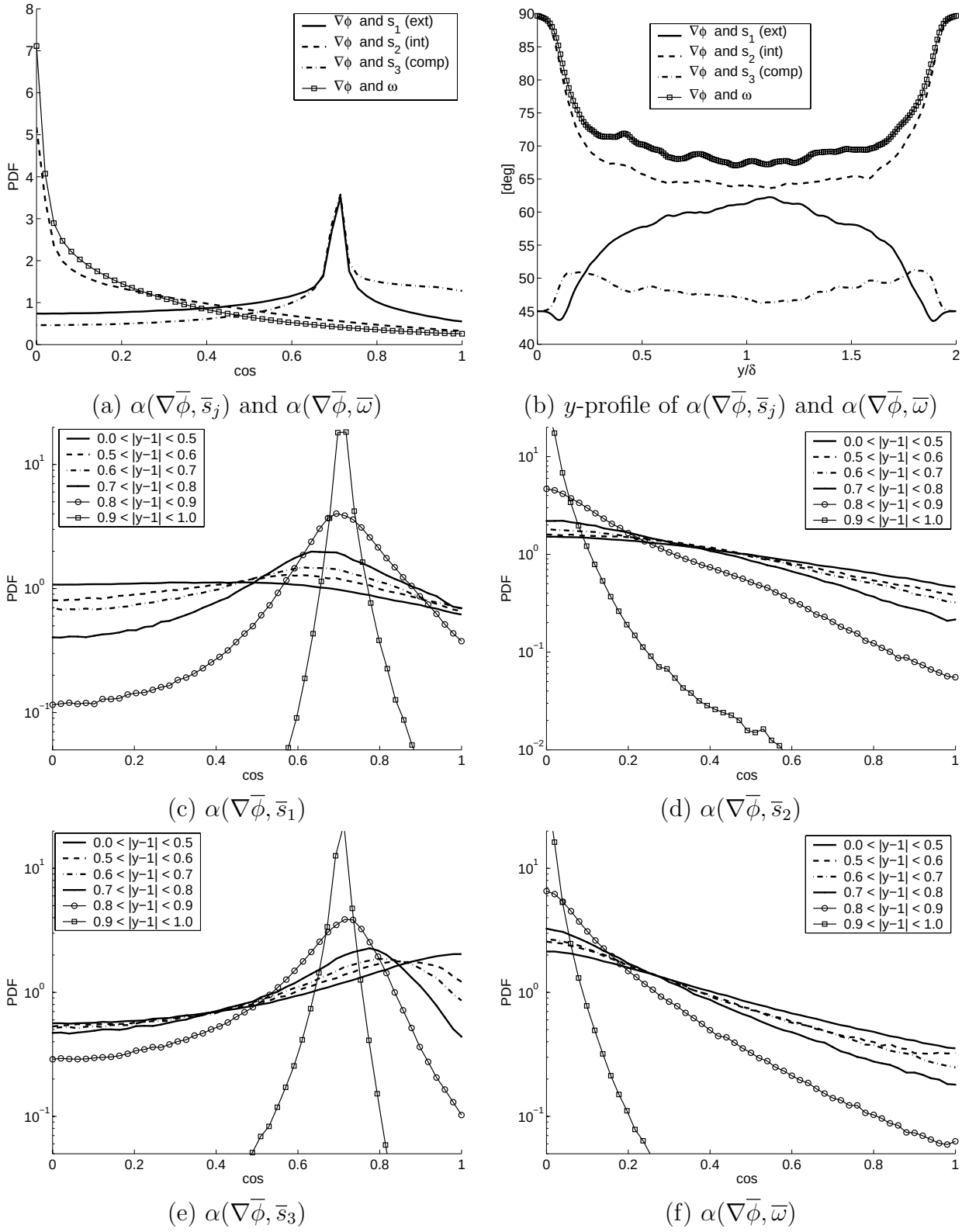

(a) $\alpha(\nabla\overline{\phi}, \overline{s}_j)$ and $\alpha(\nabla\overline{\phi}, \overline{\omega})$

(b) y-profile of $\alpha(\nabla\overline{\phi}, \overline{s}_j)$ and $\alpha(\nabla\overline{\phi}, \overline{\omega})$

(c) $\alpha(\nabla\overline{\phi}, \overline{s}_1)$

(d) $\alpha(\nabla\overline{\phi}, \overline{s}_2)$

(e) $\alpha(\nabla\overline{\phi}, \overline{s}_3)$

(f) $\alpha(\nabla\overline{\phi}, \overline{\omega})$

Figure 4–17: Alignment trends of the resolved temperature gradient $\nabla\overline{\phi}$ in the channel flow, and its dependence on the proximity of the wall. The base filter size is set to 7 DNS grid spacings.

wall proximity, which is shown in the Figures 4–16d and 4–16f, correspondingly.

A phenomena of special interest is the secondary peak at $\cos\alpha = 1$ in the PDFs in Figures 4–16d and 4–16f. This, much weaker, peak is explained by the fact that near-wall turbulence is dominated by "hairpins" and "streaks", which are produced by the streamwise vortical structures. Inside the "streaks", the vorticity vector is pointing in the streamwise direction. This is orthogonal to the scalar gradient, which is in this case, orthogonal to the wall. It is worth noting overall that $\nabla\phi$ and ω have a more pronounced orthogonal alignment than $\nabla\phi$ and s_2. Similar alignment trends occur in the Couette flow (not shown).

Figure 4–17 shows PDFs and profiles of similar angles as Figure 4–16, but computed for the spatially averaged field. First, and the most striking, difference is that the resolved temperature gradient does not show the preferential alignment with the most compressive resolved strain direction, as seen on the Figure 4–17a. Since spatial filtering does not seem to affect this particular alignment for the DIT case (Figure 4–15), we conclude that application of the spatial filter of this particular size eliminates the small eddies leaving only large-scale structures, and thus the flow near the centerline cannot be regarded as isotropic at these filter scales, being subject to pronounced mean gradients in both scalar and velocity fields. The other alignment trends remain similar to those of an unfiltered DNS data shown in the Figure 4–16.

4.5.3 Log-normality of scalars in the turbulent flow

The last observation from the section 4.5.1 is consistent with the model proposed in 1967 by Gurvich and Yaglom[31] as an extension of Kolmogorov's third hypothesis. The model predicts that if

- a non-negative scalar variable ϕ is defined only by the small-scale turbulent fluctuations,

- V_r is some region with characteristic length r,
- $\eta \ll r \ll L$, where η is Kolmogorov length scale and L is the flow geometry length scale,
- ϕ_r denotes the average value of ϕ in the region V_r,

then the variable ϕ_r has a log-normal distribution.

In the literature one can find DNS results and experimental measurements that suggest that the scalar dissipation $\chi = \nabla\phi \cdot \nabla\phi$ has an "almost" log-normal distribution with considerable negative skewness, or, equivalently, the variable $\ln \chi$ has an almost normal PDF with negative skewness (Su and Clemens,[68] Feikema et al.,[28] Eswaran and Pope[27]). This, contradictory to Su and Clemens,[68] does not disprove the original hypothesis of Gurvich and Yaglom[31] that states that in order to be log-normally distributed, the flow variable has to be averaged over the volumes with characteristic dimensions much larger than Kolmogorov length scale η.

Figure 4–18a shows the unconditioned PDF for $\ln \overline{\chi}$ for the snapshot DIT-3. It is clear that the shape of the PDF is far from log-normal. However, if we restrict our sampling to the areas where ϕ is developed ($0.2 < \phi < 0.8$), we obtain the PDF shown in the Figure 4–18b, which is very close to a normal distribution. This shows that for the developed scalar field the distribution of $\overline{\chi}$ is indeed log-normal.

The statistical analysis showed similar situation for $\mathrm{Re}_\lambda > 40$. For lower Reynolds numbers, PDF of $\overline{\chi}$ resembles log-normal distribution closely without conditioning.

The energy dissipation, however, exhibited the log-normal-like behaviour for all data sets, and no conditioning is needed. Two PDFs are shown in the Figure 4–19, for the data sets DIT-3 and DIT-8. This confirms the prediction made by Gurvich and Yaglom,[31] since $\overline{\epsilon}$ is defined by the small flow structures for all samples and therefore does not need conditioning, whereas $\overline{\chi}$ is not defined by the fine structures in the early snapshots.

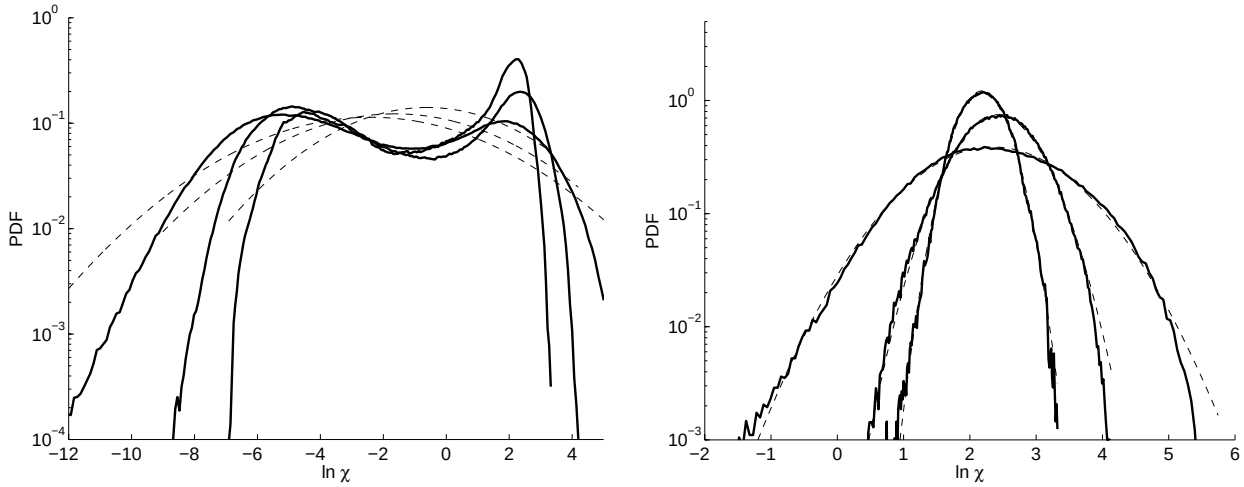

(a) (b)

Figure 4–18: PDF for $\ln \overline{\chi}$ for $\mathrm{Re}_\lambda = 65.40$ (DIT-3): (a) unconditioned PDF; (b) conditioned by $0.2 < \phi < 0.8$. Bold lines from the outer to the inner correspond to the PDFs of $\ln \overline{\chi}$ for the filter size 0, 5 and 15 grid cells, correspondingly. The dashed line present the normal PDFs with same first two moments.

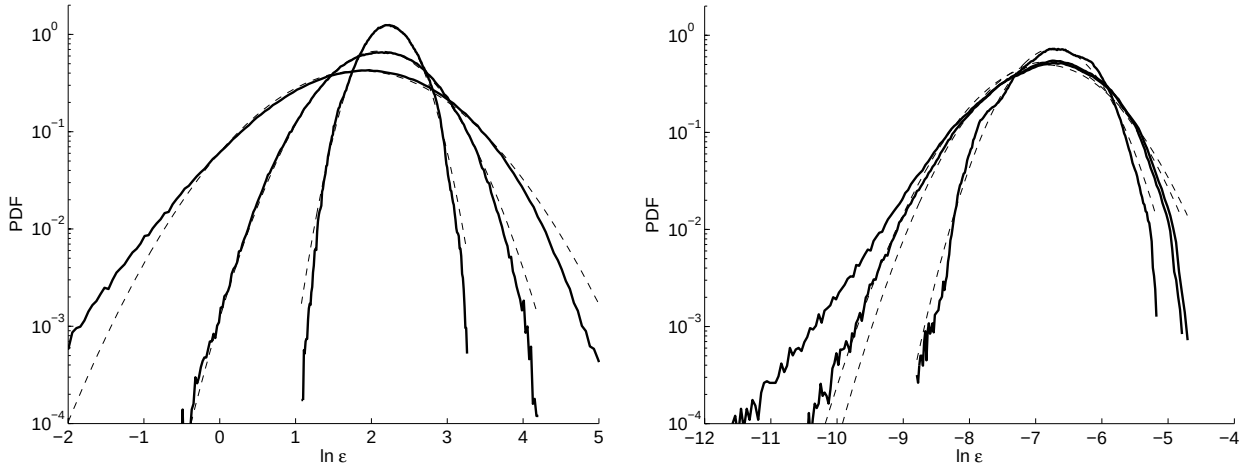

(a) $\mathrm{Re}_\lambda = 65.40$ (b) $\mathrm{Re}_\lambda = 10.01$

Figure 4–19: PDF for $\ln \overline{\epsilon}$ for different Reynolds numbers. Bold lines from the outer to the inner correspond to the PDFs of $\ln \overline{\epsilon}$ for the filter size 0, 5 and 15 grid cells, correspondingly. The dashed line present the normal PDFs with same first two moments.

4.5.4 Conclusions

For the fully resolved flow field, our observations in general match those from the current literature.

The vorticity vector ω tends to align with the intermediate strain direction s_2 — regardless of the flow being considered and the flow developmental stage (for the DIT case).

The behaviour of the scalar gradient $\nabla\phi$ appears to depend on the presence of the mean gradient imposed on the fine flow structures. When the mean strain is small comparing to the local strain (as it happens in the DIT case) the scalar gradient tends to align with the most compressive strain direction given by the eigenvector s_3 of the rate-of-strain tensor S_{ij}. In the presence of mean shear that dominates the flow (as it happens in the channel and Couette flows) the scalar gradient tends to remain orthogonal to the intermediate strain direction s_2 and form a $\pi/4$-angle with the most extensive (s_1) and most compressive (s_3) strain directions. This is fully consistent with observations of Nomura and Elghobashi[48] for the homogeneous shear flow.

Also, we checked the log-normality assumption put forth by Gurvich and Yaglom[31] for the energy dissipation ϵ and the scalar dissipation χ. Once the corresponding flow field is developed enough, both variables exhibit the log-normal distribution if averaged over a cube of length r, where $\eta \ll r \ll L$.

Chapter 5. SGS Scalar Flux Model

5.1 Modeling SGS scalar flux as a vector

5.1.1 Alignment trends from *a priori* tests

Modeling the SGS scalar flux $\tau_{i\phi}$ differs from modeling the SGS Reynolds stress τ_{ij} because $\tau_{i\phi}$ is a vector and thus does not have to comply with the realizability conditions outlined in section 3.2. In order to evaluate a certain model *a priori*, one can compare the values of $\tau_{i\phi}$ obtained from fully resolved DNS and ones obtained by the model component-wise, and compute PDFs of relative errors for three directions. Alternatively, we can treat modeling $\tau_{i\phi}$ as modeling a vector, and, instead of components, compare magnitudes and directions of the true $\tau_{i\phi}$ to ones predicted by a model.

In our opinion, it might be beneficial to apply the tools from statistical geometry to SGS modeling. In particular, we think it is feasible to look at the alignment between $\tau_{i\phi}$ and various resolved quantities, e.g., vorticity $\overline{\omega}$, resolved scalar gradient $\nabla\overline{\phi}$, principal strain directions etc. Since the DNS database contains wall-bounded flows and free-shear flows, we might be able to investigate the effect of wall proximity on those alignment trends.

Figure 5–1 shows the alignment trends of $\tau_{i\phi}$ with various vector quantities: strain directions, Leonard vector $L_{i\phi}$, resolved scalar gradient $\nabla\overline{\phi}$, and the Clark Model. Several trends can be observed.

First, it should be noted that, similarly to the resolved gradient $\nabla\overline{\phi}$, the SGS scalar flux $\tau_{i\phi}$ tends to be consistently orthogonal to the resolved vorticity for both Decaying Isotropic Turbulence (DIT) and channel flow. However, the vectors $\tau_{i\phi}$ and $\nabla\overline{\phi}$ themselves appear far from being aligned. In fact, for the DIT case the alignment between $\tau_{i\phi}$ and $\nabla\overline{\phi}$ seems to

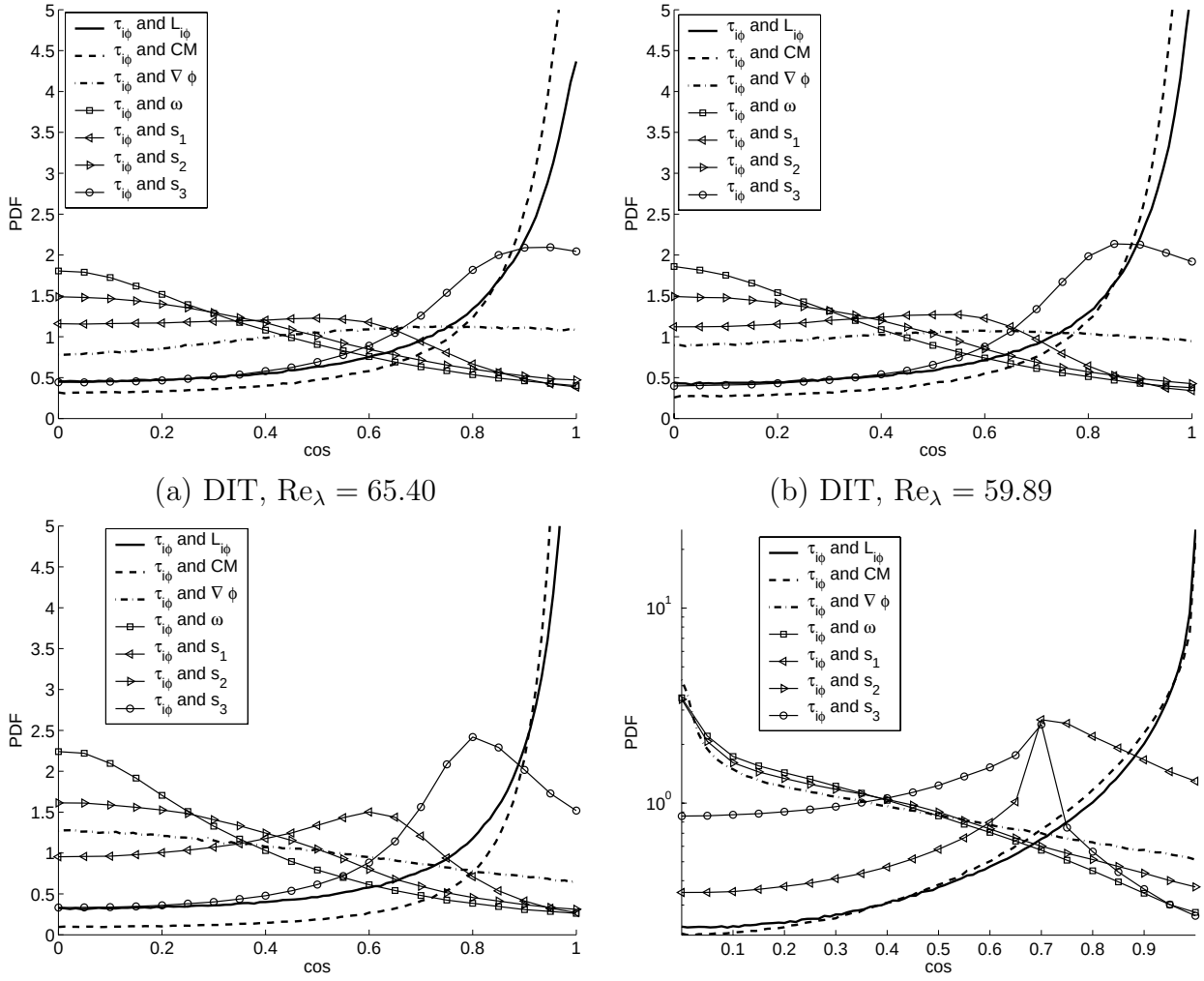

(a) DIT, $\mathrm{Re}_\lambda = 65.40$

(b) DIT, $\mathrm{Re}_\lambda = 59.89$

(c) DIT, $\mathrm{Re}_\lambda = 25.00$

(d) Channel flow

Figure 5–1: Cosine of angle between $\tau_{i\phi}$ and various vectors. The data obtained by spatially averaging DNS data for decaying isotropic turbulence and channel flow. The base filter size is 7 DNS grid cells. The test filter size is 14 DNS grid cells, or two LES grid cells.

be close to random. For the channel flow which possesses strong mean scalar and velocity gradients, $\tau_{i\phi}$ tends to be orthogonal to $\nabla\overline{\phi}$, which is illustrated in the Figure 5–1d.

In the literature, an effort has been made to investigate the alignment of $\tau_{i\phi}$ experimentally by Higgins et al.[10] They performed the measurements of the velocity and temperature ϕ in the lower atmospheric boundary layer and found that the vector $\tau_{i\phi}$ had a tendency not to align or be orthogonal to $\nabla\overline{\phi}$. Instead, $\tau_{i\phi}$ tends to be co-planar with the vectors given by the eddy viscosity and Clark models, that is, with vectors $\nabla\overline{\phi}$ and $\Delta^2\frac{\partial\overline{u}_i}{\partial x_k}\frac{\partial\overline{\phi}}{\partial x_k}$. This supported their argument about the applicability of the mixed model

$$\tau_{i\phi} \approx C\Delta^2\left[-|\overline{S}|\frac{\partial\overline{\phi}}{\partial x_i} + \lambda\frac{\partial\overline{u}_i}{\partial x_k}\frac{\partial\overline{\phi}}{\partial x_k}\right]. \tag{5.1}$$

The alignment between SGS scalar flux and the resolved strain directions is also of great interest. The SGS scalar flux seems to be consistently orthogonal to the intermediate strain direction, s_2. The alignment trends between $\tau_{i\phi}$ and the other strain directions appear to depend on some external factors.

From the Figure 5–1, it appears that for higher Reynolds numbers and in the absence of the mean scalar gradient, $\tau_{i\phi}$ tends to align with s_3, the most compressive strain direction (Figure 5–1a). Later in time (Figure 5–1b,c), when the Reynolds number decreases, the most probable value of the angle $\alpha(\tau_{i\phi}, s_3)$ shows considerable departure from zero. In fact, it appears that angles $\alpha(\tau_{i\phi}, s_1)$ and $\alpha(\tau_{i\phi}, s_3)$ approach $\pi/4$ while $\alpha(\tau_{i\phi}, s_2)$ remains close to $\pi/2$. For the channel flow case, the PDFs of the alignment angles $\alpha(\tau_{i\phi}, s_1)$ and $\alpha(\tau_{i\phi}, s_3)$ have a clear maxima at $\pi/4$ (Figures 5–1d and 5–3a).

One might speculate that the change in the PDF of $\alpha(\tau_{i\phi}, s_3)$ is affected not by the Reynolds number but rather by the "maturity" of the scalar field. In order to check this we computed the PDFs of the same angles but for a different DIT simulation with considerably higher Reynolds number, which is referred to as "Run 2". The results are presented in the Figure 5–2.

The Run 2 has the same characteristics including the code and resolution, the only difference being the higher initial Reynolds number. The quiescent flow field was forced to $\mathrm{Re}_\lambda = 165.92$, was allowed to relax to $\mathrm{Re}_\lambda = 94$ and then the passive scalar was introduced to the flow in the manner similar to one from the Section 4.2.3. During the Run 2, the scalar field had a longer time develop the small-scale structures. Despite that fact, the PDFs demonstrated in the Figures 5–1b and 5–2b look very similar (both have $\mathrm{Re}_\lambda \approx 60$). Even more surprising is the resemblance between PDFs shown in Figures 5–1c and 5–2c, despite the fact that the Reynolds numbers are quite different. This leads us to the conclusion that the orientation of $\tau_{i\phi}$ is affected by both the flow structures and the development stage of the scalar field.

Figures 5–3 and 5–4 show the dependence of the alignment of $\tau_{i\phi}$ with various vectors on the wall proximity in the channel flow. The main observation is that $\tau_{i\phi}$ tends to stay orthogonal to $\overline{s}_2$ and $\overline{\omega}$, that is, to remain in the plane spanned by $\overline{s}_1$ and $\overline{s}_3$. The most probable values for both angles $\alpha(\tau_{i\phi}, \overline{s}_1)$ and $\alpha(\tau_{i\phi}, \overline{s}_3)$ are observed to be $\pi/4$.

Based on the Figures 5–1 and 5–2, we can conclude that the best prediction for the SGS flux direction is given by Clark model. The self-similarity models, and Dynamic Structure models mentioned later in this document, take the direction from the Leonard vector $L_{i\phi}$ and, based on figures, predict the direction of SGS flux as well as the Clark model. It should be noted, however, that the direction of $L_{i\phi}$ should (and would) change as the test filter is varied, but based on our investigations (not shown), the alignment of $\tau_{i\phi}$ and $L_{i\phi}$ remains very satisfactory even for quite large test filter sizes.

5.1.2 Magnitude

We also wanted to investigate possible correlations between the magnitudes of the vector $\tau_{i\phi}$ and other quantities. The following quantities have been tested:

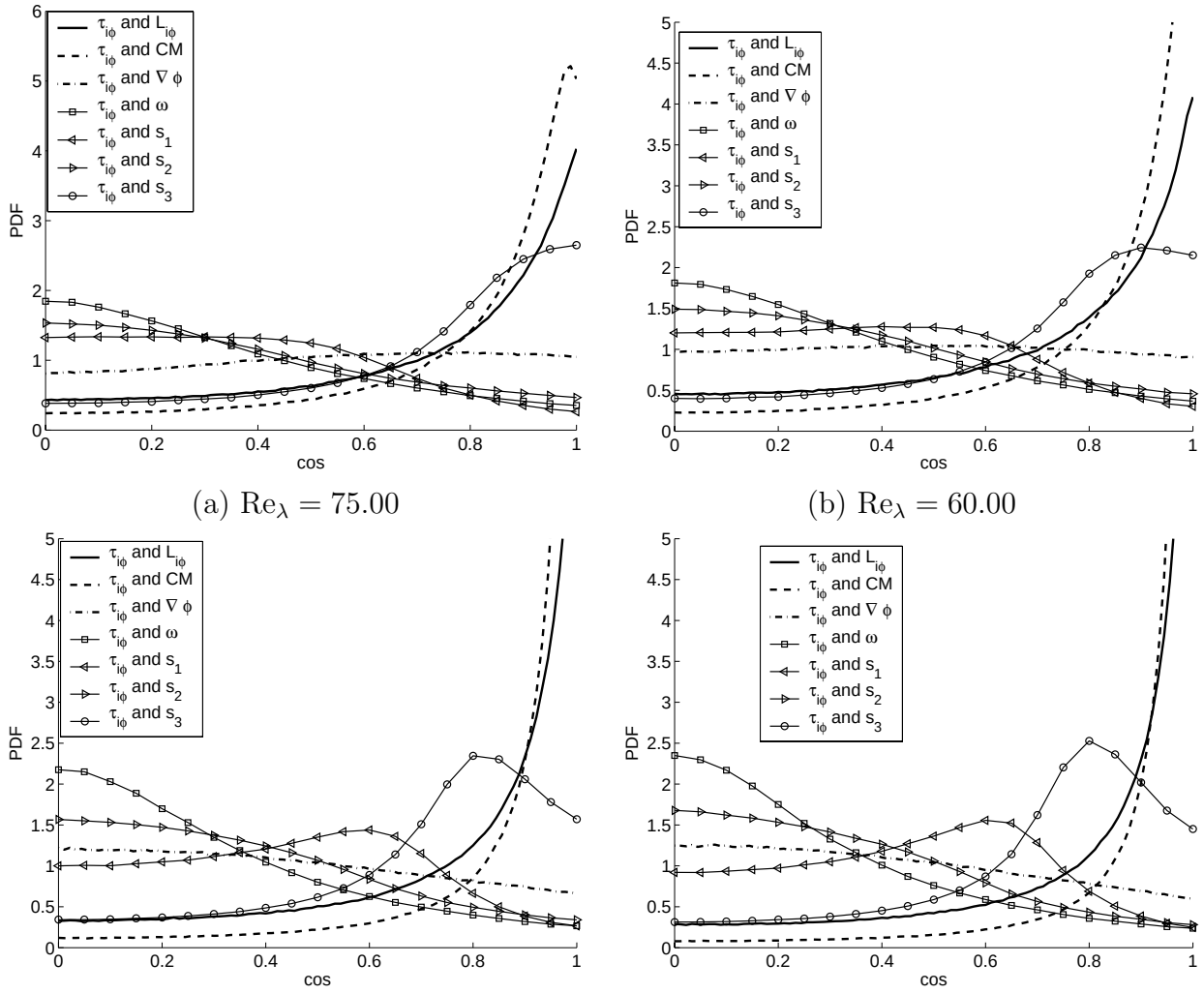

(a) $\mathrm{Re}_\lambda = 75.00$

(b) $\mathrm{Re}_\lambda = 60.00$

(c) $\mathrm{Re}_\lambda = 50.00$

(d) $\mathrm{Re}_\lambda = 46.00$

Figure 5–2: Cosine of angle between $\tau_{i\phi}$ and various vectors: Data from the DIT simulation, Run 2. The base filter size is 7 DNS grid spacings. The test filter size is 14 DNS grid spacings, or two LES grid spacings.

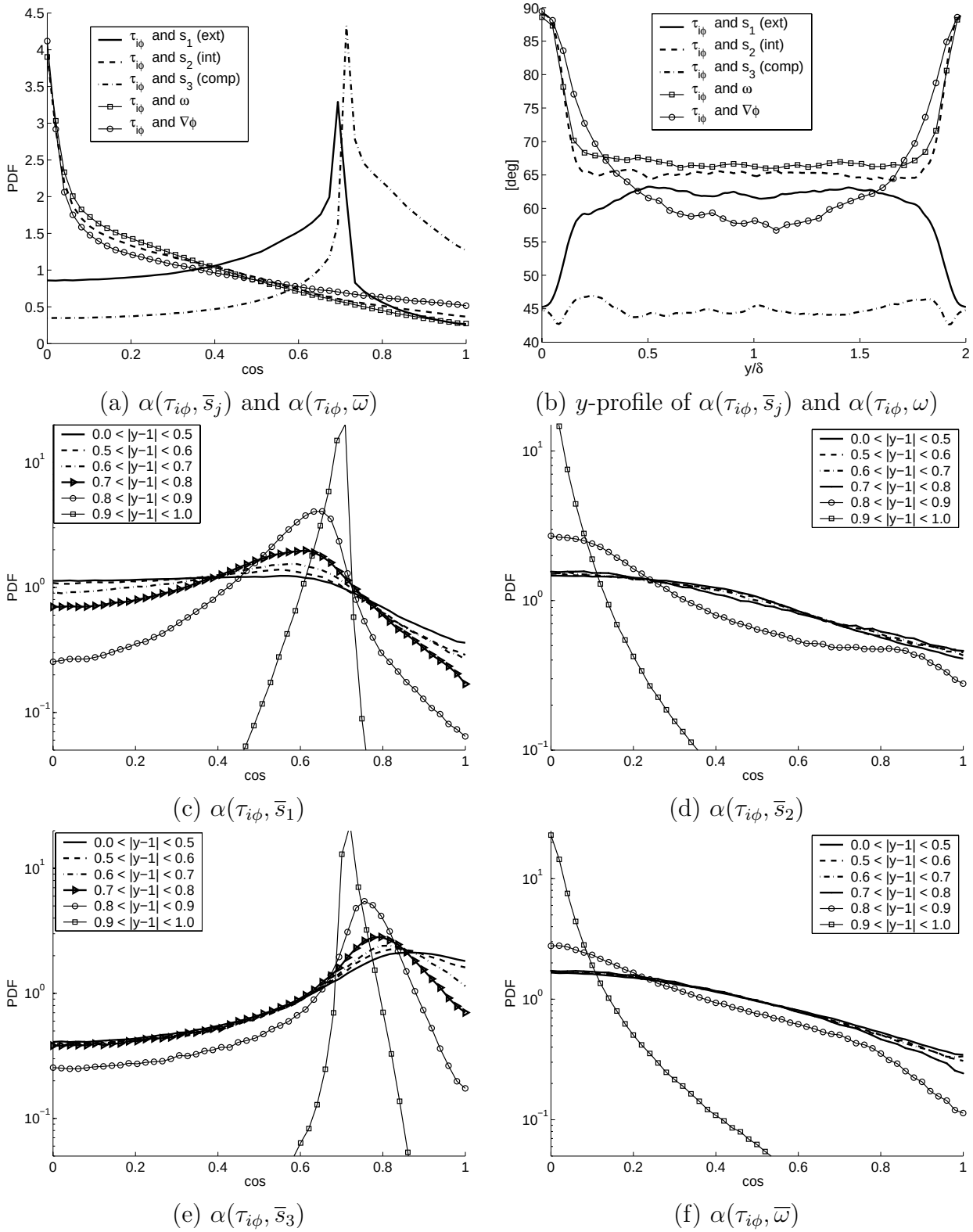

(a) $\alpha(\tau_{i\phi}, \overline{s}_j)$ and $\alpha(\tau_{i\phi}, \overline{\omega})$

(b) y-profile of $\alpha(\tau_{i\phi}, \overline{s}_j)$ and $\alpha(\tau_{i\phi}, \omega)$

(c) $\alpha(\tau_{i\phi}, \overline{s}_1)$

(d) $\alpha(\tau_{i\phi}, \overline{s}_2)$

(e) $\alpha(\tau_{i\phi}, \overline{s}_3)$

(f) $\alpha(\tau_{i\phi}, \overline{\omega})$

Figure 5–3: Alignment trends of the SGS scalar flux $\tau_{i\phi}$ in the channel flow, and its dependence on the proximity of the wall.

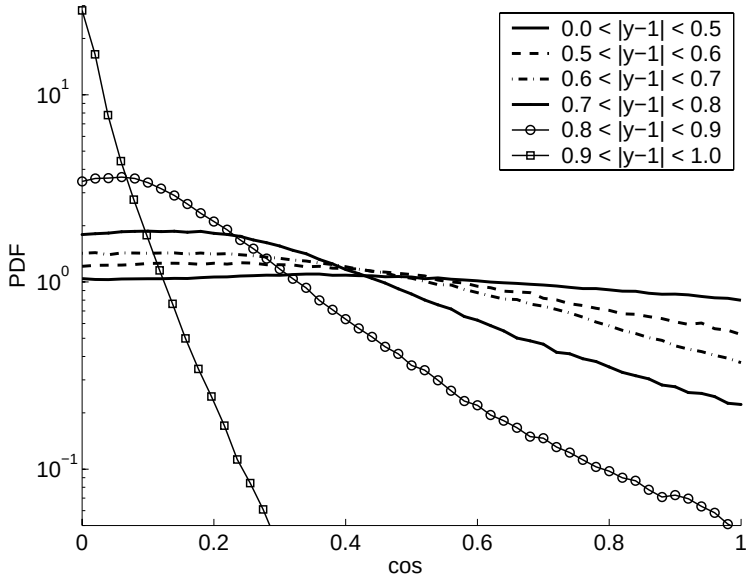

Figure 5–4: $\alpha(\tau_{i\phi}, \nabla\overline{\phi})$ in the channel flow: dependence on the proximity to the wall.

- Magnitude of the resolved strain tensor $|\overline{S}| = \sqrt{2\overline{S}_{ij}\overline{S}_{ij}}$;
- Energy dissipation $\epsilon = \nu\overline{\frac{\partial u_i}{\partial x_j}\frac{\partial u_i}{\partial x_j}}$
- SGS energy dissipation $\epsilon_{sgs} = \epsilon - \nu\frac{\partial\overline{u}_i}{\partial x_j}\frac{\partial\overline{u}_i}{\partial x_j}$;
- Scalar dissipation $\overline{\chi} = 2D\overline{\frac{\partial\phi}{\partial x_i}\frac{\partial\phi}{\partial x_i}}$;
- SGS scalar dissipation $\chi_{sgs} = \overline{\chi} - 2D\frac{\partial\overline{\phi}}{\partial x_i}\frac{\partial\overline{\phi}}{\partial x_i}$;
- Resolved scalar gradient $|\nabla\overline{\phi}|$;

To test the dependency of $|\tau_{i\phi}|$ on another quantity, we have sorted the values of the variable in question into six bins conditioned on the magnitude of $|\tau_{i\phi}|$. We then determine the mean variable value in each bin.

The quantities that showed significant correlation with the magnitude of $\tau_{i\phi}$ were the magnitude of the resolved scalar gradient $|\nabla\overline{\phi}|$ and the scalar dissipation $\overline{\chi}$. The resulting graphs are shown in the Figures 5–5 and 5–6.

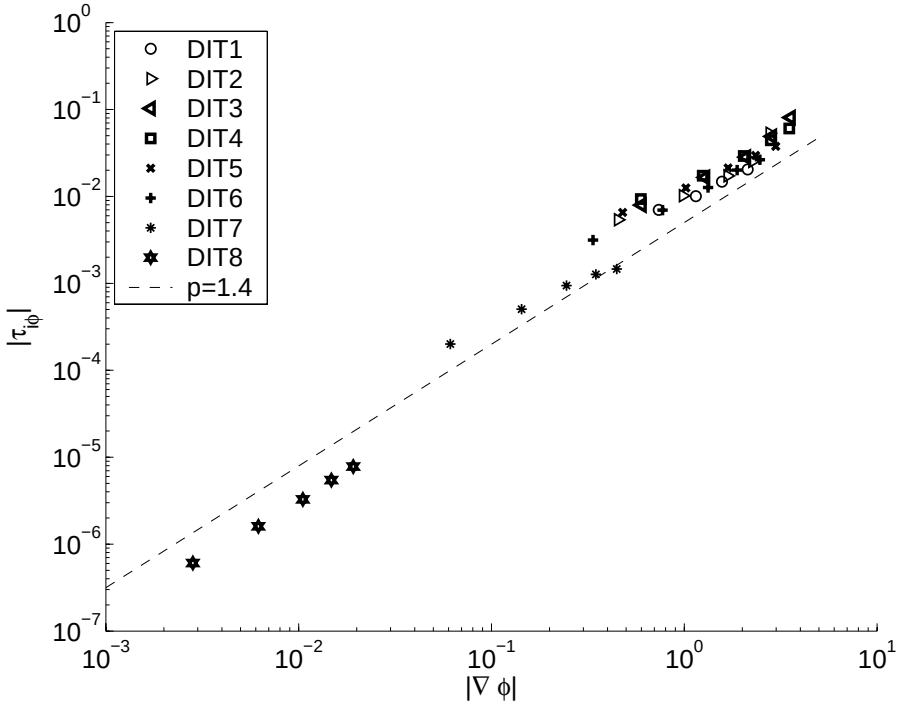

Figure 5–5: Scatter plot of $|\nabla\overline{\phi}|$ vs. $|\tau_{i\phi}|$. Different symbols correspond to different snapshots (see Table 2 for reference). The power law $|\tau_{i\phi}| = |\nabla\overline{\phi}|^{1.4}$ is plotted for comparison.

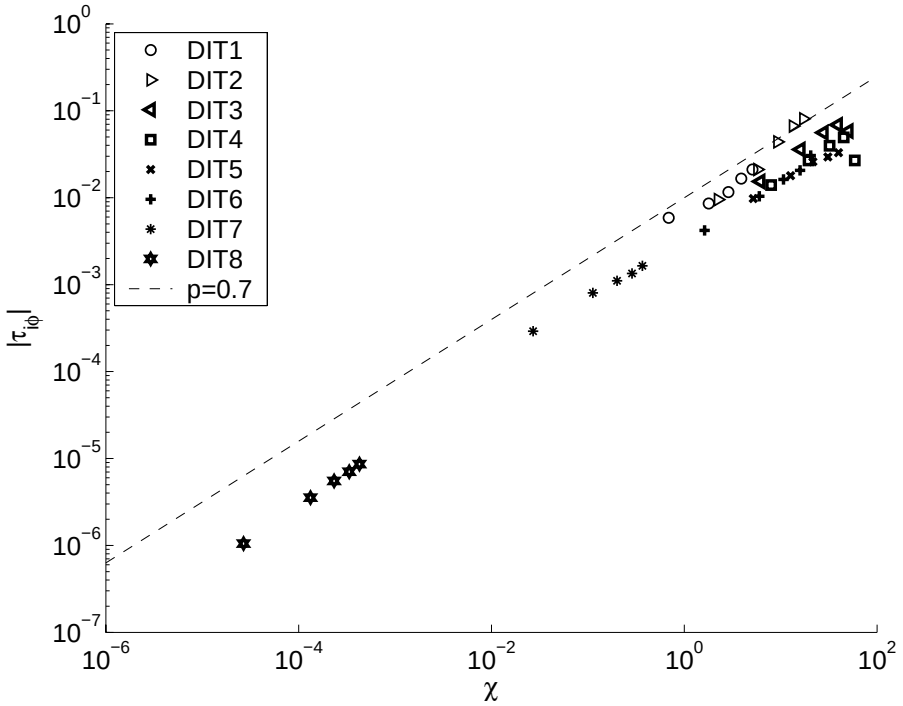

Figure 5–6: Scatter plot of χ vs. $|\tau_{i\phi}|$. Different symbols correspond to different snapshots (see Table 2 for reference). The power law $|\tau_{i\phi}| = \chi^{0.7}$ is plotted for comparison.

5.1.3 Conclusions

The direction of the SGS scalar flux $\tau_{i\phi}$ appears to depend either on the Reynolds number or on the maturity of the scalar field.

For the DIT case, we observe the peak of $\alpha(\tau_{i\phi}, \overline{s}_3)$ initially at $\pi/2$ and, as the flow develops, the alignment peak shifts to $\pi/4$. The initial distribution of $\alpha(\tau_{i\phi}, \overline{s}_1)$ does not have a clearly defined peak but tends closer to zero. As the flow develops, a peak appears, and it migrates towards $\pi/4$. The distribution of angle $\alpha(\tau_{i\phi}, \overline{s}_2)$ has a clearly defined peak at $\pi/2$ throughout the DIT simulation. This is very similar to the evolution of alignment trends for the scalar gradient $\nabla\phi$ for the case of the homogeneous shear flow described by Nomura and Elghobashi.[48] They argue that for $\nabla\phi$ the change in the alignment reflects the growing importance of the mean strain, since initially the local gradients are dominating. We suspect that the described phenomena might occur also due to the development of the scalar field itself.

The magnitide of the vector $\tau_{i\phi}$ seems to correlate with the magnitude of the resolved gradient and the value of scalar dissipation.

If we consider the data from the DNS of channel flow, in which the mean strain is comparable to the local strain, then we observe clear alignment peaks of $\alpha(\tau_{i\phi}, \overline{s}_1)$ and $\alpha(\tau_{i\phi}, \overline{s}_3)$ at $\pi/4$ and a peak of $\alpha(\tau_{i\phi}, \overline{s}_2)$ at $\pi/2$. Quite similar alignment trends are observed for the $\nabla\overline{\phi}$. Yet $\nabla\overline{\phi}$ and $\tau_{i\phi}$ tend to be orthogonal.

5.2 Model Formulation

The term we need to model is

$$\tau_{i\phi} = \overline{u_i\phi} - \overline{u}_i\overline{\phi}. \tag{5.2}$$

A Dynamic Structure (DS) type model for $\tau_{i\phi}$ is the following:

$$\tau_{i\phi} \approx \frac{\overline{\phi\phi} - \overline{\phi}\,\overline{\phi}}{\widehat{\overline{\phi}\,\overline{\phi}} - \widehat{\overline{\phi}}\,\widehat{\overline{\phi}}} \left[\widehat{\overline{u}_i\overline{\phi}} - \widehat{\overline{u}}_i\widehat{\overline{\phi}}\right] \equiv \frac{\theta}{\Theta} L_{i\phi}, \tag{5.3}$$

where θ is the SGS variance of the scalar ϕ, Θ is the SGS variance of $\overline{\phi}$ on the test level, and $L_{i\phi}$ is the Leonard term for $\tau_{i\phi}$.

We can derive this model in two ways. The first way employs an intuitive argument: we build a similarity-type model with a particular coefficient. We start with the Leonard term and scale it down to the base level using the ratio of SGS variances on two levels. The second way is more formal and employs the Dynamic Procedure.

First, we postulate that

$$\overline{u_i\phi} - \overline{u}_i\overline{\phi} = C_b(\overline{\phi\phi} - \overline{\phi}\,\overline{\phi}), \tag{5.4}$$

$$\widehat{\overline{u_i\phi}} - \widehat{\overline{u}}_i\widehat{\overline{\phi}} = C_t(\widehat{\overline{\phi\phi}} - \widehat{\overline{\phi}}\,\widehat{\overline{\phi}}), \tag{5.5}$$

where C_b and C_t are functions of space. Then using the argument similar to Germano et.al,[29] we can combine (5.4) and (5.5) to obtain

$$L_{i\phi} = C_t(\widehat{\overline{\phi\phi}} - \widehat{\overline{\phi}}\,\widehat{\overline{\phi}}) - \widehat{C_b\theta}.$$

Now assuming that $C_t \approx C_b \approx C$ and C varies slowly in space, we get

$$C = \frac{L_{i\phi}}{\widehat{\overline{\phi\phi}} - \widehat{\overline{\phi}}\,\widehat{\overline{\phi}} - \widehat{\theta}} = \frac{L_{i\phi}}{\Theta},$$

which leads to (5.3).

Note that in similar manner, we can start with the model assumption $\tau_{i\phi} \approx C_b k$, and arrive at the following model:

$$\tau_{i\phi} \approx \frac{k}{L_{mm}} L_{i\phi}, \tag{5.6}$$

where $L_{mm} = \overline{u_m u_m} - \overline{u}_m\overline{u}_m$.

5.3 *A priori* tests

Figures 5–7 examines the behaviour of the DS model compared to the performance of the models found in the literature: the dynamic eddy-viscosity model (3.13) and the similarity model (3.15). Figure 5–7a presents scatter plots of $\tau_{1,\phi}$ computed from DNS vs. $\tau_{1,\phi}$ predicted by the eddy-viscosity model (3.13) and Dynamic Structure model 5.3. The advantage of the DS model is evident from the values falling closer to the exact correlation line plotted at 45^o. Figure 5–7b shows the PDF of relative error for the DS and similarity model (3.15). For the ideal model, the PDF of relative error should be the Kronecker delta-function $\delta(x)$. Thus the DS model is considered superior since its PDF of relative error has higher peak and lower variance.

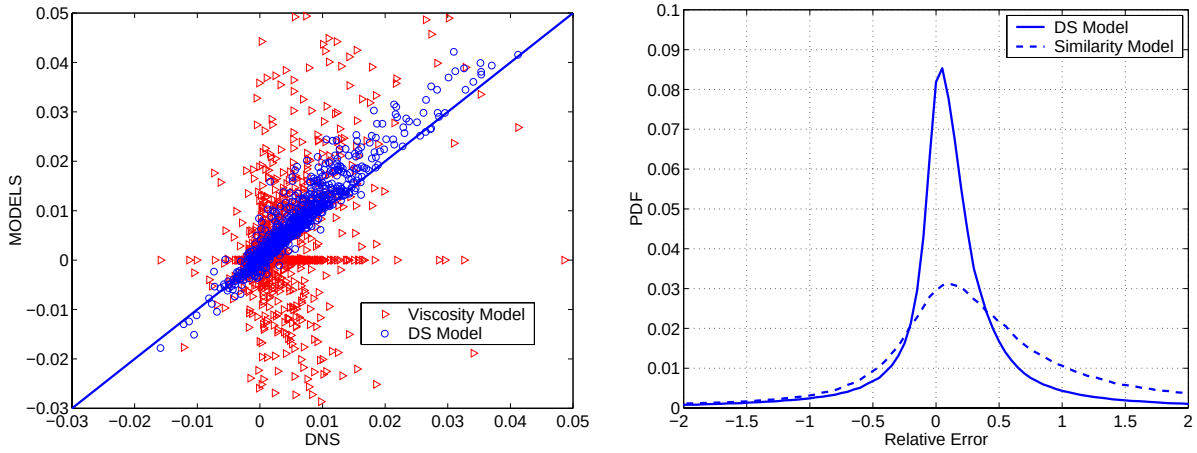

(a) (b)

Figure 5–7: Comparison of *a priori* performance of Dynamic Structure model for $\tau_{1,\phi}$ with other models. For clarity, only x-component is shown. (a) Scatter plot of $\tau_{1,\phi}$ computed from DNS vs. models DS model (circles) and viscosity model (triangles); (b) PDFs of the relative errors for the DS model (solid) and Similarity model (dashed). The data is taken from DNS of mixing layer.

It is obvious from the Figure 5–7 that the viscosity model, which relies on the resolved gradient as a directional vector, poorly predicts the SGS scalar flux. The self-similarity model (3.15), similar to the DS model (5.3), relies on the Leonard vector to get the direction of $\tau_{i\phi}$. As was shown earlier in the Figures 5–1, 5–2, and 5–4, directions of $\tau_{i\phi}$ and $\nabla\overline{\phi}$ are

not the same, and tend to be orthogonal in the presence of strong mean shear. This is the main reason of poor performance of any eddy-viscosity model in *a priori* tests.

Thus the main comparison we are going to make is the one between the performance of the Dynamic Structure model and the Clark model. As it can be seen from Figures 5–1 and 5–2, the DS and Clark models predict the direction of $\tau_{i\phi}$ with comparable degree of accuracy using the channel flow DNS results. It should be noted, though, that the accuracy of DS model is somewhat dependent on the test filter size, while Clark model does not employ the test filter.

To compare the DS and Clark models further, we plotted the transverse profiles of the angles between $\tau_{i\phi}$ and models and also the ratio of predicted and actual magnitudes of $\tau_{i\phi}$ for the DS and Clark models. The results are given in the Figure 5–8.

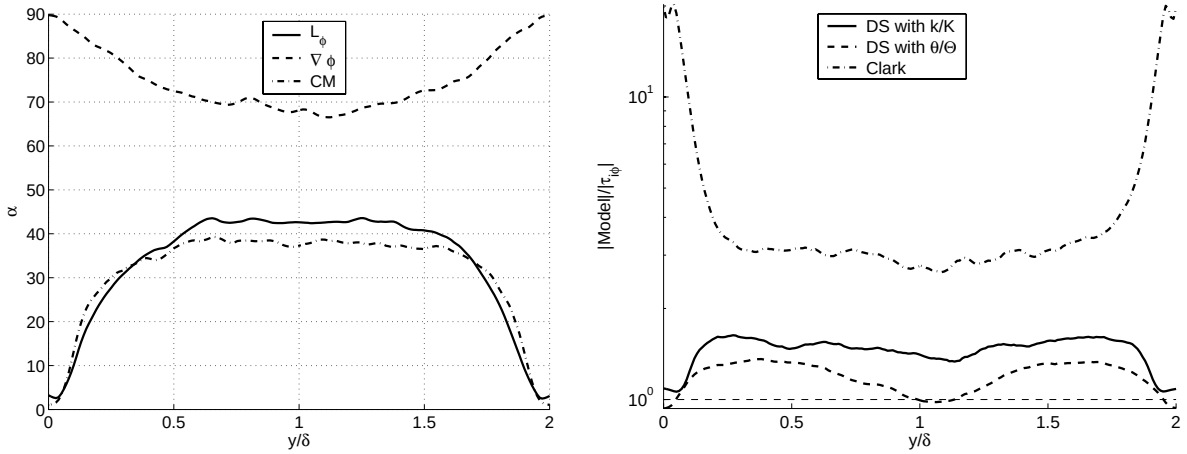

(a) (b)

Figure 5–8: (a) The angle between $\tau_{i\phi}$ and indicated vectors: Leonard term, resolved scalar gradient and Clark model (CM); (b) The ratio of the magnitudes of the modeled and actual SGS scalar flux for DS and Clark models. Both quantities are averaged in homogeneous directions and transverse profiles are plotted.

Figure 5–8a shows the transverse profile of the angle between $\tau_{i\phi}$ and three other vectors: Leonard term $L_{i\phi}$, resolved gradient $\nabla\overline{\phi}$, and the vector given by the Clark model. The angles were averaged along the homogeneous directions (flow direction x and spanwise direction z) and plotted against the y-coordinate. From the Figure it is evident again that the resolved

gradient does not provide the correct direction of the SGS scalar flux. On the other hand, the directions given by the DS and Clark models do not look very good either. We attribute part of this to the fact that the orientation of two vectors in an oriented three-dimensional space is characterized by two angles, not one. The Figure 5–8a depicts only the angle in an unoriented 3-D space.

On the other hand, the ratio of magnitudes of two vectors in any three-dimensional space is a scalar, and averaging in homogeneous directions gives an accurate representation of the scaling trends. Figure 5–8b shows the averaged y-profiles of the ratio of magnitudes of $\tau_{i\phi}$ predicted by models and DNS. Two DS models (5.3) and (5.6) with different scaling factors are evaluated, along with the Clark model. As we can see, the Clark model consistently over-predicts the magnitude of the SGS scalar flux, especially in the areas with considerable mean strain. The best magnitude prediction is given by the DS model (5.3) with scaling factor of θ/Θ. However, using the DS model (5.6) with scaling factor k/K instead of θ/Θ does not significantly damage the accuracy of prediction, and does not require an additional transport equation for the scalar variance θ. This is feasible in, for example, IC engine simulation, where the number of active scalars can be considerably high, and each of those scalars would require either a transport equation for the corresponding θ or a model for it.

Thus, based on our *a priori* evaluation of the DS models, we can conclude that Dynamic Structure Models (5.3) and (5.6) for $\tau_{i\phi}$ predict the direction of $\tau_{i\phi}$ as good as the Clark model, and the magnitude of $\tau_{i\phi}$ at least as good as the Clark model. Moreover, in the areas of the flow with high mean strain, DS models seems to predict the magnitude of SGS scalar flux better than the Clark model, which can over-predict it by an order of magnitude. This tendency could increase with the Reynolds number.

Chapter 6. SGS Scalar Dissipation model

6.1 Introduction

The SGS dissipation of a scalar ϕ is given by

$$\chi_s = 2D\left[\overline{\frac{\partial\phi}{\partial x_i}\frac{\partial\phi}{\partial x_i}} - \frac{\partial\overline{\phi}}{\partial x_i}\frac{\partial\overline{\phi}}{\partial x_i}\right]. \tag{6.1}$$

In the literature a lot of effort is being spent on modeling of the the term

$$\overline{\chi} = 2D\overline{\frac{\partial\phi}{\partial x_i}\frac{\partial\phi}{\partial x_i}} = \chi_r + \chi_s, \tag{6.2}$$

where χ_r is the *resolved scalar dissipation*

$$\chi_r = 2D\frac{\partial\overline{\phi}}{\partial x_i}\frac{\partial\overline{\phi}}{\partial x_i}, \tag{6.3}$$

obtained from the resolved field.

In the literature, models for $\overline{\chi}$ are proposed and evaluated[21,33] and $\overline{\chi}$ is referred to as "subgrid scalar dissipation". We feel that this expression is more suitable for the term χ_s, since χ_s represents the difference between the total scalar dissipation and the part of it that acts only on resolved scales.

In order to investigate the relative importance of the SGS scalar dissipation, we plotted the average ratio $\chi_s/\overline{\chi}$ versus simulation time, taking the data from the DNS of decaying isotropic turbulence. The result is shown in the Figure 6–1a. It shows that most of the time χ_s is comparable in the magnitude with $\overline{\chi}$ and thus modeling χ_s is important. Figure 6–1b shows the PDF of $\chi_s/\overline{\chi}$ for the snapshot DIT-3, conditioned by $0.2 < \overline{\phi} < 0.8$ to focus on the fully developed regions. The PDF shows that for the regions of the scalar field which

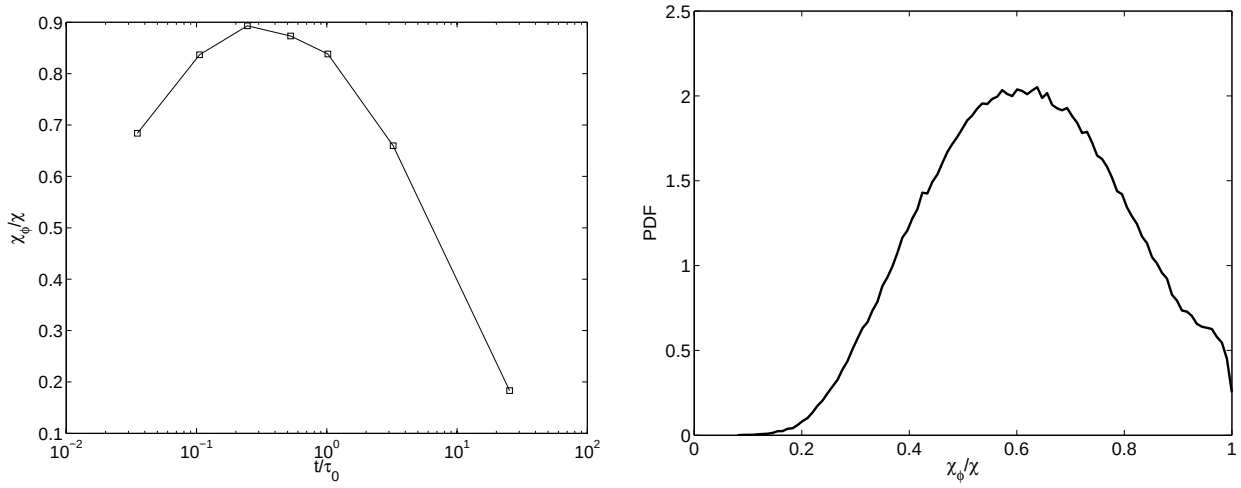

(a) (b)

Figure 6–1: The relative importance of the SGS scalar dissipation χ_s compared to the total scalar dissipation $\overline{\chi}$. The LES filter size was set to 7 DNS cell sizes. For the snapshot parameters, see Table 2. (a) The evaluation of average ratio $\chi_s/\overline{\chi}$ in time (snapshots DIT2 through DIT-8). (b) The PDF of ratio $\chi_s/\overline{\chi}$ for the snapshot DIT-3, conditioned by $0.2 < \overline{\phi} < 0.8$.

are well developed, the SGS scalar dissipation is of the same order of magnitude as the total scalar dissipation.

As we have already seen in the Section 4.5.3, both $\overline{\epsilon}$ and $\overline{\chi}$ tend to be log-normally distributed. Similar distribution is expected from the SGS scalar dissipation since it also falls in the category of flow variables defined by small flow structures. Figures 6–2 and 6–3 show the PDFs of χ_s, their skewness and excess kurtosis.

As it can be seen from the Figure 6–2, χ_s also exhibits log-normal distribution. It should be noted, though, that the parameters of the PDF such as mean, variance and higher moments shown in the Figure 6–3, appear to depend on the developmental stage of the scalar field.

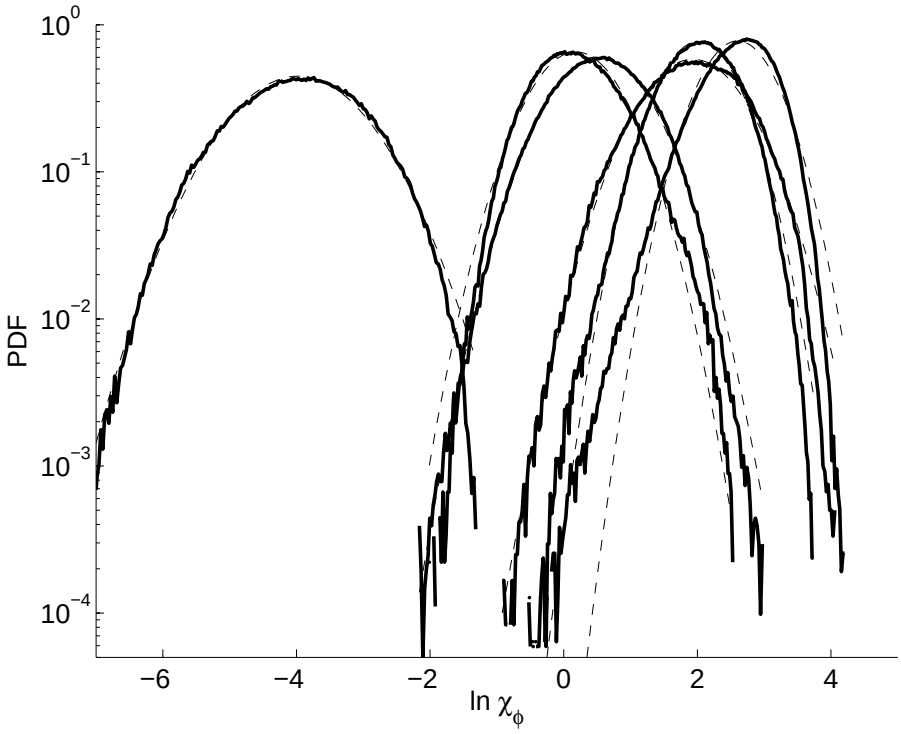

Figure 6–2: Log-normality of χ_s, conditioned by $0.2 < \overline{\phi} < 0.8$. PDFs of $\ln \chi_s$ (DIT-2 through DIT-7). Solid lines are the actual PDFs of $\ln \chi_s$, dashed lines are PDFs of normal distributions that have the same first two moments. The PDFs of $\ln \chi_s$ are: DIT-2 (second from the left), DIT-3 (third from the right), DIT-4 (the first from the right), DIT-5 (second from the right), DIT-6 (third from the left), and DIT-7 (the most left).

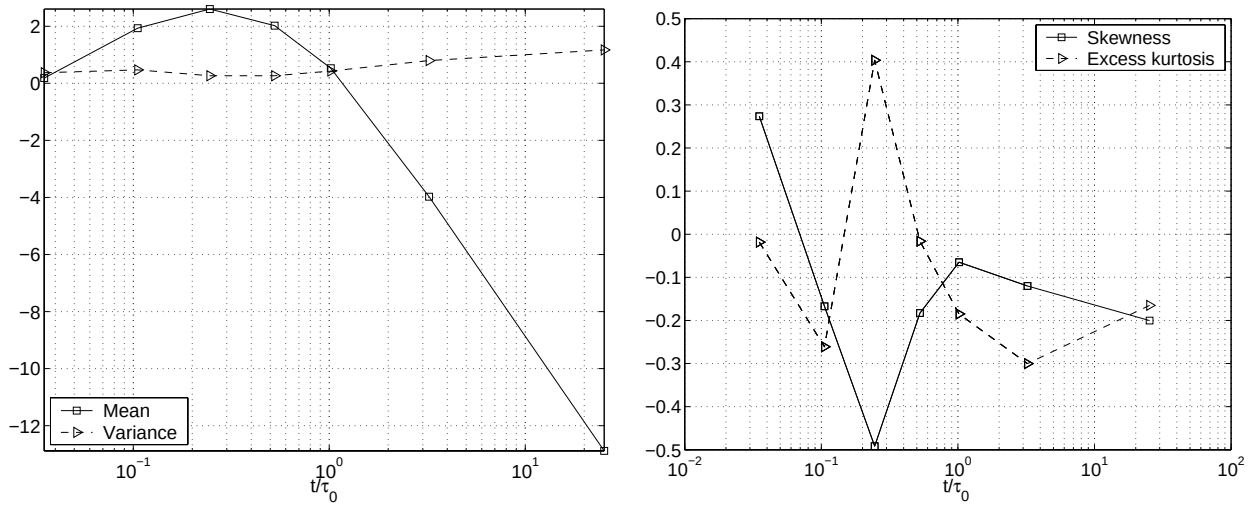

(a) (b)

Figure 6–3: Log-normality of χ_s, conditioned by $0.2 < \overline{\phi} < 0.8$. (a) Mean and variance of $\ln \chi_s$ (DIT-2 through DIT-8). (b) Skewness and excess kurtosis of $\ln \chi_s$. The LES filter size was set to 7 DNS cell sizes. For the snapshot parameters, see Table 2.

6.2 Formulation

A Dynamic Structure (DS) type model for χ_s is the following:

$$\chi_s \approx C_\chi \frac{\theta}{\Theta} L_\chi \equiv C_\chi \frac{\overline{\phi\phi} - \overline{\phi}\,\overline{\phi}}{\widehat{\overline{\phi}\,\overline{\phi}} - \widehat{\overline{\phi}}\,\widehat{\overline{\phi}}} \cdot 2D \left[\widehat{\overline{\frac{\partial\phi}{\partial x_i}}\,\overline{\frac{\partial\phi}{\partial x_i}}} - \widehat{\overline{\frac{\partial\phi}{\partial x_i}}}\,\widehat{\overline{\frac{\partial\phi}{\partial x_i}}} \right], \tag{6.4}$$

where the form of the factor C_χ is to be determined from the a priori tests.

6.3 *A priori* tests

We ran an *a priori* test using the DNS simulation of an incompressible non-reacting mixing layer,[42] described in the chapter 5. Figure 6–4 shows the PDF of relative error for two models: the Dynamic Structure model (6.4) and the momentum-based model (3.17),[33] which we reprint here for convenience:

$$\overline{\chi} \approx \frac{1}{\mathrm{Pr}} \frac{\epsilon}{k} \theta. \tag{6.5}$$

We conducted the *a priori* comparison for several cases. First, we evaluated the models (6.4) and (6.5) using the mixing layer DNS data. The base and test filter sizes were varied, as were the filter shapes. This was done in order to test the robustness of the models. The PDFs shown in Figure 6–4 were computed for various filter dimensions ranging from $3\Delta_g$ to $15\Delta_g$ and from isotropic to highly asymmetric, e.g., $6\Delta_g \times 14\Delta_g \times 10\Delta_g$, where Δ_g is the DNS grid spacing. The quantity modeled is $\overline{\chi}$, and the constant C_χ has been assigned the empirical value of 2. As it can be seen, the sum of DS model (6.4) and the resolved dissipation (6.3) provide what seems to be a better approximation for the value of $\overline{\chi}$ than the momentum analogy model (6.5).

In order to test the DS model further, we performed the same type of a priori testing on the data from DNS of decaying isotropic turbulence. Two snapshots are used — DIT-4 and DIT-7. The data set DIT-4 is chosen because at that particular time the SGS scalar

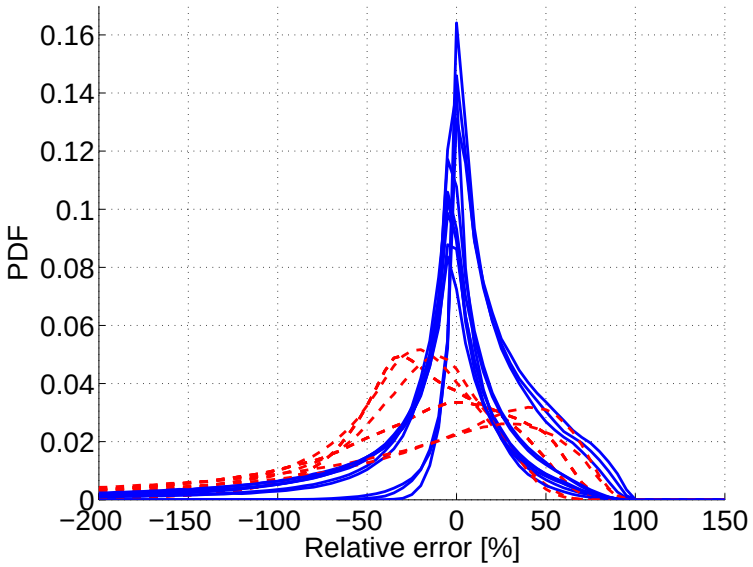

Figure 6–4: PDF of relative error for $\overline{\chi} = \chi_r + \chi_s$, where χ_s is computed by DS model (6.4) with $C_\chi = 2$ (solid); momentum-based model (6.5) for $\overline{\chi}$ (dashed). Different lines correspond to different cases with various base and test filter sizes.

dissipation χ_s is a very significant part of the total scalar dissipation $\overline{\chi}$ (up to 90%, depending on the base filter size). The data from the set DIT-7 is supposed to represent the other case — when the SGS dissipation is not as important (less than 15% of total dissipation, depending on the base filter size). The results of these *a priori* tests are given in Figures 6–5 and 6–6.

The Figure 6–5 shows the PDFs of relative error for the DS model (6.4) for nine different base and test filter sizes, given in the figure legend. We can see that performance of the DS model as it is given by the equation (6.4) is heavily dependent on the size of the base filter. For both data sets, PDFs can be distinctly divided into three groups that correspond to three different base filter sizes.

For the snapshot DIT-4, where the SGS dissipation contributes up to 90% to the total scalar dissipation, the best model performance is achieved when the base filter size is the smallest. For the snapshot DIT-7, where the SGS dissipation is not that important, the best performance is observed for the case of $\Delta = 5\Delta_{DNS}$. This leads to several conclusions.

First, if we utilize the model (6.4) for the SGS scalar dissipation, the value of the constant

C_χ should depend on the LES grid size, which usually scales with the LES base filter size Δ. Secondly, the value of C_χ seems to depend on additional factors. One such factor may be the ratio of Δ and the Batchelor length scale

$$L_B = (D/\gamma)^{1/2}, \qquad \gamma = (\epsilon/\nu)^{1/2}, \tag{6.6}$$

where D is the diffusion coefficient and γ is the strain parameter.

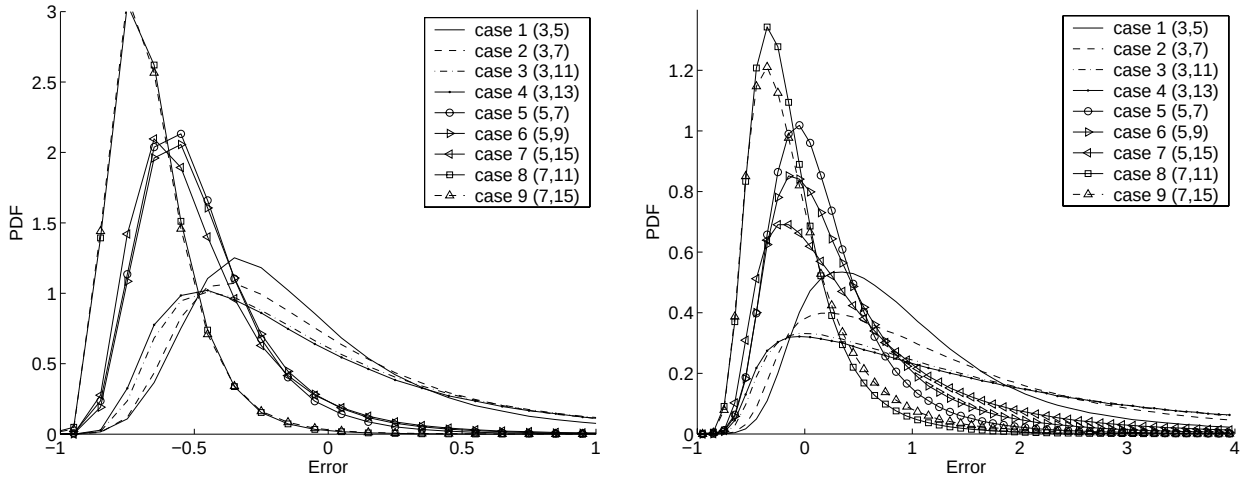

(a) (b)

Figure 6–5: PDF of relative error in modeling the SGS scalar dissipation χ_s for (a) DIT-4, (b) DIT-7. Figures in parentheses denote the base and test filter sizes in terms of DNS grid cells.

For DIT-4, $L_B/\Delta \approx 0.45$, while for DIT-7, $L_B/\Delta \approx 1$. This motivated us to look for C_χ in the following form:

$$C_\chi = C\frac{\Delta}{L_B},$$

where L_B is the local Batchelor scale computed using the local value of the filtered energy dissipation $\bar{\epsilon}$.

Figures 6–7 and 6–8 show the distribution of relative error that characterize models (6.4) and (6.5) with $C_\chi = 0.2\Delta/L_B$. As it can be seen, the performance of the DS model with this particular form of C_χ have significantly improved and does not appear to depend as much on the Reynolds number of the flow. The peaks of the PDFs are higher and the variance of

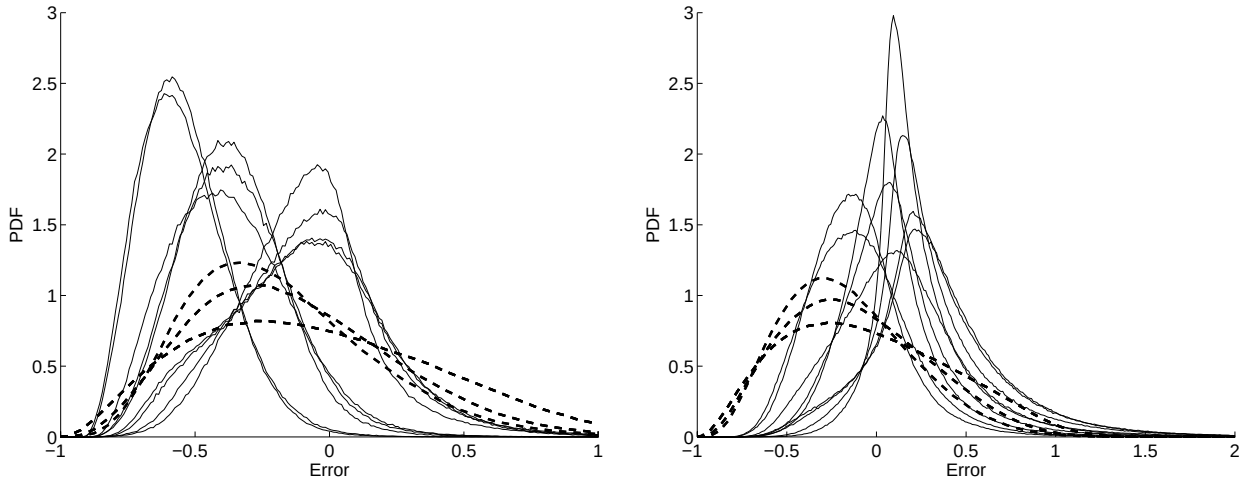

Figure 6–6: PDF of relative error in modeling the total scalar dissipation $\overline{\chi}$. Solid lines correspond to $\chi_r + \chi_s$, where χ_s is given by the DS model (6.4). Dashed lines correspond to the momentum-based model (6.5). (a) DIT-4, (b) DIT-7.

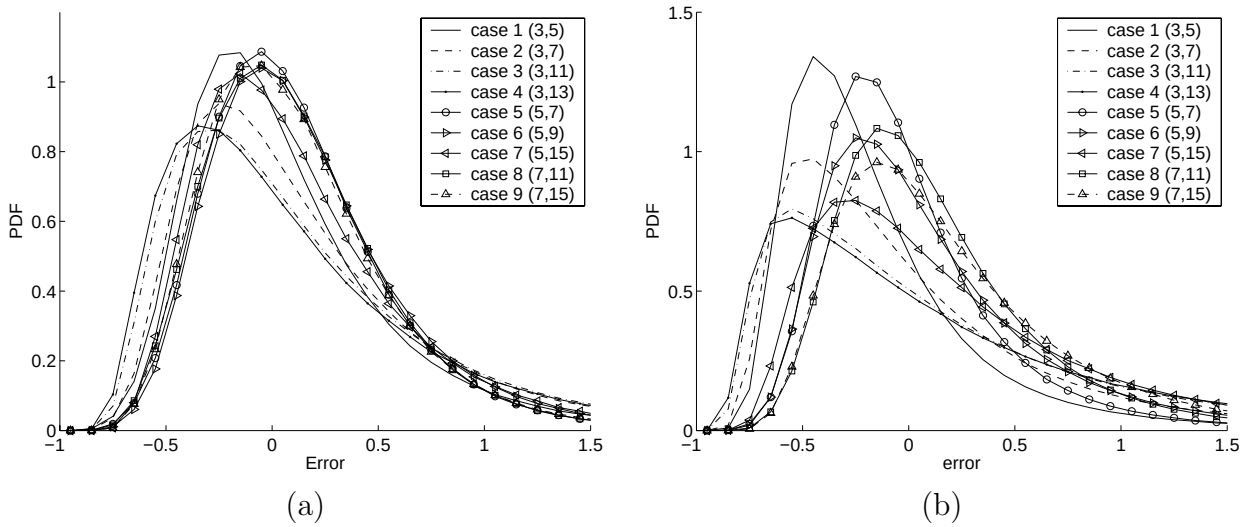

Figure 6–7: PDF of relative error in modeling the SGS scalar dissipation χ_s for (a) DIT-4, (b) DIT-7. Figures in parentheses denote the base and test filter sizes in terms of DNS grid cells.

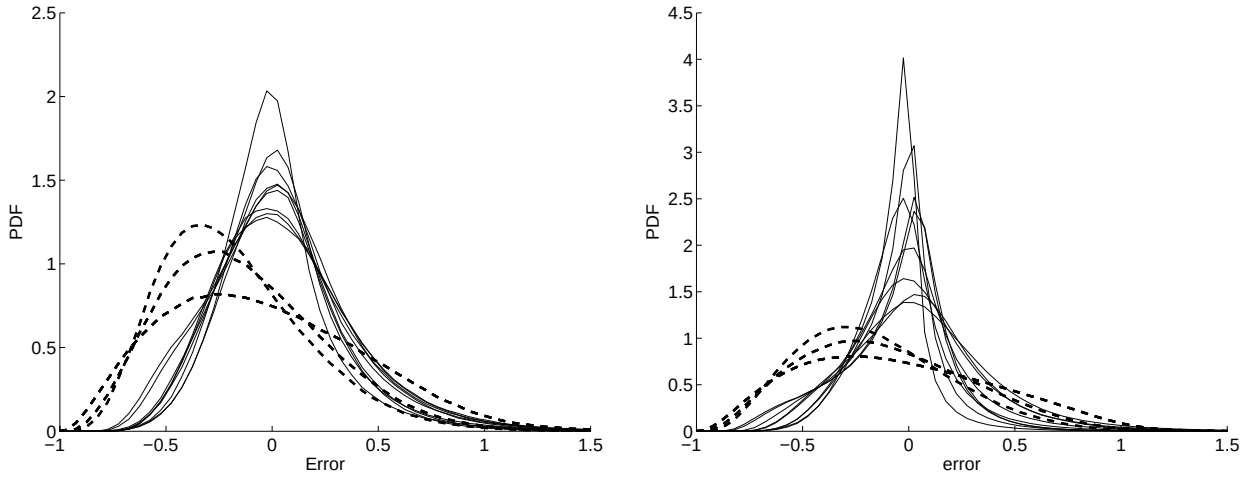

(a) (b)

Figure 6–8: PDF of relative error in modeling the total scalar dissipation $\overline{\chi}$. Solid lines correspond to $\chi_r + \chi_s$, where χ_s is given by the DS model (6.4). Dashed lines correspond to the momentum-based model (6.5). (a) DIT-4, (b) DIT-7.

relative errors seem to be lower than for the momentum-based model (6.5).

Overall, the modified DS model (6.4) with $C_\chi = 0.2\Delta/L_B$ was found to perform better in *a priori* tests than the momentum-based model (6.5). Similar results are obtained by using the SGS energy dissipation ϵ_s instead of $\overline{\epsilon}$ for calculation of L_B (not shown).

The drawback of the modified DS model is that in order to calculate the local Batchelor length scale L_B one needs to know the local dissipation $\overline{\epsilon}$ which is not known in LES calculations. This couples the DS model for χ_s with the model for $\overline{\epsilon}$, or with the model for ϵ_s, which is discussed in the next chapter.

Chapter 7. A Model for SGS Energy Dissipation

7.1 Formulation

The filtered momentum equation contains an unclosed term

$$\overline{\epsilon} = \nu \overline{\frac{\partial u_i}{\partial x_j} \frac{\partial u_i}{\partial x_j}}, \tag{7.1}$$

which is referred to as *filtered dissipation*. We can either try to model $\overline{\epsilon}$ directly or we can combine it with the resolved dissipation and model the difference

$$\epsilon_s = \nu \left[\overline{\frac{\partial u_i}{\partial x_j} \frac{\partial u_i}{\partial x_j}} - \frac{\partial \overline{u}_i}{\partial x_j} \frac{\partial \overline{u}_i}{\partial x_j} \right], \tag{7.2}$$

which we call *SGS energy dissipation*.

The name "SGS energy dissipation" has two different meanings encountered in the literature. For zero-equation models the "SGS energy dissipation" might refer to the term

$$\Pi = -\tau_{ij} \overline{S}_{ij}, \tag{7.3}$$

which acts like a source or sink for the resolved kinetic energy $K = \overline{u}_i \overline{u}_i / 2$.[7] For one-equation models, and for the remainder of this document, the term "SGS energy dissipation" refers to (7.2), which is responsible for the energy removal from the unresolved scales. The term (7.3) can be referred to as the "Energy transfer term" since it is responsible for the energy transfer between resolved and unresolved scales.

Thus our primary goal in this chapter is to formulate and validate a model for ϵ_s.

The proposed form of the model is

$$\epsilon_s \approx \nu F \left[\widehat{\frac{\partial \overline{u}_i}{\partial x_j} \frac{\partial \overline{u}_i}{\partial x_j}} - \widehat{\frac{\partial \overline{u}_i}{\partial x_j}} \widehat{\frac{\partial \overline{u}_i}{\partial x_j}} \right], \tag{7.4}$$

where F is a function to be determined by *a priori* tests and verified by *a posteriori* tests.

7.2 *A priori* tests

7.2.1 Relative importance of SGS energy dissipation

First, we should demonstrate that the subgrid energy dissipation plays an important role in the LES simulation. For this, we calculated the percentage of the total filtered dissipation, given by the SGS dissipation using the DNS data for isotropic turbulence. The results are shown in the Figure 7–1.

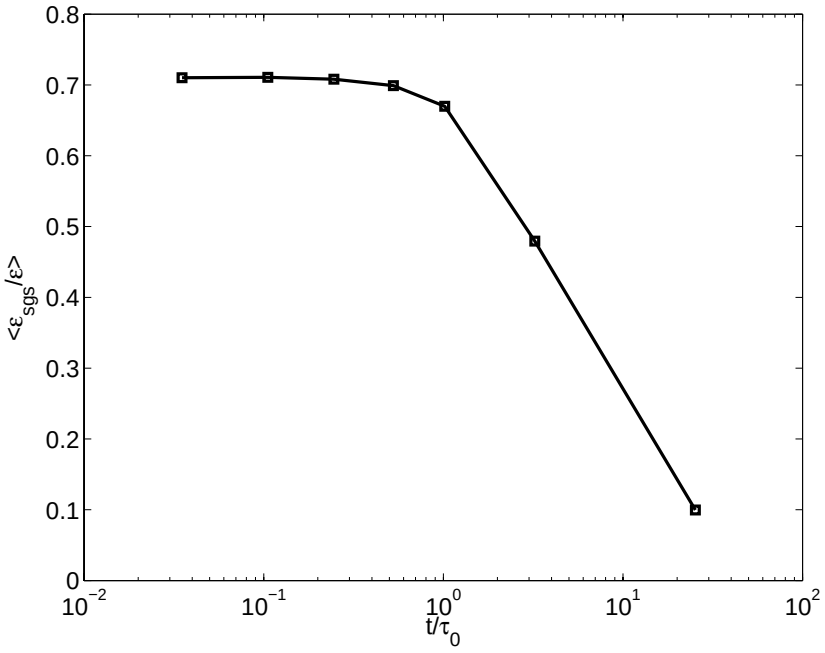

Figure 7–1: Fraction of the filtered dissipation $\bar{\epsilon}$ stored in the SGS energy dissipation ϵ_s vs. simulation time. The time is normalized by the initial eddy turnover time. The points correspond to the snapshots DIT-2 through DIT-8. The base filter size is taken to be 7 DNS grid spacings.

It is evident from Figure 7–1 that during the inertial period of the flow development the SGS energy dissipation represents more than half of the total filtered dissipation, and thus is important to model. When the flow approaches the final period of decay and starts being

fully resolved, which starts to happen at $\mathrm{Re}_\lambda \approx 25$ ($t/\tau_0 \approx 3.2$), the SGS energy dissipation becomes less important. This is illustrated by the last data entry in Figure 7–1 (DIT-8).

7.2.2 *A priori* investigation of the scaling factor

In order to obtain sufficient information about the behaviour of SGS dissipation and F in particular, we varied the size of the base and test filters in our *a priori* tests. From initial studies the following shape of F has been assumed

$$F = C_\epsilon \left[\frac{2k}{L_{kk}} \right]^\gamma,$$

and PDFs for C_ϵ have been computed for various values of γ. From our point of view, the most successful value for γ has been 0.5, leading to

$$\epsilon_s \approx C_\epsilon \sqrt{\frac{2k}{L_{kk}}} \cdot \nu \left[\widehat{\frac{\partial \overline{u}_i}{\partial x_j}} \widehat{\frac{\partial \overline{u}_i}{\partial x_j}} - \widehat{\frac{\partial \overline{u}_i}{\partial x_j}} \widehat{\frac{\partial \overline{u}_i}{\partial x_j}} \right]. \tag{7.5}$$

Figure 7–2 shows PDFs for C_ϵ in (7.5) for various base and test filter sizes.

It is evident from Figure 7–2 that for $\gamma = 0.5$, during the inertial period of decay of isotropic turbulence, the scaling coefficient C_ϵ exhibits a clear dependence on the base filter size. This dependence manifests itself in the fact that the PDFs for C_ϵ can be clearly divided in three groups, which correspond to different base filter sizes, in our case $3\Delta_{DNS}$, $5\Delta_{DNS}$, and $7\Delta_{DNS}$. This might be indicative of the dependence of C_ϵ on the SGS Reynolds number, which can be defined in several ways, e.g., $\mathrm{Re}_\Delta = \sqrt{\mathrm{k}}\Delta/\nu$, or $\mathrm{Re_s} = \mathrm{k}/|\mathrm{S_{ij}}|\nu$.

We tried the following form of C_ϵ:

$$C_\epsilon = C\frac{\Delta}{\eta}, \tag{7.6}$$

where $\eta \equiv (\nu^3/\epsilon)^{1/4}$ is Kolmogorov length scale, determined using either global or local value of ϵ.

Figure 7–3 demonstrates the PDFs of the constant C in the following model:

$$\epsilon_s \approx \nu \cdot C \cdot \frac{\Delta}{\eta} \sqrt{\frac{k}{L_{mm}}} \left[\widehat{\frac{\partial \overline{u}_i}{\partial x_j}} \widehat{\frac{\partial \overline{u}_i}{\partial x_j}} - \widehat{\frac{\partial \overline{u}_i}{\partial x_j}} \widehat{\frac{\partial \overline{u}_i}{\partial x_j}} \right], \tag{7.7}$$

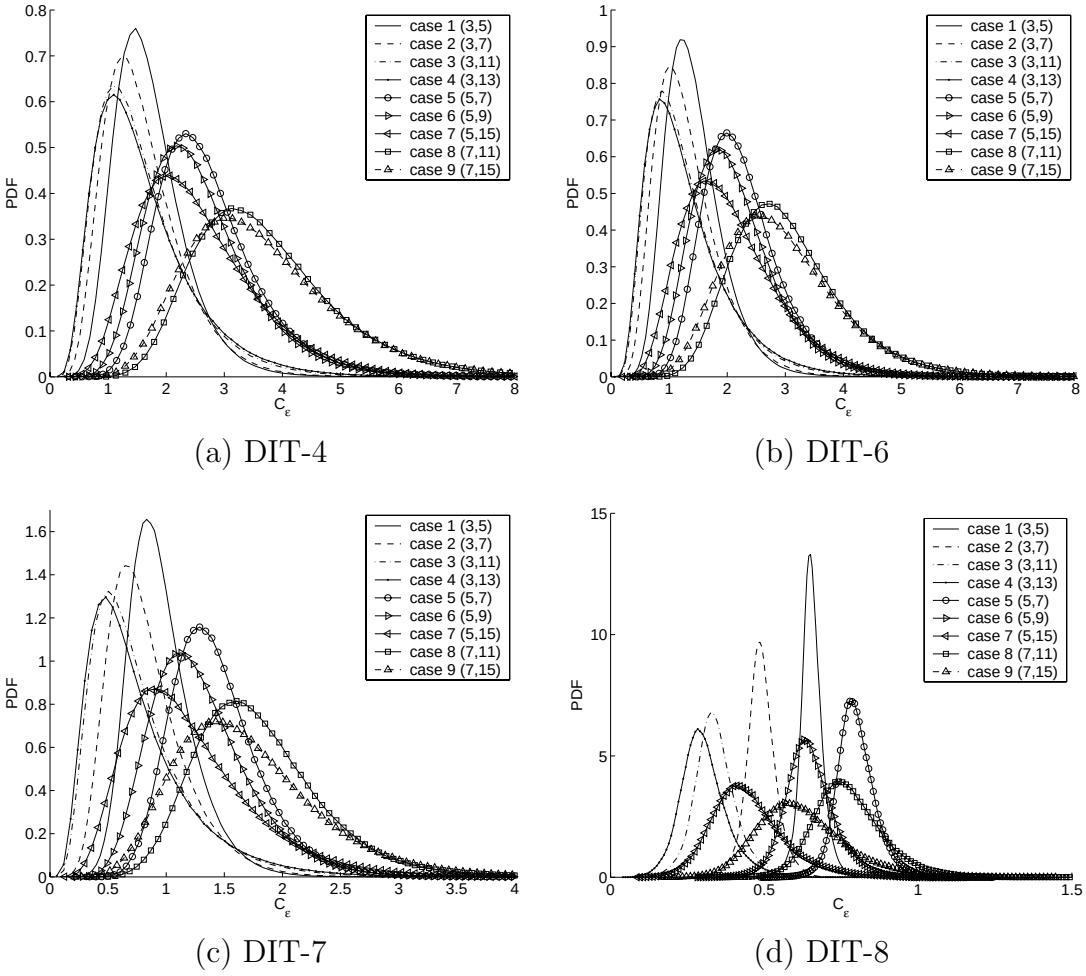

(a) DIT-4 (b) DIT-6

(c) DIT-7 (d) DIT-8

Figure 7–2: PDF for the scaling coefficient C_ϵ in (7.5) obtained *a priori*. The figures in parenthesis indicate the dimensions of the base and test filters in terms of DNS grid cells.

computed from four snapshots of DNS of DIT. The Figure suggests that for Reynolds numbers Re_λ higher than 25, the following scaling holds:

$$C_\epsilon = 0.25\frac{\Delta}{\eta}. \tag{7.8}$$

The global value of the dissipation ϵ was used to obtain Kolmogorov scale η in (7.8).

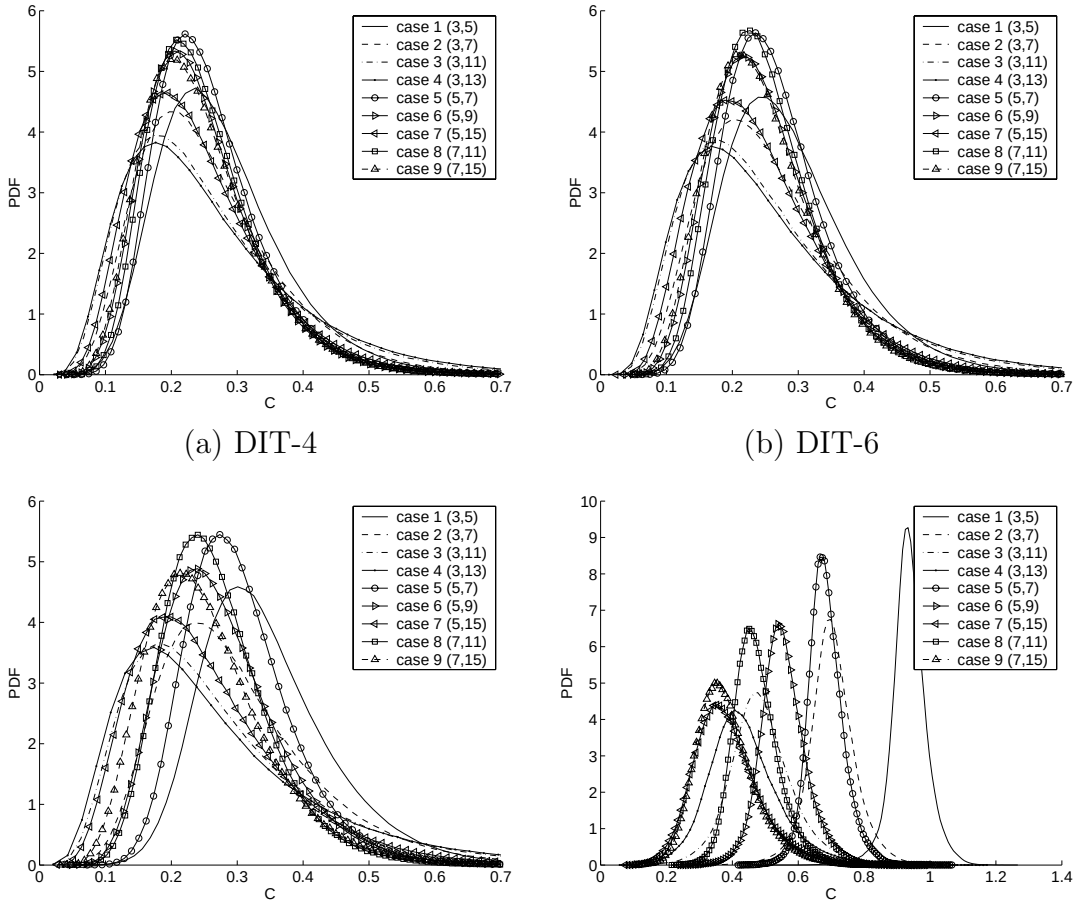

(a) DIT-4 (b) DIT-6

(c) DIT-7 (d) DIT-8

Figure 7–3: PDF for the scaling coefficient C in (7.7), obtained *a priori*. The figures in parenthesis indicate the dimensions of the base and test filters in terms of DNS grid cells.

Another approach is to express the local Kolmogorov length scale η via the SGS energy dissipation: $\eta = A(\nu^3/(\epsilon_s))^{1/4}$. The constant A reflects the fact that the SGS energy dissipation constitutes only a fraction of the total local energy dissipation. Then we can solve

for ϵ_s algebraically, resulting in

$$(\epsilon_s)^{3/4} \approx \nu \frac{\Delta}{A\nu^{3/4}} \sqrt{\frac{k}{L_{mm}}} \left[\widehat{\frac{\partial \overline{u}_i}{\partial x_j}} \widehat{\frac{\partial \overline{u}_i}{\partial x_j}} - \widehat{\frac{\partial \overline{u}_i}{\partial x_j}} \widehat{\frac{\partial \overline{u}_i}{\partial x_j}} \right]. \tag{7.9}$$

Figure 7–4 shows the PDF of relative error for the model (7.9) with $A = 4$, evaluated *a priori* on the data from DNS of DIT. Again, the proposed models performs well for intermediate Reynolds numbers ($\mathrm{Re}_\lambda > 25$). For lower Reynolds numbers the SGS energy dissipation appears to be not as important as resolved energy dissipation (see Figure 7–1) — at least, for the given spatial resolution (128^3). Thus model performance for low Reynolds numbers (DIT-8) is not very critical.

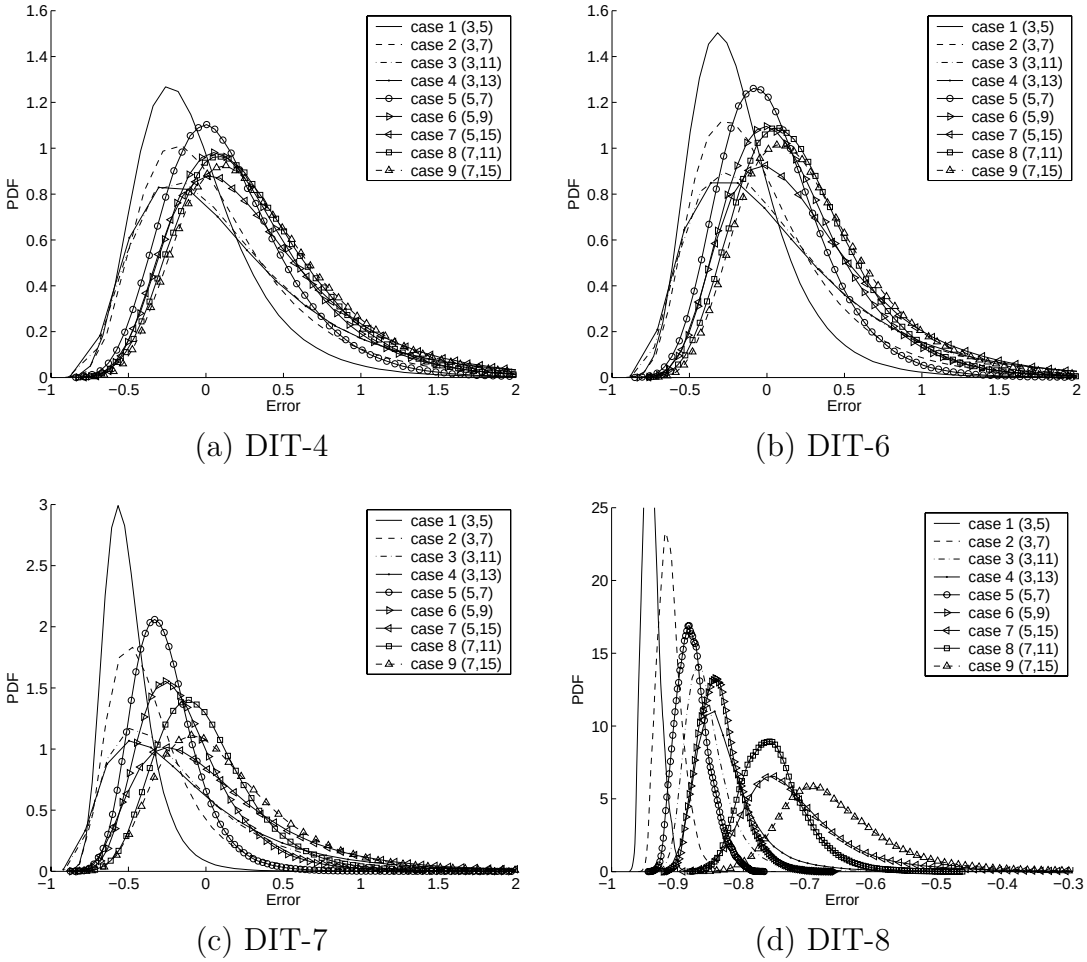

(a) DIT-4 (b) DIT-6

(c) DIT-7 (d) DIT-8

Figure 7–4: PDF of relative error for the model (7.9) with $A = 4$. Data from the DNS of decaying isotropic turbulence is used.

For comparison, Figures 7–5 shows the PDF for scaling coefficient C in the classic dissipation model[65]

$$\epsilon_S \approx C\frac{k^{3/2}}{\Delta}. \tag{7.10}$$

Since the model does not employ test filtering, instead of 9 cases as in Figure 7–3, we have only 3. As it can be seen, the model coefficient C is not a constant as well. The data from DNS of isotropic turbulence[75] with $\mathrm{Re}_\lambda = 105$ is used. We do not investigate this model further, reasoning given in the next chapter.

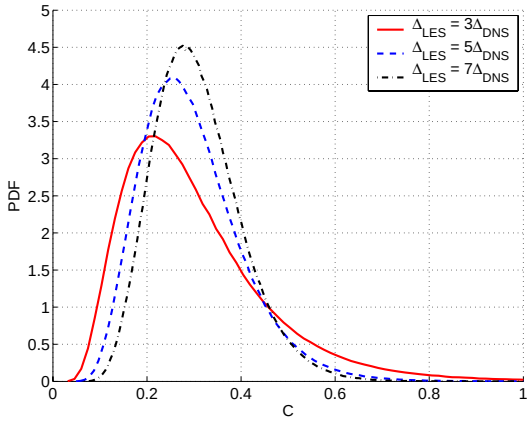

Figure 7–5: PDF for the scaling coefficient C for the model (7.10). The data from decaying isotropic turbulence[75] with $\mathrm{Re}_\lambda = 105$ is used.

Chapter 8. *A posteriori* Model Evaluation

8.1 Introduction

8.1.1 General notes

In this chapter, we focus on *a posteriori* evaluations of LES SGS models described in the previous chapters. The *a posteriori* tests performed include: a non-reacting mixing layer with a passive scalar, a decaying isotropic turbulence simulation, and a coaxial combustor.

8.1.2 The code used: TURF

TURF (as in TUrbulent Flow) code has been developed at ERC as a DNS code for incompressible flow simulation using low Mach number approximation and later modified to include the possibility of LES.[13,23,42] The main code features are:

- finite differences used for spatial discretization on a non-staggered grid
- arbitrary high order in space
- 3rd, 4th or 5th order accuracy in time using explicit Runge-Kutta type scheme
- Poisson equation for pressure is solved using multigrid method
- Skewed stencils for the convective part of governing equations

8.2 Decaying Isotropic Turbulence

8.2.1 Computing the DIT characteristics from LES

In the literature one can find several parameters that are customarily used to characterize isotropic turbulent flow. Namely,

1. The RMS velocity u' (assuming zero mean velocity), given by

$$u' = \sqrt{\frac{1}{3}\left\langle u_1^2 + u_2^2 + u_3^2 \right\rangle} \tag{8.1}$$

2. Dissipation rate ϵ given by

$$\epsilon = 2\nu \left\langle S_{ij} S_{ij} \right\rangle, \qquad S_{ij} = \frac{1}{2}\left[\frac{\partial u_i}{\partial x_j} + \frac{\partial u_j}{\partial x_i}\right] \tag{8.2}$$

3. The Taylor microscale λ given by $\lambda^2 = 15\nu\frac{u'^2}{\epsilon}$,

4. Taylor microscale Reynolds number $\mathrm{Re}_\lambda = \frac{u'\lambda}{\nu}$,

5. Kolmogorov length scale $\eta = (\nu^3/\epsilon)^{1/4}$,

where angle brackets indicate the averaging over the entire $(2\pi)^3$ domain. It is clear that the first two quantities together with the kinematic viscosity ν define the rest.

In LES calculations one cannot apply the definitions (8.1) and (8.2) directly because the strain rate tensor S_{ij} and velocities u_i are not accessible. Instead one has access to the resolved velocities $\overline{u}_i$ and the resolved strain-rate tensor $\overline{S}_{ij} = \frac{1}{2}\left[\frac{\partial \overline{u}_i}{\partial x_j} + \frac{\partial \overline{u}_j}{\partial x_i}\right]$. However, one can use the available SGS kinetic energy k and the SGS stress τ_{ij} in order to find u' and ϵ in the following fashion.

First, we shall prove the following lemma.

Lemma 1. For any flow variable f in the periodic $(2\pi)^3$ domain the following holds:

$$\langle f \rangle = \left\langle \overline{f} \right\rangle, \tag{8.3}$$

where the angle brackets indicate the volume averaging over entire domain, and overbar denotes the spatial filtering.

Proof. Suppose $V = (2\pi)^3$ is the volume of the triple-periodic box, S is the support of the filter function G. By definition,

$$\begin{aligned} \left\langle \overline{f} \right\rangle &= \frac{1}{V} \int_V (f * G)(x)\, dx = \frac{1}{V} \int_V \int_S f(x+z) G(z)\, dz\, dx = \\ &= \int_S \left[\frac{1}{V} \int_V f(x+z)\, dx \right] G(z)\, dz = \int_S \langle f \rangle \cdot G(z)\, dz = \langle f \rangle . \end{aligned}$$

Q.E.D.

Using (8.3), one can obtain the following expression for u':

$$u' = \sqrt{\frac{1}{3} \langle u_i u_i \rangle} = \sqrt{\frac{1}{3} \langle \overline{u_i u_i} \rangle} = \sqrt{\frac{1}{3} \langle \overline{u}_i\, \overline{u}_i \rangle + \frac{2}{3} \langle k \rangle}.$$

Using the fact that

$$2 S_{ij} S_{ij} = \frac{\partial u_i}{\partial x_j} \frac{\partial u_i}{\partial x_j} + \frac{\partial^2 u_i u_j}{\partial x_i \partial x_j},$$

one can compute ϵ as follows:

$$\begin{aligned} \epsilon &= \nu \left\langle \frac{\partial u_i}{\partial x_j} \frac{\partial u_i}{\partial x_j} + \frac{\partial^2 u_i u_j}{\partial x_i \partial x_j} \right\rangle \\ &= \nu \left\langle \overline{\frac{\partial u_i}{\partial x_j} \frac{\partial u_i}{\partial x_j}} + \overline{\frac{\partial^2 u_i u_j}{\partial x_i \partial x_j}} \right\rangle \\ &= \nu \left\langle \frac{\partial \overline{u}_i}{\partial x_j} \frac{\partial \overline{u}_i}{\partial x_j} + \frac{\partial^2 \overline{u}_i \overline{u}_j}{\partial x_i \partial x_j} + \frac{\epsilon_s}{\nu} + \frac{\partial^2 \tau_{ij}}{\partial x_i \partial x_j} \right\rangle \end{aligned}$$

Thus we can summarize:

$$u' = \sqrt{\frac{1}{3} \langle \overline{u}_i \overline{u}_i + 2k \rangle} \tag{8.4}$$

$$\epsilon = 2\nu \langle S_{ij} S_{ij} \rangle = 2\nu \left\langle \overline{S}_{ij} \overline{S}_{ij} \right\rangle + \langle \epsilon_s \rangle + \left\langle \frac{\partial^2 \tau_{ij}}{\partial x_i \partial x_j} \right\rangle. \tag{8.5}$$

8.2.2 Numerical setup

All simulations were performed using the TURF code.

- The $(2\pi)^3$ triple-periodic domain was discretized using various resolution - from 16^3 to 64^3 points. We only show the results from the 32^3 run.
- The degree of spatial approximation was chosen to be 7th order accurate.
- The third order accuracy in time was chosen.
- In order to match the physical experiments by Comte-Bellot and Corrsin,[18] the following length and time scales were chosen for normalization:
  - Length scale $l_* = 10M$, $M = 2$ in;
  - Time scale $t_* = 64M/U_0$, $U_0 = 10$ m/s.

  Thus the length scale of the simulation is $l_*/2\pi = 8.085071$ cm, and the time scale is $t_* = 0.32512$ s. Using these quantities, $\nu_{\text{DNS}} = \nu_{\text{air}} \frac{t_*}{l_*} = 7.539e-04$ (the ν_{air} is the viscosity of air at 20^oC).
- Initial velocity field has been obtained from the DNS spectral code by Rogallo.[55] The DNS velocity field had been initialized using random phases and allowed to evolve in time until structures of desired size formed. Then the DNS data was filtered and used as initial velocity field for LES.
- Initial values of SGS kinetic energy k were approximated by the first two terms of series (3.8) using the resolved velocity field.

8.2.3 Simulation results

The following two sets of models have been tested *a posteriori*:

1. Dynamic Structure (DS) models

$$\tau_{ij} \approx \frac{2k}{L_{kk}} \left[\widehat{\overline{u}_i \overline{u}_j} - \widehat{\overline{u}}_i \widehat{\overline{u}}_j \right], \tag{8.6}$$

$$\epsilon_s \approx \nu C_\epsilon \frac{2k}{L_{kk}} \left[\widehat{\frac{\partial \overline{u}_i}{\partial x_j} \frac{\partial \overline{u}_i}{\partial x_j}} - \widehat{\frac{\partial \overline{u}_i}{\partial x_j}} \widehat{\frac{\partial \overline{u}_i}{\partial x_j}} \right], \tag{8.7}$$

2. The RANS-type model (referred to as "Localization Model"):[22,35,43,62]

$$\tau_{ij} \approx -0.05 \sqrt{k} \Delta \, S_{ij} \tag{8.8}$$

$$\epsilon_s \approx 1.0 \frac{k^{3/2}}{\Delta} \tag{8.9}$$

Figures 8–1 through 8–5 present the preliminary results from LES runs. The first run, referred to as "DS" in figures, uses the first set of models with $C_\epsilon = 8$. The second run uses the second set of models and is referred to as "LM" in the figures. For the LM set of models, the Dynamic Procedure can be applied in order to estimate the *a priori* given coefficients.[22,62] However, the resulting integral equation is not always solvable thus we used constant coefficients that resulted in the best performance of the given set of models. Both runs were performed using 32^3 computational grid.

Figures 8–1 through 8–5 depict the evolution in time of several quantities: total kinetic energy (resolved plus SGS), SGS kinetic energy, the energy transfer between resolved and SGS scales, SGS energy dissipation, and Reynolds number Re_λ based on the Taylor microscale λ. The latter has been estimated using (8.5).

As we can see from figure 8–1, both models seem to be able to capture the total energy decay rate quite efficiently. The separation between inertia-dominated and viscosity-dominated regimes is clearly visible. The slopes on the log-log plots match the theoretical and experimental predictions well. However, in the LM run, the transition to the "final" (viscosity-dominated) phase of turbulence is more spread out in time – approximately between $t = 20 \ldots 60$, as opposed to between $t = 30 \ldots 50$ for the DS run..

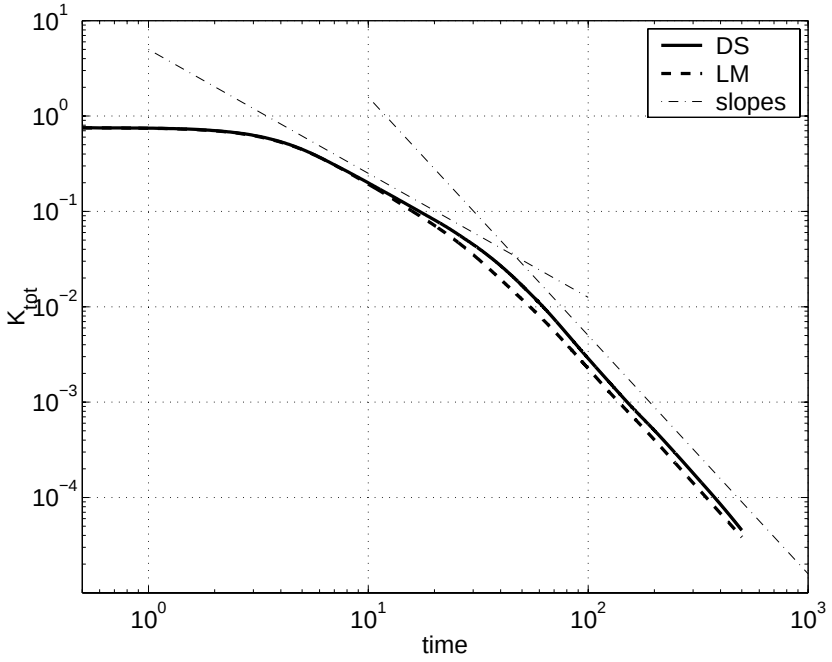

Figure 8–1: Decay of total kinetic energy in time: 32^3 LES. Slopes of -1.3 and -2.5 are plotted.

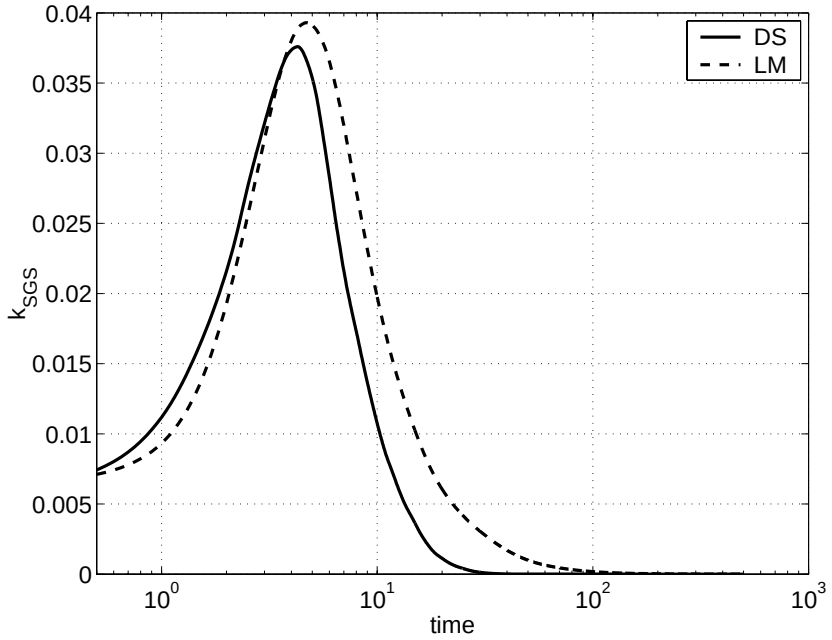

Figure 8–2: Decay of SGS kinetic energy in time: 32^3 LES.

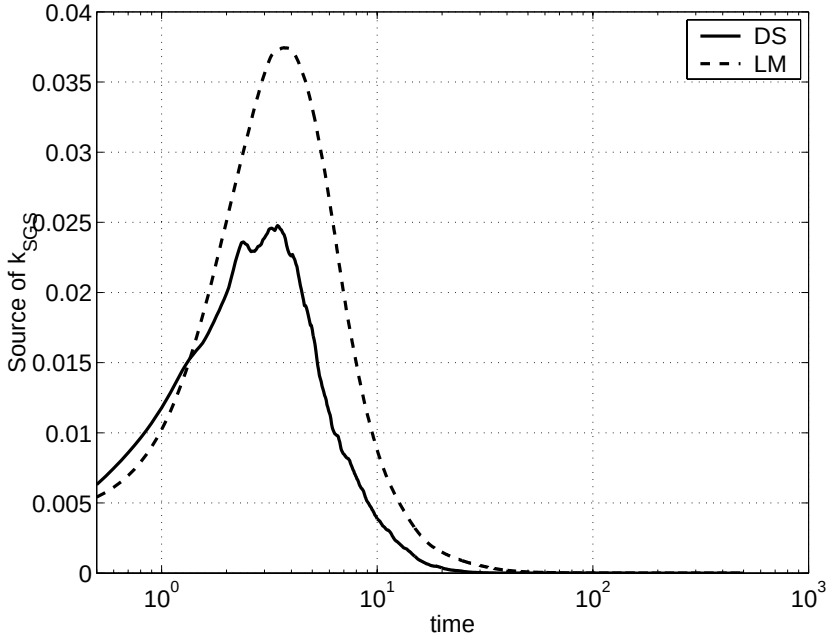

Figure 8–3: Energy transfer between resolved and SGS scales: 32^3 LES.

The Figure 8–2 shows the evolution of the SGS kinetic energy in time. For the LM run, k appears to grow slower but later in time more energy is stored in subgrid scales. This agrees with Figure 8–3, where the energy transfer term is shown. The non-smoothness of the transfer term profile for the DS run is attributed to more significant amount of backscatter than in the LM run.

The Figures 8–4 examines behaviour of the SGS dissipation term in time. Overall, the DS run predicts smaller SGS dissipation than the LM run. This may result in the earlier transition to the viscosity-dominated phase in the LM run.

Figure 8–5 presents the evolution of the Taylor microscale Reynolds number Re_λ for both runs. The values of Re_λ are estimated using (8.5). It should be noted that according to the Figure 8–5, transition to the "final" phase occurs at $\mathrm{Re}_\lambda \approx 60$ for the DS run and $\mathrm{Re}_\lambda \approx 30$ for the LM run. In the literature,[57] the Reynolds numbers that correspond to the "final" phase are described as "significantly lower than ones of interest" which contradicts predictions from both runs. On the other hand, Chasnov[11] indicates that the scaling laws

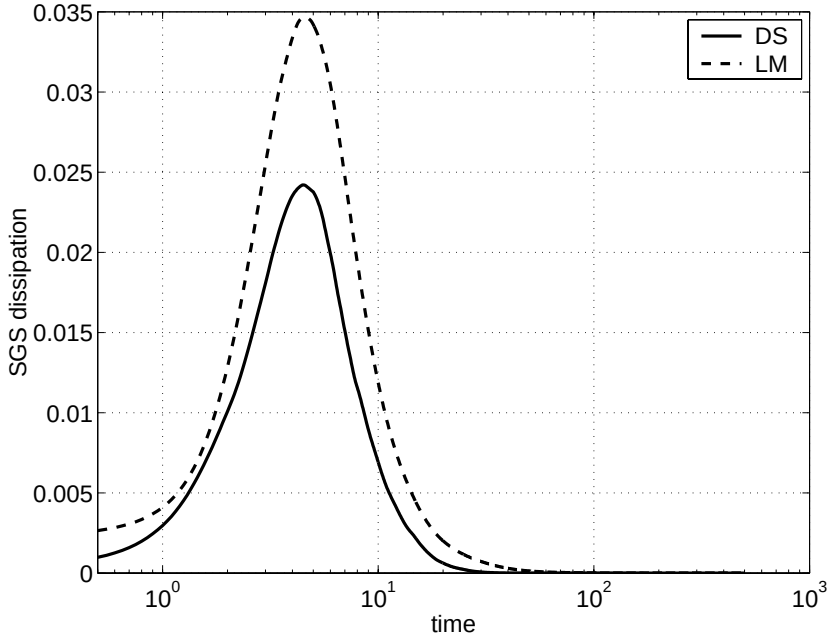

Figure 8–4: Dissipation of SGS kinetic energy: 32^3 LES.

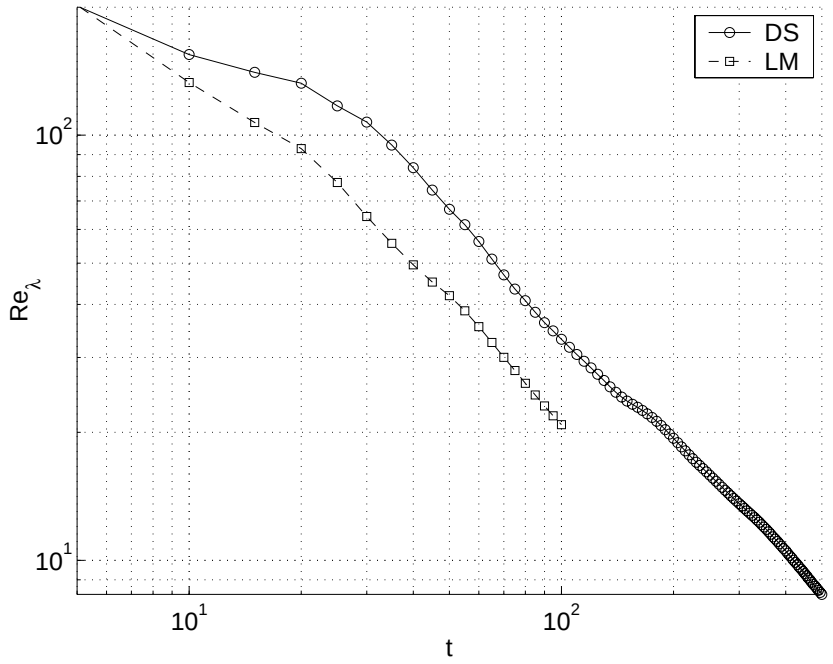

Figure 8–5: Reynolds number Re_λ obtained from (8.5): 32^3 LES.

should change at around $\mathrm{Re}_\lambda \approx 30$, which is in agreement with the LM run. This indicates that the better model is needed for the SGS energy dissipation than the one employed in the DS run.

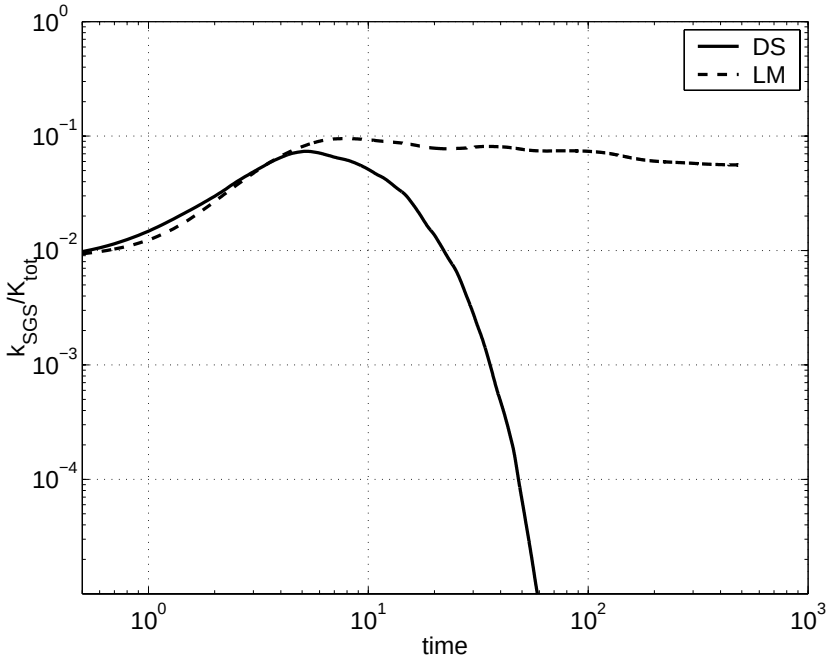

Figure 8–6: Fraction of the total kinetic energy stored in the subgrid scales: DS run (solid) and LM run (dashed).

Finally, the most striking difference between the DS and LM models is demonstrated in the Figure 8–6, which shows how the fraction of total kinetic energy stored in the subgrid scales changes in time. It should be noted that the final period of the isotropic decay is characterized by the absence of the inertial range in the energy spectrum[5] thus the fraction of energy stored in the subgrid scales should go to zero as the DIT approaches the final period. This is not captured by the LM set of models, which leaves from 5 to 10% of the energy in subgrid scales at all times, but the DS set of models captures the expected behaviour well.

8.3 Non-reacting mixing layer

An LES of a non-reacting incompressible mixing layer with a passive scalar (temperature) has been performed. Statistical results have been computed and compared to ones from DNS.[42] The results presented here have been obtained using an older model for the SGS energy dissipation:

$$\epsilon_s \approx \nu \frac{2k}{L_{kk}} \left[\widehat{\frac{\partial \overline{u}_i}{\partial x_j} \frac{\partial \overline{u}_i}{\partial x_j}} - \frac{\partial \widehat{\overline{u}}_i}{\partial x_j} \frac{\partial \widehat{\overline{u}}_i}{\partial x_j} \right].$$

The future work includes *a posteriori* test with the improved model for SGS energy dissipation.

8.3.1 Numerical setup

The TURF code was used in the simulation. The following are the parameters of the simulation.

- Non-staggered grids, explicit finite-difference scheme for spatial discretization, 5th order approximation in space, 3rd order of approximation in time.
- LES part of the code is characterized by adding two additional transport equations for k and θ — SGS kinetic energy and SGS temperature variance.
- Unlike the DNS simulation, LES run employs a uniform grid in all three directions (DNS used a non-uniform grid in the y-direction).
- The inlet conditions were modified. The time-dependent perturbations of the base inlet velocity profile are still introduced but they are put in the inlet profile of SGS kinetic energy k instead.
- Grid dimensions: $120 \times 60 \times 16$ (DNS grid dimensions were $481 \times 241 \times 39$).

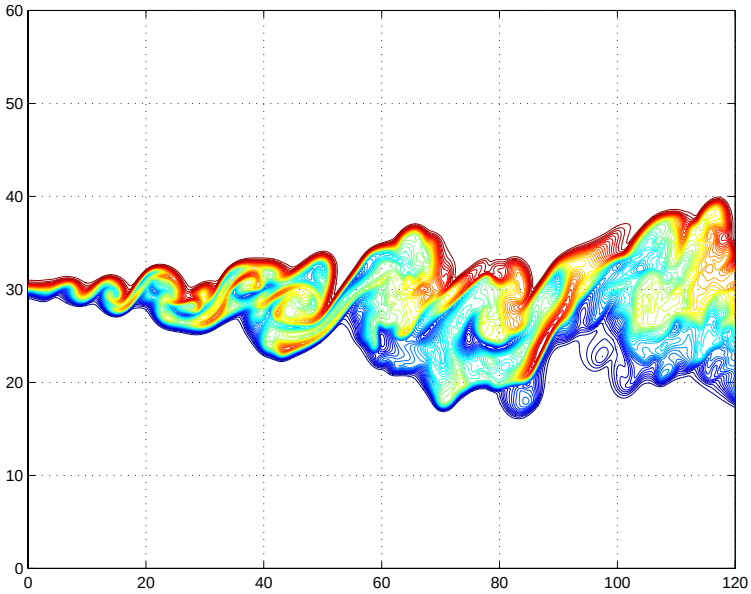

Figure 8–7: Snapshot of the temperature field in mixing layer (DNS).

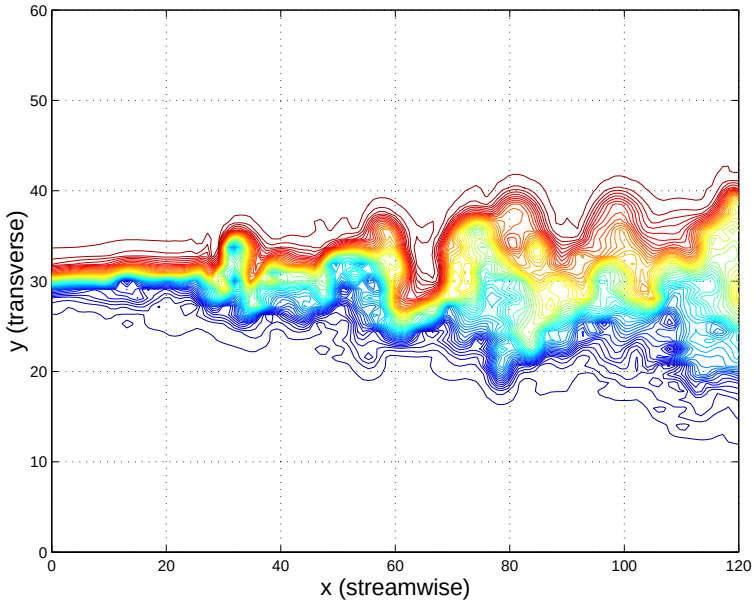

Figure 8–8: Snapshot of the temperature field in mixing layer (LES).

8.3.2 Simulation results

Figures 8–7 and 8–8 show snapshots of the scalar field for DNS and LES. Figure 8–9 shows a snapshot of the SGS variance θ of the passive scalar (temperature).

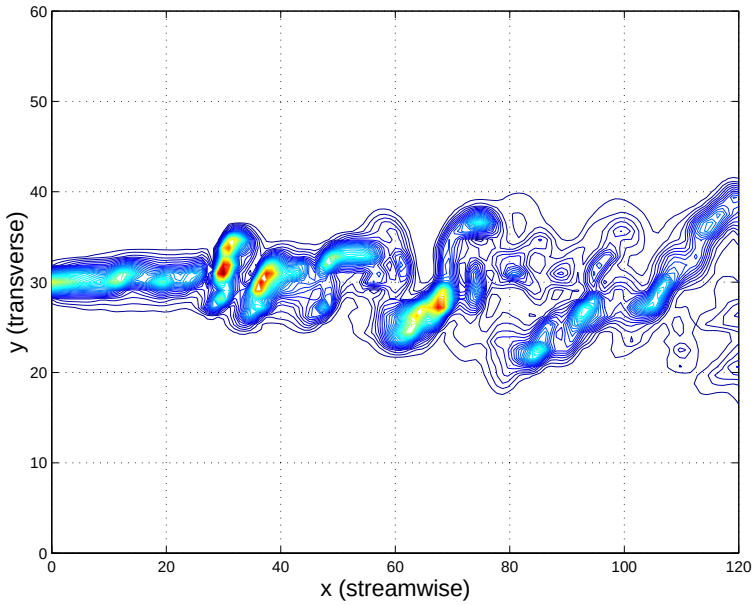

Figure 8–9: Snapshot of the temperature SGS variance in the mixing layer (DNS).

Figure 8–10 compares the rates of growth for LES and DNS mixing layers based on 1% scalar difference from the free stream. The growth rate of a mixing layer was found to be close to linear by many researchers. For a mixing layer with equal freestream densities, the following approximation was proposed:[26]

$$\frac{\delta}{x} = C_\delta \frac{1-r}{1+r},$$

where δ is the mixing layer width, x is the streamwise coordinate, C_δ is an empirical constant, and r is the low-to-high velocity ratio. The value of C_δ has been found to be in the range of $0.25 \ldots 0.45$ by a collection of experimental studies.[42] The DNS prediction for C_δ was 0.4554. The LES prediction is 0.422 which is regarded as a good match.

Thus, rates of growth match well the only difference being the location of the mixing

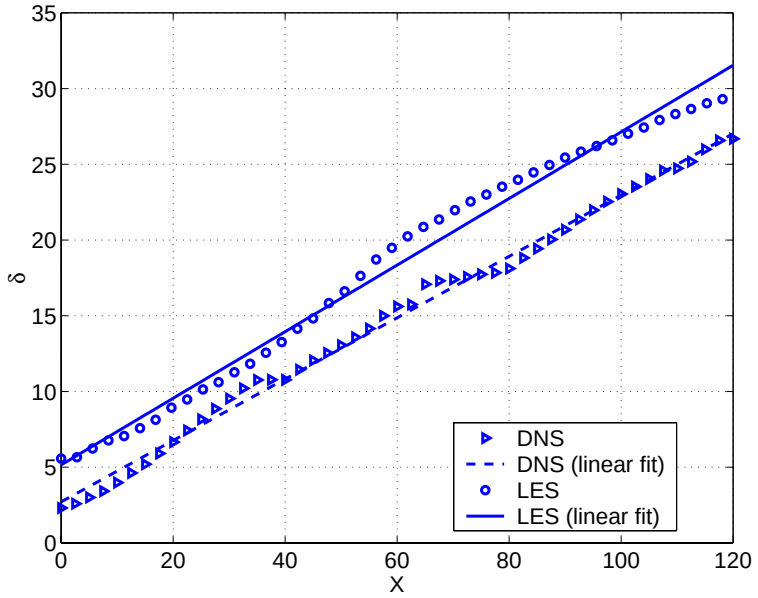

Figure 8–10: Mixing layer thickness based on 1% scalar difference: DNS and LES.

layer's virtual origin. The difference in the virtual origin locations was found to be approximately 10 space units. Thus the first- and second-order scalar statistics was taken at different locations for DNS and LES: $x = 110$ for DNS and $x = 100$ for LES.

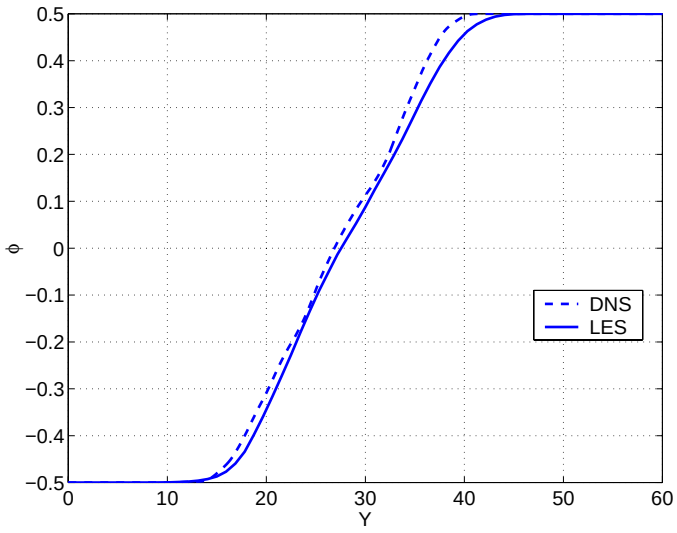

Figure 8–11: Mean transverse temperature profiles - LES and DNS.

Figures 8–11 and 8–12 present the first- and second-order scalar statistics at the measuring locations: mean transverse temperature profile and the transverse profile of the temperature variance measured from DNS and LES. Figure 8–11 shows a very good agreement between DNS and LES mean transverse temperature profiles. Note that both profiles have small but distinguishable "bump" slightly below $y = 30$. This little step in the mean temperature profile indicates that the center of the layer is well-mixed by the spanwise vortical structures, which gives a more homogeneous temperature in the center of the layer. Similar phenomena was observed in an experimental work by Pickett.[52] This also may indicate that by the time it reaches $x = 110$, the shear layer is almost fully developed.

The quantities compared in the Figure 8–12 are $\overline{\mathrm{Var}(\phi)} = \langle\overline{\phi\phi}\rangle - \overline{\langle\phi\rangle\langle\phi\rangle}$ obtained from the DNS data for the mixing layer, $\mathrm{Var}(\overline{\phi})$ obtained from the LES data, and $\mathrm{Var}(\overline{\phi}) + \langle\theta_\phi\rangle = \langle\overline{\phi\phi}\rangle - \langle\overline{\phi}\rangle\langle\overline{\phi}\rangle$ obtained from LES data. The last quantity is assumed to be close to $\overline{\mathrm{Var}(\phi)}$, that is, the difference between $\overline{\langle\phi\rangle\langle\phi\rangle}$ and $\langle\overline{\phi}\rangle\langle\overline{\phi}\rangle$ is assumed to be small. In the Figure 8–12, the SGS variance contributes up to as much as 45% of the total temperature variance. This indicates that the LES computational grid is too coarse for DNS, and the LES procedure is indeed applicable to the scalar field.

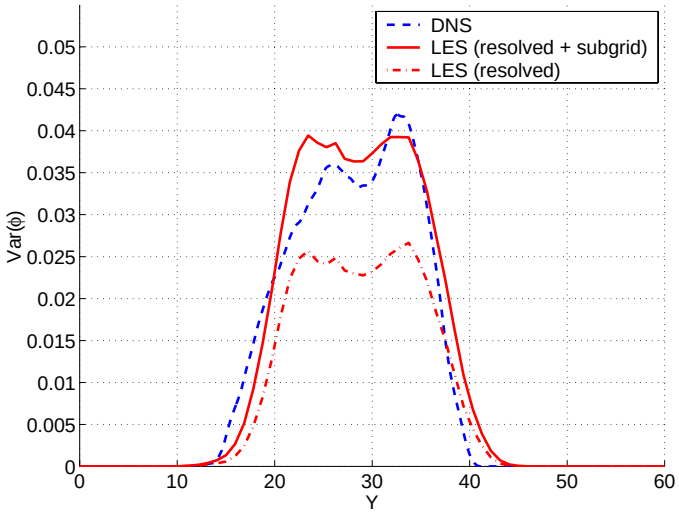

Figure 8–12: Transverse profile of temperature variance: DNS, LES resolved and (LES resolved + LES subgrid).

Chapter 9. Conclusions and Future Work

9.1 Conclusions

The development of predictive models for turbulent mixing relies on a detailed understanding of the interaction between turbulent flow structures and scalar field. In this work, results of direct numerical simulations were used to devise and evaluate the subgrid-scale models for Large Eddy Simulation.

Over the course of this work, three new SGS models were proposed and evaluated *a priori*:

- A model for the SGS scalar flux $\tau_{i\phi}$
- A model for the SGS scalar dissipation χ_s
- A model for the SGS kinetic energy dissipation ϵ_s.

The proposed models belong to a new class of SGS models named Dynamic Structure (DS) models. The DS model take the structure of the modeled term from the corresponding Leonard term and a particular form of a scaling factor is then used.

All proposed models seem to perform as well or better than the SGS models found in the literature in *a priori* tests. However, extensive *a posteriori* testing is required in order to fully evaluate the models' performance. Some *a posteriori* tests have been conducted already,[13,14] but none used all three models together.

A study of interaction between the turbulent flow structure and scalar field has been performed using the DNS data for channel flow, Couette flow, mixing layer and decaying

isotropic turbulence. The alignment trends of various quantities such as principal strain directions, vorticity and scalar gradient were studied in the framework of Large Eddy Simulation. This was done in order to provide us with insight into interaction between the resolved and sub-grid quantities and their statistical properties. It was found feasible to approach the SGS modeling from the point of view of statistical geometry thus giving us an efficient tool in the *a priori* evaluation of the model quality. A statistical similarity was found between the alignment trends of the scalar gradient $\nabla\phi$ in the fully resolved field and the alignment of the sub-grid scalar flux vector $\tau_{i\phi}$. The flow quantities that are defined by the small flow structures were found to have log-normal distribution, illustrating the Gurvich–Yaglom extension of the third Kolmogorov hypothesis.[31]

The DS model for SGS scalar flux $\tau_{i\phi}$ was found to perform better than the models from the literature under variety of conditions. In particular, it was found that the performance of the DS model was practically unaffected by the mean strain. The regions of the flow that have large mean strain appeared to be the most difficult for SGS modeling. All models from the literature that we compared the DS model to — eddy viscosity, self-similarity and gradient-viscosity, — tend to overpredicts the scalar flux in those regions. The DS model was found to be practically unaffected by the large mean strain.

The self-similarity approach was tested in modeling the zero-dimensional flow quantities such as SGS energy dissipation ϵ_s and the SGS scalar dissipation χ_s, to a certain degree of success. The main difficulty in modeling these two variables seems to be in finding a suitable length scale required by the particular form of the model that we use — the Kolmogorov length scale η for the model for ϵ_s, and the Batchelor length scale L_B for the model for χ_s. However, for the case of modeling ϵ_s, a way was proposed to overcome this difficulty by directly evaluating the (approximation for) Kolmogorov length scale from the SGS energy dissipation via $\epsilon_s = A\epsilon$ and solving the resulting algebraic equation for ϵ_s. Once the Kolmogorov length scale is approximated, we can find the local Batchelor length scale

and thus close the model for χ_s. The results of *a priori* test on the DNS data for isotropic turbulence look encouraging, but the thorough *a posteriori* testing is needed.

Finally, some *a posteriori* tests were done by performing LES of non-reacting mixing layer and decaying isotropic turbulence (DIT) with passive scalar. For the mixing layer, the earlier models for ϵ_s and χ_s were implemented, and for the DIT yet another earlier model for ϵ_s was used. Both simulations appeared to capture the flow structure well, and compare well with the results from the literature and DNS. For the mixing layer LES, the SGS scalar variance was found to contribute up to 45% of the total scalar variance, which indicated that significant part of the flow structures occurred in sub-grid scales.

Overall, the Dynamic Structure approach, when the spatial structure is taken from the corresponding Leonard term and an adaptive scaling factor is used, showed great promise for turbulence modeling and should be explored further.

9.2 Future work

The proposed outline of the future work is as follows.

SGS Energy Dissipation. Finish *a posteriori* testing for the model for ϵ_s first, because in our experience the model plays an important role in balancing the energy budget between the resolved and subgrid scales. If the energy balance is not maintained properly it could lead to blow-ups in the simulations. If the model for the SGS energy dissipation is found to be reliable and robust, the whole set of DS models can be implemented and used.

A posteriori **testing on engineering flows.** Extensive *a posteriori* testing is needed for the whole suite of models together. So far, we have tested the models on canonical flows — decaying isotropic turbulence, and mixing layer. These flows are ideal and seldom appear in practical calculations. More validation for the models is needed in practical applications.

The wall problem in LES. So far we have only tested the models *a posteriori* on the flows that did not have walls — isotropic turbulence and mixing layer. This was done because no general algorithm exists in LES for the wall treatment. The DS models showed superior performance near the walls in *a priori* testing. We need to run *a posteriori* tests based on LES of wall-bounded flows. Possible wall treatments include:

- Grid refinement near the wall,
- Modification of the filter function near the wall,
- Keeping the filtering function intact throughout the domain and formally extending flowfield into the wall for the filtering purposes.

Reacting flow simulation. The ultimate application of the scalar-related models is combustion simulation. Introducing LES concepts into combustion simulation should reduce the computational time. Coupling LES transport models and reaction mechanisms is rapidly growing area of LES.

Further applications. Other possible applications of scalar-related LES models include

- Pollutant transport
- Evaporation/condensation
- Cloud simulation
- Earth atmospheric layer simulation
- Interstellar simulation (galaxies etc.)

Appendix A. θ-equation.

For a scalar ϕ tranported in the flow, the quantity θ is defined as

$$\theta = \overline{\phi\phi} - \overline{\phi}\overline{\phi}.$$

A transport equation for θ derived for the case of incompressible flow.

The energy equation for the incompressible, non-reacting flow can be written in the non-dimensional form as following:

$$\frac{\partial \phi}{\partial t} + u_i \frac{\partial \phi}{\partial x_i} = \frac{1}{\rho \mathrm{ReSc}} \frac{\partial^2 \phi}{\partial x_i \partial x_i} \tag{A.1}$$

Applying the LES filtering operation to (A.1), and multiplying the whole equation by $\overline{\phi}$, we get

$$\overline{\phi}\frac{\partial \overline{\phi}}{\partial t} + \overline{u}_i\overline{\phi}\frac{\partial \overline{\phi}}{\partial x_i} = \frac{1}{\rho \mathrm{ReSc}}\overline{\phi}\frac{\partial^2 \overline{\phi}}{\partial x_i \partial x_i} - \overline{\phi}\frac{\partial \tau_{i\phi}}{\partial x_i}, \tag{A.2}$$

where

$$\tau_{i\phi} = \overline{u_i\phi} - \overline{u}_i\overline{\phi}.$$

Using the identify

$$\phi\frac{\partial^2 \phi}{\partial x \partial x} = \frac{\partial^2(\phi\phi/2)}{\partial x \partial x} - \frac{\partial \phi}{\partial x}\frac{\partial \phi}{\partial x}, \tag{A.3}$$

and absorbing $\overline{\phi}$ inside the derivatives, we can rewrite (A.2) as

$$\frac{\partial(\overline{\phi}\,\overline{\phi}/2)}{\partial t} + \overline{u}_i\frac{\partial(\overline{\phi}\,\overline{\phi}/2)}{\partial x_i} = \frac{1}{\rho \mathrm{ReSc}}\left[\frac{\partial^2(\overline{\phi}\,\overline{\phi}/2)}{\partial x_i \partial x_i} - \frac{\partial \overline{\phi}}{\partial x_i}\frac{\partial \overline{\phi}}{\partial x_i}\right] - \overline{\phi}\frac{\partial \tau_{i\phi}}{\partial x_i}. \tag{A.4}$$

Now let us multiply the equation (A.1) by ϕ first, and then apply the LES filtering operation. These manipulations result in the following equation:

$$\frac{\partial(\overline{\phi\phi}/2)}{\partial t} + \overline{u}_i\frac{\partial(\overline{\phi\phi}/2)}{\partial x_i} = \frac{1}{\rho \mathrm{ReSc}}\left[\frac{\partial^2(\overline{\phi\phi}/2)}{\partial x_i \partial x_i} - \overline{\frac{\partial \phi}{\partial x_i}\frac{\partial \phi}{\partial x_i}}\right] - \frac{1}{2}\frac{\partial}{\partial x_i}\left[\overline{\phi\phi u_i} - \overline{\phi\phi}\,\overline{u}_i\right]. \tag{A.5}$$

Note that we used the fact that LES filtering commutes with spatial and temporal derivatives which is true provided the LES filter function does not change throughout the domain.

Now, subtracting the equation (A.4) from (A.5) and multiplying the result by two, we obtain the following equation for θ:

$$\begin{aligned}\frac{\partial\theta}{\partial t}+\overline{u}_i\frac{\partial\theta}{\partial x_i} &= \underbrace{\frac{1}{\rho\mathrm{ReSc}}\frac{\partial^2\theta}{\partial x_i\partial x_i}}_{\text{diffusion}}-\underbrace{\frac{2}{\rho\mathrm{ReSc}}\left[\overline{\frac{\partial\phi}{\partial x_i}\frac{\partial\phi}{\partial x_i}}-\frac{\partial\overline{\phi}}{\partial x_i}\frac{\partial\overline{\phi}}{\partial x_i}\right]}_{\text{scalar dissipation}}- \\ &- \underbrace{\frac{\partial}{\partial x_i}\left[\overline{\phi\phi u_i}-\overline{\phi\phi}\,\overline{u}_i\right]}_{\text{triple correlation}}+\underbrace{2\overline{\phi}\frac{\partial\tau_{i\phi}}{\partial x_i}}_{\text{source}} \qquad \text{(A.6)}\end{aligned}$$

The equation (A.6) is exact, i.e., it does not contain any approximations or model terms. However, it contains the triple correlation term which needs to be modeled. This issue is dealt with by applying the Yeo series to the triple correlation and source terms. For brevity, we omit indices for α's in the Yeo series.

The triple correlation term gives:

$$-\frac{1}{2}\frac{\partial}{\partial x_i}\left[\overline{\phi\phi u_i}-\overline{\phi\phi}\,\overline{u}_i\right]=-\frac{\partial}{\partial x_i}\left[\alpha\frac{\partial\overline{u}_i}{\partial x_k}\frac{\partial\overline{\phi\phi}}{\partial x_k}+O(\alpha^2)\right]=$$

$$=-\frac{\partial}{\partial x_i}\left[\alpha\frac{\partial\overline{u}_i}{\partial x_k}\frac{\partial}{\partial x_k}\left(\overline{\phi}\,\overline{\phi}+2\alpha\frac{\partial\overline{\phi}}{\partial x_k}\frac{\partial\overline{\phi}}{\partial x_k}+O(\alpha^2)\right)+O(\alpha^2)\right]$$

Proceeding further and disregarding all terms that have powers of α higher or equal to 2, we obtain:

$$-\frac{1}{2}\frac{\partial}{\partial x_i}\left[\overline{\phi\phi u_i}-\overline{\phi\phi}\,\overline{u}_i\right]\approx-\frac{\partial}{\partial x_i}\left[\overline{\phi}\cdot 2\alpha\frac{\partial\overline{\phi}}{\partial x_k}\frac{\partial\overline{u}_i}{\partial x_k}\right]\approx-\tau_{i\phi}\frac{\partial\overline{\phi}}{\partial x_i}-\overline{\phi}\frac{\partial\tau_{i\phi}}{\partial x_i}.$$

Thus, if we substitute the obtained representation for the triple correlation term back into the equation (A.6), the approximate form of the transport equation for θ would be as follows:

$$\frac{\partial\theta}{\partial t}+\overline{u}_i\frac{\partial\theta}{\partial x_i}=\frac{1}{\rho\mathrm{ReSc}}\frac{\partial^2\theta}{\partial x_i\partial x_i}-\frac{2}{\rho\mathrm{ReSc}}\left[\overline{\frac{\partial\phi}{\partial x_i}\frac{\partial\phi}{\partial x_i}}-\frac{\partial\overline{\phi}}{\partial x_i}\frac{\partial\overline{\phi}}{\partial x_i}\right]-2\tau_{i\phi}\frac{\partial\overline{\phi}}{\partial x_i} \qquad \text{(A.7)}$$

Bibliography

[1] E. Adams, J. P. Johnson, and J. K. Eaton, *Experiments on the structure of turbulent reacting flow*, Tech. Report MD-43, Thermosciences Division, Dept. of Mechanical Engineering, Stanford University, 1984.

[2] K. Akselvoll and P. Moin, *Large eddy simulation of turbulent confined coannular jets and turbulent flow over a backward facing step*, Tech. Report TF-63, Thermosciences Division, Dept. of Mechanical Engineering, Stanford University, 1995.

[3] W. T. Ashurst, A. R. Kerstein, R. M. Kerr, and C. H. Gibson, *Alignment of vorticity and scalar gradient with strain rate in simulated navier-stokes turbulence*, Phys. Fluids, 30 (1987), pp. 2343–2353.

[4] J. K. Bo Tao and C. Meneveau, *Statistical geometry of subgrid-scale stresses determined from holographic particle image velocimetry measurements*, J. Fluid Mech., 457 (2002), pp. 35–78.

[5] R. Camussi and G. Gui, *Experimental analysis of scaling laws in low* re_λ *grid-generated turbulence*, Experiments in Fluids, 20 (1996), pp. 199–209.

[6] D. Carati and E. V. Eijnden, *On the self-similarity assumption on dynamic models for large eddy simulation*, Physics of Fluids, 9 (1997), pp. 2165–2167.

[7] S. Cerutti and C. Meneveau, *Intermittency and relative scaling of subgrid-scale energy dissipation in isotropic turbulence*, Phys. Fluids, 10 (1998), p. 928.

[8] ——, *Statistics of filtered velocity in grid and wake turbulence*, Phys. Fluids, 12 (2000), p. 1143.

[9] M. P. Chad Higgins and C. Meneveau, *Alignment trends of velocity gradients and subgrid-scale fluxes in the turbulent atmospheric boundary layer*, Boundary-Layer Meteorology, 109 (2003), pp. 59–83.

[10] ——, *The heat flux and the temperature gradient in the lowe atmosphere*, Geophysical Research Letters, 31 (2004), p. L22105.

[11] J. Chasnov, *Decaying turbulence in two and three dimensions*, in Advances in DNS/LES, C. Liu and Z. Liu, eds., Greyden Press, 1997.

[12] J. R. Chasnov, *On the decay of inhomogeneous turbulence*, Journal of Fluid Mechanics, 342 (1997), pp. 335–354.

[13] S. Chumakov, *Large-eddy simulation models for subgrid scalar transport*, master's thesis, University of Wisconsin–Madison, Madison WI, 2001. Dept. of Mechanical Engineering.

[14] S. G. Chumakov and C. J. Rutland, *Dynamic structure subgrid-scale models for large eddy simulation*, Int. J. Numer. Meth. Fluids, 47 (2005), pp. 911–923.

[15] R. A. Clark, J. H. Ferziger, and W. C. Reynolds, *Evaluation of subgrid-scale models using accurately simulated turbulent flow*, J. Fluid Mech., 91 (1979).

[16] S. S. Collins, *Monitoring unresolved scales in multiscale turbulence modeling*, Phys. Fluids, 13 (2001), pp. 1800–1806.

[17] G. Comte-Bellot and S. Corrsin, *The use of a contraction to improve the isotropy of grid-generated turbulence*, J. Fluid Mech., 25 (1966), pp. 657–682.

[18] ——, *Simple eulerian time correlation of full- and narrow-band velocity signals in grid-generated, "isotropic" turbulence*, J. Fluid Mech., 48 (1971), pp. 273–337.

[19] A. Cook and W. K. Bushe, *A subgrid-scale model for scalar dissipation rate in non-premixed combustion*, Phys. Fluids, 11 (1999), p. 746.

[20] A. W. Cook, *Determination of the constant coefficient in scale similarity models of turbulence*, Phys. Fluids, 9 (1997), pp. 1485–1487.

[21] A. W. Cook and J. J. Riley, *A subgrid model for equilibrium chemistry in turbulent flows*, Phys. Fluids, 6 (1994), p. 2868.

[22] S. G. Daniele Carati and P. Moin, *On the representation of backscatter in dynamic localization models*, Phys. Fluids, 7 (1995), p. 606.

[23] B. Debusschere, *Turbulent Scalar Transport in Non-Reacting and Reacting Flows*, PhD thesis, University of Wisconsin-Madison, 2001.

[24] B. Debusschere and C. J. Rutland, *Turbulent scalar transport mechanisms in plane channel and couette flows*, International Journal of heat and mass transfer, 47 (2004), pp. 1771–1781.

[25] P. E. DesJardin and S. H. Frankel, *Large eddy simulation of a non-premixed reacting jet: Application and assessment of subgrid-scale combustion models*, Physics of Fluids, 10 (1998), pp. 2298–2314.

[26] P. E. Dimotakis, *Turbulent free shear layer mixing and combustion*, in High-Speed Flight Propulsion System, S. N. B. Murphy and E. T. Curran, eds., vol. 137 of Progress in Astronautics and Aeronautics, Washington, D.C., 1991, pp. 265–340.

[27] V. Eswaran and S. B. Pope, *Direct numerical simulations of the turbulent mixing of a passive scalar*, Phys. Fluids, 31 (1988), pp. 506–520.

[28] D. A. Feikema, D. Everest, and J. F. Driscoll, *Images of dissipation layer to quantify mixing within a turbulent jet*, AIAA J., 34 (1996), pp. 2531–2538.

[29] M. Germano, U. Piomelli, P. Moin, and W. H. Cabot, *A dynamic subgrid-scale eddy viscosity model*, Physics of Fluids, 3 (1991), pp. 1760–1765.

[30] S. Ghosal and P. Moin, *The basic equations of the large eddy simulation of turbulent flows in complex geometry*, J. Comput. Phys., 118 (1995), p. 24.

[31] A. S. Gurvich and A. M. Yaglom, *Bearkdown of eddies and probability distributions for small-scale turbulence*, Phys. Fluids Suppl., (1967), pp. S59–S65.

[32] J. O. Hinze, *Turbulence*, New York: McGraw-Hill, 2nd ed., 1975.

[33] C. Jimenez, F. Ducros, B. Cuenot, and B. Bedat, *Subgrid scale variance and dissipation of a scalar field in large eddy simulations*, Physics of Fluids, 13 (2001), pp. 1748–1754.

[34] A. R. Kerstein and W. T. Ashurst, *Lognormality of gradients of diffusive scalars in homogeneous two-dimensional mixing systems*, Phys. Fluids, 27 (1984), pp. 2819–2827.

[35] W.-W. Kim and S. Menon, *A new dynamic one-equation subgrid-scale model for large eddy simulation.* AIAA 95-0356, 1995.

[36] W.-W. Kim, S. Menon, and H. C. Moniga, *Large-eddy simulation of a gas turbine combustor flow*, Combust. Sci. Tech., 143 (1999), pp. 25–62.

[37] H. Kobayashi and Y. Shimomura, *Inapplicability of the dynamic clark model to the large eddy simulation of incompressible turbulent channel flows*, Phys. Fluids, 15 (2003), pp. L29–L32.

[38] A. N. Kolmogorov, *The local structure of turbulence in incompressible viscous fluid for very large reynolds numbers*, Doklady Akad. Nauk, USSR 30:301, (1941).

[39] A. Leonard, *Large eddy simulation of chaotic convection and beyond.* AIAA Paper 97-0204, 1997.

[40] D. K. Lilly, *A proposed modification of the germano subgrid-scale closure method*, Physics of Fluids, 4 (1992), pp. 633–635.

[41] S. Liu, C. Meneveau, and J. Katz, *On the properties of similarity subgrid-scale models as deduced from measurements in a turbulent jet*, Journal of Fluid Mechanics, 275 (1994), pp. 83–119.

[42] S. D. Mason, *Turbulence Transport in Spatially Developing Reacting Shear Layers*, PhD thesis, University of Wisconsin-Madison, 2000.

[43] S. Menon, P.-K. Yeung, and W.-W. Kim, *Effect of subgrid models on the computed interscale energy transfer in isotropic turbulence*, Computers and Fluids, 25 (1996), pp. 165–180.

[44] A. Misra and D. I. Pullin, *A vortex-based subgrid stress model for large-eddy simulation*, Phys. Fluids, 9 (1997), pp. 2443–2454.

[45] M. S. Mohamed and J. C. LaRue, *The decay power law in grid-generated turbulence*, J. Fluid Mech., (219), pp. 195–214.

[46] P. Moin, K. Squires, W. Cabot, and S. Lee, *A dynamic subgrid-scale model for compressible turbulence and scalar transport*, Phys. Fluids A, 3 (1991).

[47] R. D. Moser, J. Kim, and N. N. Mansour, *Direct numerical simulation of turbulent channel flow up to* $\mathrm{re}_\tau = 590$, Phys. Fluids, 11 (1999), pp. 943–945.

[48] K. K. Nomura and S. E. Elghobashi, *Mixing characteristics of an inhomogeneous scalar in isotropic and homogeneous sheared turbulence*, Phys. Fluids A, 4 (1992), pp. 606–625.

[49] N. Okong'o and J. Bellan, *A priori subgrid analysis of temporal mixing layers with evaporating droplets*, Phys. Fluids, 12 (2000), p. 1573.

[50] M. R. Overholt and S. B. Pope, *A deterministic forcing scheme for direct numerical simulations of turbulence*, Computers & Fluids, 27 (1998), pp. 11–28.

[51] J. Pallares and L. Davidson, *Large-eddy simulations of turbulent heat transfer in stationary and rotating turbulence*, Phys. Fluids, 14 (2002), pp. 2804–2816.

[52] L. M. Pickett, *Structure of a planar reacting shear layer using hydrocarbon fuels*, PhD thesis, University of Wisconsin-Madison, Madison, WI, 2000.

[53] C. Pierce and P. Moin, *A dynamic model for subgrid-scale variance and dissipation rate of a conserved scalar*, Physics of Fluids, 12 (1998), pp. 3041–3044.

[54] S. Pirozzoli and F. Grasso, *Direct numerical simulation of isotropic compressible turbulence: incluence of compressibility on dynamic structures*, Phys. Fluids, 16 (2004), pp. 4386–4407.

[55] E. Pomraning, *Development of Large Eddy Simulation Turbulence Models*, PhD thesis, UW-Madison, 2000.

[56] E. Pomraning and C. J. Rutland, *Dynamic one-equation nonviscosity large-eddy simulation model*, AIAA Journal, 40 (2002), pp. 689–701.

[57] S. B. Pope, *Turbulent Flows*, Cambridge Univ. Press, 2000.

[58] D. I. Pullin, *A vortex-based model for the subgrid flux of a passive scalar*, Physics of Fluids, 12 (2000), pp. 2311–2319.

[59] S. Rao, E. Pomraning, and C. J. Rutland, *Development of advanced combustion models for diesel engines using large eddy simulation*, in Second Joint Meeting of the US Sections of the Combustion Institute, Oakland, CA, March 26–28 2001.

[60] L. F. Richardson, *Weather Prediction by Numerical Process*, Cambridge Univ. Press, Cambridge, UK, 1922.

[61] J. R. Ristorcelli and D. Livescu, *Decay of isotropic turbulence: Fixed points and solutions for nonconstant $g \sim r_\lambda$ palinstrophy*, Phys. Fluids, 16 (2004), pp. 3487–3490.

[62] P. M. Sandip Ghosal, Thomas S. Lund and K. Akselvoll, *A dynamic localization model for large-eddy simulation of turbulent flows*, J. Fluid Mech., 286 (1995), pp. 229–255.

[63] U. Schumann, *Realizability of the reynolds-stress turbulence models*, Physics of Fluids, 20 (1977), pp. 721–725.

[64] J. Smagorinsky, *General circulation experiments with the primitive equations*, Monthly Weather Review, 93 (1963).

[65] C. G. Speziale, *Analytic methods for the development of reynolds-stress closures in turbulence*, Ann. Rev. Fluid Mech., 23 (1991), pp. 107–157.

[66] ——, *Turbulence modeling for time-dependent rans and vles: A review*, AIAA Journal, 36 (1998), pp. 173–184.

[67] G. D. Stefano and O. V. Vasilyev, *Sharp cutoff versus smooth filtering in large eddy simulation*, Phys. Fluids, 14 (2002), pp. 362–369.

[68] L. K. Su and N. T. Clemens, *Planar measurements of the full three-dimensional scalar dissipation rate in gas-phase turbulent flows*, Experiments in Fluids, 27 (1999), pp. 507–521.

[69] H. Tenneks and J. L. Lumley, *A First Course in Turbulence*, MIT Press, 1972.

[70] H. van der Ven, *A family of large eddy simulation (les) filters with nonuniform filter widths*, Phys. Fluids, 7 (1995), p. 1171.

[71] O. V. Vasilyev and D. E. Golstein, *Local spectrum of commutation error in large eddy simulations*, Phys. Fluids, 16 (2004), pp. 470–473.

[72] O. V. Vasilyev, T. S. Lund, and P. Moin, *A general case of commutative filters for les in complex geometries*, J. Comput. Phys., 146 (1998), pp. 82–104.

[73] T. Voelkl and D. I. Pullin, *A physical-space version of the stretched-vortex subgrid-stress model for large-eddy simulations*, Phys. Fluids, 12 (2000), p. 1810.

[74] F. M. White, *Viscous Fluid Flow*, McGraw-Hill Book Company Inc., 2 ed., 1991.

[75] A. Wray, *Decaying isotropic turbulence*, in A Selection of Test Cases for the Validation of Large-Eddy Simulations of Turbulent Flows, AGARD Advisory Report 345, pp. 63–64.

[76] W. K. Yeo, *A Generalized High Pass / Low Pass Averaging Procedure for Deriving and Solving Turbulent Flow Equations*, PhD thesis, Ohio State University, 1987.